Diploma Thesis

Flow Simulation of a Centrifugal Pump with Finite Volume Methods and Smoothed Particle Hydrodynamics

Alexandre Dodier

Institute for Thermal Turbomachinery and Machine Dynamics
Graz University of Technology
Head : o.Univ.-Prof. Dr.-Ing. Franz HEITMEIR

Assessor : Ao.Univ.-Prof. Dipl.-Ing. Dr.techn. Wolfgang SANZ
Supervisor : Dipl.-Ing. Dr.techn. Arno GEHRER
Dipl.-Ing. Magdalena NEUHAUSER

Graz, March 2012

Kurzfassung

Das Ziel dieser Arbeit ist die Anwendung branchenüblicher CFD-Methoden gemeinsam mit einer neuartigen Methode genannt Smoothed Particle Hydrodynamics (SPH) auf hydraulischen Pumpen. In Hinsicht auf die Verringerung der numerischen Fehler mittels einer netzfreien Methode soll im Zuge dieser Arbeit die Anwendbarkeit der SPH Methode an einer Pumpe untersucht werden. Man erwartet sich von dieser Methode die Möglichkeit, die Fehler minimieren zu können, welche auf die Interaktion zwischen stehenden und rotierenden Netzen zurückzuführen sind. Dazu wurden im Laufe dieser Arbeit mehrere Tools an den jeweiligen Standorten der R&D Abteilungen bei ANDRITZ entwickelt, um diese Methode erstmals an einer Pumpe anzuwenden. Der Prototyp dieser Pumpe wurde vor dieser Arbeit bereits erfolgreich entwickelt und am ASTRÖ Prüfstand in Graz vermessen. Diese Pumpe erreichte einen sehr hohen Wirkungsgrad, jedoch wies die Pumpenkennlinie eine Hysterese auf. Dieses Phänomen wird in der Forschung ambitioniert verfolgt, da die Strömungseffekte, welche im Bereich der Teillast entstehen, problematische Auswirkungen auf den Betrieb haben können. Dieser Effekt ist bislang durch numerische Methoden nur schwer zu erfassen.

Diese Arbeit soll den Anwendungsbereich für die verwendeten numerischen Methoden in der Pumpenentwicklung erweitern und wurde in zwei Phasen unterteilt. Die erste Phase umfasste die Erstellung eines Benchmark mittels der Software ANSYS CFX. Dazu wurde das Netz des zuvor erfolgreich abgeschlossenen Projekts von der R&D Abteilung in Graz zur Verfügung gestellt und mit einer quasi-stationären 'Frozen Rotor'-, sowie einer transienten Rechnung evaluiert. Des weiteren beinhaltet die Evaluierung die numerischen Ergebnisse der in der Abteilung ASTRÖ verwendeten sogenannten 'Eulerkette', welche ebenfalls auf der Finite-Volumen-Methode (FVM) basiert. Ziel sollte sein, in Zukunft einen direkten Vergleich zwischen Finite-Volumen-Methoden und SPH zu ermöglichen. Die zweite Phase wurde am ANDRITZ HYDRO Standort Vevey durchgeführt und sollte die erstmalige Anwendung der SPH Methode an einer Pumpe umfassen. Da sich diese Methode im Entwicklungsstadium befindet, war meine Aufgabe zunächst die Erstellung und Aufbereitung zwei-dimensionaler Testfälle, welche von der SPHERIC Community verfolgt werden. Hierfür wurden zahlreiche Simulationen parallel zu den sich im Gange befindenden Entwicklungen an diesem Code ausgeführt.

Aufgrund der Fülle an Daten und der sich im Evaluierungsstadium befindenden Ergebnisse wurde in dieser Arbeit hauptsächlich über die Berechnung der oben erwähnten Pumpe berichtet. Hierzu ist es gelungen Berechnungen durchzuführen, welche in Zukunft einen direkten Vergleich ein-und-derselben Geometrie mittels verschiedener numerischer Methoden erlaubt. Es wurde jedoch deutlich, dass die SPH Methode noch einige Entwicklungsschritte benötigt in Hinsicht auf die Stabilität, weshalb bislang noch keine Evaluierung der Pumpe durchgeführt wurde.

Abstract

The aim of this work is the application of industry-standard CFD methods together with a new type of method called Smoothed Particle Hydrodynamics (SPH) on hydraulic pumps. In the course of this work the feasibility study should be performed regarding the use of the SPH method on a pump, with the goal of reducing the numerical error by a mesh-less method. It is expected from this method, that the errors can be minimized coming along with the simulation due to the avoidance of the interaction between static and rotating systems. For this reason several tools were developed at the respective locations of the R&D departments of ANDRITZ in order to apply this method for the first time on a pump. The prototype of this pump was developed and measured successfully prior to this work on the test bench of Andritz in Graz. The pump reached a very high efficiency, however, the characteristic curve showed a hysteresis. This phenomenon is pursued in an ambitious manner in research, as the flow effects which arise in part-load may have an impact on the operation, which is difficult to reproduce with numerical methods.

This work aims to extend the field of applied numerical methods in pump development and was therefore divided into two phases. The first phase involved the establishment of a benchmark using the software ANSYS CFX. For this purpose the mesh from a previously successfully completed project was provided by the R&D department in Graz and in consequence evaluated with a quasi-steady 'Frozen-Rotor' as well as a transient calculation. The evaluation also comprises the numerical results of the so-called 'Eulerkette', applied at the ASTRÖ department, which is based on the finite volume method. The goal should be a direct comparison between SPH and finite volume methods in the future. The second phase was conducted at the ANDRITZ HYDRO site in Vevey and should include the first use of the SPH method on a pump geometry. As this method is still under development, it was my objective to establish and prepare two-dimensional test cases, based on publications of the SPHERIC Community. For this purpose several simulations were performed parallel to the developments on this code, which have already been in progress.

Due to the great amount of data and results which are still under evaluation, this thesis is restricted to the main topic, namely the calculation of the above mentioned pump. It was achieved to obtain calculations and will allow in future a direct comparison of different numerical methods. However, it was clearly shown that the SPH method still requires further development with regard to stability so that no evaluation of the pump has been performed to this stage.

Deutsche Fassung:
Beschluss der Curricula-Kommission für Bachelor-, Master- und Diplomstudien vom 10.11.2008
Genehmigung des Senates am 1.12.2008

EIDESSTATTLICHE ERKLÄRUNG

Ich erkläre an Eides statt, dass ich die vorliegende Arbeit selbstständig verfasst, andere als die angegebenen Quellen/Hilfsmittel nicht benutzt, und die den benutzten Quellen wörtlich und inhaltlich entnommene Stellen als solche kenntlich gemacht habe.

Graz, am ……. ……..
(Unterschrift)

Englische Fassung:

STATUTORY DECLARATION

I declare that I have authored this thesis independently, that I have not used other than the declared sources / resources, and that I have explicitly marked all material which has been quoted either literally or by content from the used sources.

……. ……..
date (signature)

Danksagung

Diese Diplomarbeit wurde im Zeitraum 2011/12 am Institut für Thermische Turbomaschinen und Maschinendynamik an der Technischen Universität Graz durchgeführt. Um meinen aufrichtigen Dank auszudrücken, möchte ich mich bei allen Beteiligten dieser Arbeit für Ihre Unterstützung bedanken. Um dieser Anerkennung gerecht zu werden, müsste ich beinahe jeden einzelnen Angestellten der F&E Abteilungen von Graz sowie von Vevey namentlich erwähnen. Ich möchte mich jedoch auf die Personen beschränken, welche mir diese Arbeit insbesondere ermöglicht haben.

Zum Ersten möchte ich mich bei Prof. Wolfgang Sanz bedanken, welcher mir bereits während meines Studiums das Vertrauen als Studienassistent schenkte und in weiterer Folge mir diese Diplomarbeit ermöglichte. Beinahe im selben Atemzug bedanke ich mich bei Dr. Arno Gehrer, welcher mir in seiner Abteilung in Graz in einem professionellen und stets angenehmen Arbeitsumfeld unschätzbare Erfahrungen im Bereich der Entwicklung hydraulischer Maschinen ermöglichte. In Folge entwickelte sich meine Arbeit zu einer fruchtbaren Kooperation zwischen den beiden Standorten Graz sowie in Vevey (Schweiz).

Dr. Etienne Parkinson vermittelte mir von Beginn an sein Vertrauen und ermöglichte mir diese Arbeit am Standort Vevey, weshalb ich ihm sehr dankbar bin. Die Mitarbeit in seinem hochmotivierten und hochkompetenten F&E Team an einer neuartigen Simulationsmethode war eine außerordentlich spannende Erfahrung für mich.

Besonderen Dank möchte ich auch meiner Betreuerin Magdalena Neuhauser entgegenbringen, welche mir die in dieser Arbeit behandelte neuartige Methode in Maschinenbauersprache übersetzte und stets ein offenes Ohr hatte. Ich bedanke mich für ihre professionelle und freundschaftliche Betreuung und wünsche ihr viel Erfolg für ihre PhD Arbeit. Besondere Wertschätzung möchte ich für Jean-Christophe Marongiu ausdrücken, welcher mir mit seinen zukunftsträchtigen Ideen umfassenden Einblick in den Bereich der Entwicklung ermöglichte.

Dem Institut für Hydraulischen Strömungsmaschinen möchte ich für die Unterstützung bei der Analyse und Interpretation der CFD Simulationen danken. Ebenso möchte ich mich diesbezüglich auch bei Prof. Benigni für seine Expertise bedanken.

Michael Buchmayr gab mir einen wichtigen Einblick in die numerische Strömungssimulation, welche für meinen Einstieg in diese Domäne wertvoll und aufschlussreich war. Die Genies der Bits und Bytes dürfen in der Liste der Anerkennungen keineswegs fehlen. Die unermüdliche Geduld und Ausdauer von Jeremy D'Inverno und Dr. Pascal Lemmonier sowie ihre Freundschaft hat mich geprägt.

Zuletzt möchte ich allen nicht namentlich erwähnten Beteiligten und Wegbegleiter der Standorte Graz und Vevey für ihre Unterstützung und Freundschaft danken. Die warmherzige und freundschaftliche Atmosphäre am Arbeitsplatz werden mir in bester Erinnerung bleiben und für meinen beruflichen Werdegang als Vorzeigemodell für eine gelungene Firmenphilosophie dienen.

Der größte Dank gebührt jedoch meiner Mutter, welche mich stets während meines Studiums unterstützt hat. Ihr Rückhalt sowie ihre unermüdliche Hingabe hat mich und meine beiden Brüder maßgeblich geprägt.

Remerciements

La présente thèse a été réalisée dans la période 2011/12 à l'Institut de Turbomachines Thermiques à l'Université Technique de Graz (Autriche). Afin d'exprimer ma sincère gratitude, je tiens à remercier toutes les personnes impliquées dans cette thèse pour leur soutien et engagement sans lesquels ce travail n'aurait pas été possible. Pour que cette reconnaissance soit la plus complète, il me faudrait remercier chaque employé des départements R&D de Andritz à Graz et à Vevey. Par souci de concision, je vais cependant me limiter aux personnes qui m'ont particulièrement encouragées et soutenues dans ce travail.

Tout d'abord, je tiens à remercier le Professeur Wolfgang Sanz, qui m'a déjà gratifié de sa confiance pendant mes études, en étant son assistant d'étude, et qui par la suite m'a permis d'effectuer cette thèse. De même, je tiens à remercier le Dr. Arno Gehrer, qui m'a accepté dans son département chez Andritz à Graz, et avec qui j'ai pu travailler dans un environnement professionnel et toujours agréable, me permettant d'acquérir une expérience inestimable dans le développement des machines hydrauliques. Ainsi mon travail s'est développé dans une fructueuse coopération entre les deux sièges à Graz et à Vevey (Suisse).

Dès notre première rencontre, le Dr. Etienne Parkinson m'a accordé sa confiance et m'a permis de travailler sur le site de Vevey, ce pourquoi je lui suis très reconnaissant. Le travail dans son équipe de R&D très motivée et compétente sur une méthode de simulation était une expérience particulièrement enrichissante pour moi.

J'adresse également de chaleureux remerciements à mon superviseur Magdalena Neuhauser qui m'a soutenue en 'traduisant' les nouvelles méthodes de travail dans la langue du génie mécanique et qui a toujours eu une oreille attentive à mes besoins. Je lui suis reconnaissant de son attitude très professionnelle et amicale et je lui souhaite le succès et la réussite pour son doctorat. Des remerciements spéciaux à Jean-Christophe Marongiu encore qui, grâce à ses talents de visionnaire, m'a offert un aperçu riche et instructif du travail R&D.

De sincères remerciements à l'Institut de Mécanique des Fluides Hydraulique à Graz pour leur soutien dans l'analyse et l'interprétation des simulations CFD. Je voudrais également remercier à cet égard le professeur Benigni pour son expertise.

Michael Buchmayr m'a donné un aperçu important sur la simulation numérique des écoulements, ce qui constitua pour moi une introduction précieuse et instructive dans ce domaine. Les génies des bits et des octets ne doivent pas manquer dans la liste des remerciements. La patience et la persévérance sans limite de Jeremy D'Inverno et du Dr. Pascal Lemonnier tout comme leur amitié m'a touchées.

Je tiens à remercier tous les participants et compagnons qui ne sont pas mentionnés par leur nom sur les sites de Graz et de Vevey pour leur soutien et leur amitié. Je demeure fortement imprégné par l'atmosphère chaleureuse et conviviale au travail, qui me restera en mémoire pour ma future carrière comme modèle à suivre pour le succès d'une entreprise.

Enfin mes plus grands remerciements à ma mère qui m'a toujours soutenu pendant mes études. Son soutien et son infatigable dévouement m'ont considérablement aidé, tout comme mes deux frères.

Contents

List of Symbols

c	absolute velocity [$\mathrm{m\,s^{-1}}$]
b	acceleration [$\mathrm{m\,s^{-2}}$]
D, d	diameter [m]
F	force
H_{torque}	delivered head by the impeller [m]
n	rotational speed [$\mathrm{min^{-1}}$]
n_q, n_s	specific speed [$\mathrm{min^{-1}}$]
$NPSH$	net positive suction head
P	power
p	static pressure
Q	flow rate
r	radius [m]
T	torque
u	circumferential velocity
V	volume
w	relative velocity
Y	specific work
α	angle between direction of circumferential and absolute velocity
β	angle between relative velocity vector and the negative direction of the circumferential velocity
η	efficiency
η_h	hydraulic efficiency
μ	dynamic viscosity [$\mathrm{kg{\cdot}m^{-1}s^{-1}}$]
ν	kinematic viscosity [$\mathrm{m^2s^{-1}}$]
ρ	density [$\mathrm{kg{\cdot}m^{-3}}$]
σ	deviation [%]
φ	flow coefficient [-]
ψ	head coefficient [-]
ω	angular rotor velocity [$\mathrm{rad\ s^{-1}}$]

List of Abbreviations

A	Area, cross section
BC	Boundary Conditions
BEP	Best Efficiency Point
BL	Blade
CFD	Computational Fluid Dynamics
CM	Control Mass
CV	Control Volume
D,d	diameter
df	disk friction
DT	Draft Tube
FVM	Finite Volume Method
HP	High Pressure
IEC	International Engineering Consultants
LP	Low Pressure
OL	Overload
OP	Operating Point
PL	Partload
RANS	Reynolds Averaged Navier Stokes
Rec	Recirculation
RN	Runner
SC	Spiral Casing
SST	Shear Stress Transport
SHR	Shroud
th	theoretical flow condition
tot	total
TKE	Turbulent Kinetic Energy
TM	Turbulence Model
TR	Test Rig

List of Figures

Introduction

The following work, conducted for the ANDRITZ Group, involves a comparison between commonly used finite volume methods and an in-house code developed by the R&D department at ANDRITZ HYDRO Vevey (Switzerland) and the Ecole Centrale de Lyon (LMFA) applied on a centrifugal pump. The first method deals with a mesh-based approach, while the latter code involves a mesh-free description, allowing to discretize the domain in accordance with the desired fluid particle size.

For this purpose, this work was carried out at the ANDRITZ sites of Graz and Vevey (Switzerland). The SPH code has been developed over the past few years to a successful tool for the development and optimization of Pelton turbines. It was found, that the mesh-free method was very advantageous for the simulation of free surface flows, since no additional mesh generation and updating is required. The code ASPHODEL developed in Vevey, has the advantage that the description of the movement in space couples both the Lagrange and Euler formulation, leading to the Arbitrary Lagrangian Eulerian method. From this method it is expected, that the numerical errors can be minimized, due to the evidence of the interaction between static and rotating systems. Commercial simulation methods have reached a level in recent years, at which the application on turbomachines gained a high practical value. Here several models with different geometries are validated within a short time, and ultimately allow the reduction to a few models. This implies, however, that so far the necessary quality and reliability regarding a pump design using numerical methods has not been reached, so that laboratory and test rig measurements are still required. An increase in accuracy of the numerical reproducibility could reduce the costs of expensive laboratory tests.

Thesis Outline

Chapter 1 gives a thorough introduction on the scope of this work and enables a brief explanation concerning the challenges of pump design. Trigger for the consideration of a mesh-free method were complications which had arisen during a previous pump project. A specific type of instability was found in the vicinity of the best efficiency point, causing a trough within the characteristic curve. Different mechanisms are held responsible for this instability, which depends on three-dimensional and non-uniform flow effects. Various losses can be distinguished within a centrifugal pump, where the focus in this section is laid on the hydraulic losses.

The fundamentals of numerical analysis of fluid mechanic problems are described in chapter 2, where the theoretical background of the involved methods as well as different numerical errors will be discussed.

The following chapters 3 to 6 will focus on the investigated numerical methods in this work; namely ANSYS CFX, followed by the so-called 'Eulerkette' used at the R&D department in Graz (ASTRÖ), and finally completed by the Smoothed Particle Hydrodynamic method. The latter represents the main reason for the origin of this work, which deals with a novel mesh-free method developed at the R&D department at ANDRITZ HYDRO Vevey. The fundamentals of the standard SPH description are given, from which the Arbitrary Lagrange Euler description has been implemented into a code named ASPHODEL by J.C. Marongiu and J.Leduc.

Chapter 7 focusses on the analysis of the performed simulations in ANSYS CFX 5.0, which were carried out during the first phase of this work. Additionally, the results of the ASTRÖ in-house code were included in the evaluation. This analysis should serve as reference data for future comparison with the results from the ASPHODEL calculations. The validation of the numerical results is performed with experimental data from the ASTRÖ test rig, which were conducted prior to this thesis.

Finally, this thesis is summarized in the conclusion together with suggestions for future developments and applications of the SPH-ALE method.

1. Centrifugal pumps

This chapter gives an introduction on the application and challenges of centrifugal pumps. Different loss mechanisms will be explained based on their origin in order to draw correlations with mechanisms causing flow instabilities. This section is based on the insights from [6] and [1].

1.1. Pump types

Centrifugal pumps are turbo machines used to convert mechanical energy into hydraulic energy, by raising a liquid flow to a specific pressure level. The working principle relates to the transfer of angular momentum of the impeller to the flow through the pump based on hydrodynamic processes. Therefore the flow enters the impeller axially and leaves radially on a considerably larger radius, which is representative for radial pumps. Centrifugal pumps are highly important for various technical processes in industry and domestic applications. Industry uses these machines for the transport of fluids, for power generation in pump turbines and chemical processes. A general design of a centrifugal pump is represented in Figure 1.1. The flow is guided from the draft tube to the impeller, where the energy is transferred from the driven shaft to the fluid, where it is accelerated in circumferential direction. The fluid is led from the impeller into the volute, where the flow is decelerated in the diffuser in order to convert the kinetic energy into a maximum static pressure. An impeller consists of the hub, the shroud and the blades equally arranged around the circumference.

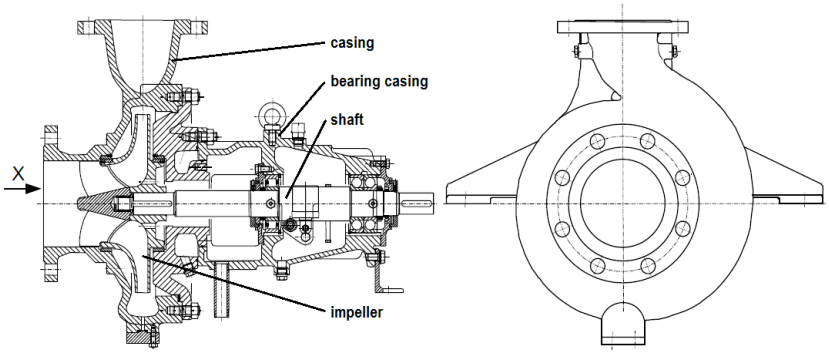

Figure 1.1.: Single-stage volute pump with bearing frame, Sulzer Pumpen AG [6].

A pump is characterized by the flow rate Q_{opt}, the head H_{opt} and the rotor speed n. The flow rate is generally defined as the useful volume flow through the discharge nozzle. The

head H can also be represented as the specific work Y.

The specific work Y is the total useful energy transmitted by the impeller to the liquid per unit of mass. For incompressible flow Y results from $\Delta p_{tot}/\rho$. Substituting the momentum equation for the flow through the impeller, one also obtains the transmitted specific work (Equ.(1.1)). The total pressure consists of the static pressure p, the pressure $\rho \cdot g \cdot z$ corresponding to the geodetic head and the dynamic pressure $\frac{1}{2}\rho c^2$.

$$Y = \frac{p_{2,tot} - p_{1,tot}}{\rho} = g \cdot H = u_2 c_{2u} - u_1 c_{1u} \tag{1.1}$$

The total dynamic head measured between suction (s) and discharge (d) nozzles results from the difference between the total pressures expressed as heads $H = H_d - H_s$. By means of the Bernoulli equation we obtain the energy head:

$$H = \frac{p_d - p_s}{\rho g} + z_d - z_s + \frac{c_d^2 - c_s^2}{2g} \tag{1.2}$$

In order to ensure the specified flow rate through a given plant, the pump needs to deliver a certain head of the plant H_A. Applying Bernoulli's equation on the system considering the head losses H_v (suction and discharge), we obtain the curve for the energy head of the plant:

$$H_A = \frac{p_a - p_e}{\rho g} + z_a - z_e + \frac{c_a^2 - c_e^2}{2g} + H_{v,d} + H_{v,s} \tag{1.3}$$

In steady operation the energy head of the pump equals the required head of the plant, hence $H = H_A$.

1.2. Pump design

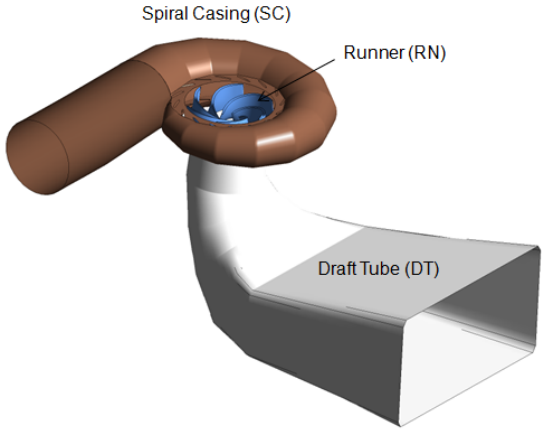

Figure 1.2.: Illustration of the investigated $n_q = 70$ pump.

The investigated pump type in this work refers to a single stage pump with a volute (or spiral) casing. This design is common in many industrial applications. Gülich states that radial pumps of this type are typically designed for specific speeds in the range of $n_q = 7$ to 100. The pump is designed in vertical arrangement, as shown in Figure 1.2, with the corresponding draft tube at inlet and the spiral casing at outlet. The induced flow at the inlet of the pump is directed through the DT, and subsequently enters the impeller in axial direction. In this, the supplied mechanical energy from a motor is converted into kinetic energy by accelerating the fluid, and into potential energy by increasing the fluid pressure. The prototype was designed for a flow rate Q of $0,4\left[\frac{m^3}{s}\right]$ and a head H of 28 [m] at a rotational speed of 1350 [rpm].

1.3. Loss mechanisms

The main objective of the hydraulic design of a centrifugal pump is to convert a maximum of the provided power P into useful hydraulic power P_h or, in other words, to determine the lowest possible effort for the given conditions. Losses can be distinguished according to the IEC 60193 standard. The sum of all losses within a pump dissipates into heat. The operating point representing the maximum efficiency of the pump is denoted as the best efficiency point (BEP). The losses can generally be distinguished into

– volumetric,
– disk friction,
– hydraulic and fluid recirculation,
– and mechanical losses.

According to [6], the calculation of all types of losses is subject to uncertainties of approximately 20 to 30%. These losses are very precisely described in the indicated literature. In the following, this comprehensive topic of loss factors is summarized, while focussing on the mechanisms and effects of hydraulic losses. The reason for this measure is related to the performed numerical simulations, as will be described in the following.

The overall efficiency η of a centrifugal pump can be described as

$$\eta = \overbrace{\underbrace{\eta_h}_{CFD} \cdot \eta_v \cdot \eta_{df}}^{TR} \cdot \eta_m \tag{1.4}$$

where η_h stands for the hydraulic efficiency, η_v the volumetric efficiency, η_{df} representing the disk friction efficiency and η_m the mechanical efficiency. In this the overall efficiency applies to the pump commissioned by the customer. The design with the respective pump characteristic is converted to a scale model, which is applied for further evaluation on the test rig (TR). The measurements conducted by the R&D department allow the determination of hydraulic and volumetric losses together with disk friction losses. The application of numerical methods for this work has been confined on the evaluation of the hydraulic losses. Therefore, the losses due to impeller side-wall gaps and annular seals as well as disk friction losses are neglected. This causes that the calculated efficiency by means of numerical methods should be higher than the overall efficiency. In the course of this work it will be shown, that this conclusion is not always confirmed by numerical methods.

1.3.1. Volumetric losses

Volumetric losses are generated within the pump, so that they belong to the internal losses. These losses are caused by all leakages between rotating and stationary components. They can be classified into losses due to:

1. leakage flow Q_{sp} through the annular seal at the impeller inlet
2. leakage flow Q_E through the device for axial thrust balancing

3. additional fluid Q_h may be branched off for auxiliary purposes as hydrostatic bearings, sealing or cooling.

1.3.2. Disk friction losses

This type of loss is generated due to the rotation of the impeller, causing a liquid film between the runner and the rear and front shrouds. The disk rotates in the fluid and causes shear stresses τ on the surface.

Disk friction losses and volumetric losses have not been considered in the numerical evaluation of the pump in this work, so that they are not described in further detail.

1.3.3. Hydraulic losses

Hydraulic losses include all component losses located between the suction and the discharge nozzle generated through friction and vortex dissipation. They include losses in the inlet casing, the impellers, volutes and the outlet casing and reduce the useful head according to $H = \eta_h \times H_{th}$. Converting kinetic energy into static pressure in a volute involves great losses, which may be called mixing losses. Mixing losses are due to the non-uniform velocity distributions in real flows and to further distortion through deceleration of the flow. Non-uniform flow generates losses by turbulent dissipation through exchange of momentum between the streamlines. Flow separation and secondary flows increase these effect. Flow separation and recirculation results in high losses since the kinetic energy within the wake tends to zero while the main flow contains high kinetic energy. These types of losses develop in flows through curved channels, impellers, diffusers and collectors of turbo machines and will be analysed in section 7.2. These losses cannot be predicted theoretically due to their three dimensional flow patterns, so that empirical loss coefficients are used for preliminary calculations. Numerical methods have been continuously developed towards the predictability of such complex flows by means of turbulence models and slowly approach a stage of practical applicability in industry.

The non-uniform flows have a profound impact on the pump's hydraulic efficiency and are generated by various mechanisms, i.e. the transmitted work by the blades. The non-uniformity of the flow is supposed to increase with the blade loading, hence with increasing pressure coefficient or decreasing blade length. Local zones with decelerated flow or even separation on the blade occur at the leading edge. These separations imply zones of stalled fluid with local recirculation, which can be observed in part load at the impeller inlet. Thereby, the stalled fluid partly blocks the available cross section of the flow and high losses are generated through the exchange of momentum between the jet-like through flow and the stalled zones. Curved flow path, as found in radial impellers, contribute also to a non-uniform flow in the curvature of the meridional section and of the blades. Secondary flows are generated by fictitious forces due to Coriolis forces, centrifugal forces and the streamline curvature, as stated in section 1.3.4.

Further, leakages through the seal at the impeller inlet contribute to the non-uniform flow near the front shroud in terms of velocity distribution, local pre-swirl and incidence angles. It is difficult to assess the phenomena within a pump by applying simplified models. Therefore, the hydraulic efficiency is mostly determined from the power balance of a measured pump. For this reason, the actual efficiency of a pump is only known once it is built. The calculated efficiency from the power balance does not allow any statements on the contribution of individual pump components and their losses. Estimations on phenomena within the pump with empirical approaches, such as the three dimensional velocity distribution in the respective components, are only meaningful near the best efficiency point.[6] As will be shown further in this work, the test rig measurements, provided by the R&D department in Graz, were taken as reference for further comparisons with the numerical results.

1.3.4. Partload phenomena

The following section leads to a brief excursus into the analysis of the partload performance of a pump and the identification of the different physical characteristics.

The best efficiency point of well-designed pumps can achieve hydraulic efficiencies up to 95%, while no significant flow separations are identified at this operating point. On the other hand, if we imagine a rotating impeller operating against a closed wall both at inlet and outlet, full recirculation is enforced as shown in Figure 1.3.

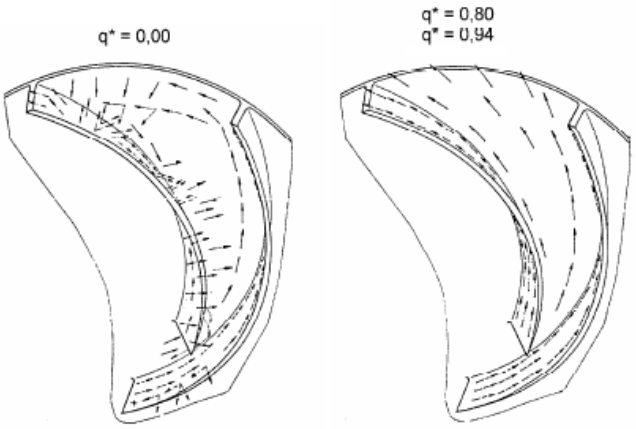

Figure 1.3.: Flow observations ($n_q = 22$) within an impeller channel using a stroboscope; left: closed valve, right: 'attached' flow near best efficiency point.[7]

q^* represents the volume flow through the impeller reffered to the BEP. The flow pattern near BEP follows a streamline similar to the curvature of the blades, whereas zones with separations and recirculation are identified at lower flow rates until q^*. From this, the conclusion can be made that different physical mechanisms of energy transfer from the impeller to the fluid occur between attached flows and fully separated flows.

The flow within an impeller follows curved paths in the absolute frame, which is possible due to a pressure gradient acting towards the momentary center of the streamline curvature. This pressure gradient is responsible for the centripetal force, and subsequently increases the static pressure in the impeller although the flow is accelerated within the absolute reference frame. The pressure field develops according to the maintenance of equilibrium with the body forces. These body forces are generated from the perspective of a rotating system through centrifugal acceleration due to rotation, the Coriolis acceleration and the centrifugal acceleration due to the streamline curvature. The equilibrium of the forces in steady flow condition can be written as

$$\frac{1}{\rho}\frac{\partial p}{\partial n} = \underbrace{2\omega \times w}_{\substack{Coriolis \\ acceleration}} + \underbrace{r\omega^2 \frac{\partial r}{\partial n}}_{\substack{centrifugal \\ acceleration}} - \underbrace{\frac{w^2}{R}}_{\substack{curvature \\ acceleration}} \tag{1.5}$$

being R the momentary radius of the streamline, w the relative velocity, n the normal on the streamline curvature and ω the angular velocity.[6] Equ.(1.5) neglects shear stresses due to wall friction and exchange of momentum between streamlines.

The non-uniform velocity distribution in an impeller is due to flow turning in the meridional section, flow deflection by the blades and boundary layers. To keep the equilibrium of forces at any point, the streamline of a fluid element is adapted and flows develop perpendicular to the main flow. These compensatory perpendicular flows generate secondary flows, which have extensive influence on the performance, hence the losses, and the stability of the characteristic curve of the pump. Following effects define the flow distribution in an impeller:
– Forces acting on the blade as the integral of the pressure distribution over the blade
– Centrifugal forces
– Coriolis forces
– Velocity distribution at inlet of the impeller
– Boundary layers
– seal leakages
– Interactions between impeller and stator during recirculation
Gülich states that shape and stability of the Q-H-curve is hardly affected by the rotor speed, as emerged from various studies in the range of practical interest. This finding allows the conclusion, that the global behavior at partload is barely sensitive to the Reynolds number or to boundary layer effects, even though these are supposed to be responsible for the first local separation. Therefore, non-viscous 3D-Euler calculations are found to reproduce quite well fully developed recirculation, but not the beginning of recirculation.

a) Impeller rotation effects

A fluid element on a curved path is exposed to the component of centrifugal acceleration b_{z1} in direction of w and b_{z2} perpendicular to w, the acceleration due to the curvature of the streamline b_{z3} and the Coriolis acceleration b_c, both normal to w. Figure 1.4 illustrates the forces acting on a fluid element in a radial impeller with back swept blades. The Coriolis force acts in the opposite direction of b_{z2} and b_{z3}. These accelerations perpendicular to the flow direction, are primarily responsible for the velocity distribution in impeller channels. It is assumed that the ratio $\frac{b_{z2}+b_{z3}}{b_c}$, defined as the Rossby number, determines the deflection

of the fluid element whether towards the suction or pressure side of the blade. A Rossby number of close to 1 implies, that no significant flow deflection from the streamline curvature would be expected, whereas a value below 1 would result in a higher influence of the Coriolis force and a flow deflection towards the pressure surface of the blade. Conversely, a Rossby number above 1 implies a deflection of the fluid towards the suction surface of the blade. The influence of the Coriolis force disappears in the boundary layers, since the relative velocity w close to the wall tends to zero and thus Ro tends to infinity. It should be noted that secondary flows also occur in reality at $Ro = 1$, due to the non-uniform flow distribution attributed to the meridional curvature, boundary layers and body forces. An analysis in [6] of a large number of measured velocity profiles at the outlet of radial impellers with back-swept blades did not yield any general tendencies for the prediction of the flow.

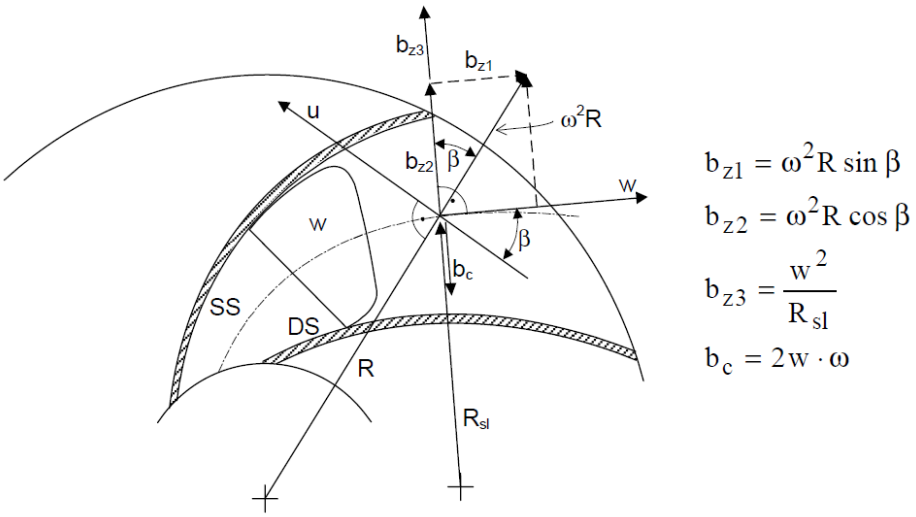

Figure 1.4.: Accelerations acting on a fluid element in a radial impeller.[6]

b) Blade force effects

The flow distribution at the impeller outlet results from a complex equilibrium of the acting forces. Consequently the mean flow angle and slip factor are influenced by different mechanisms:

– velocity differences between pressure and suction surfaces (Fig. 1.4)
– the Coriolis acceleration acts in opposite direction of the rotation and causes a secondary flow. It reduces the flow angle β due to fluid transport towards the pressure surface.
– the difference in static pressure between pressure and suction side immediately downstream the trailing edge disappears, since pressure differences in the free flow are only maintained through different streamline curvatures. Therefore, the velocity distribution already adapts in the triangular section downstream of the throat at a_2 of the impeller outlet, in order to satisfy this outflow condition. Figure 1.5 indicates that the flow is guided more effectively (section k) within the impeller channel and deviates less from the blade angles in comparison to the outlet section s.

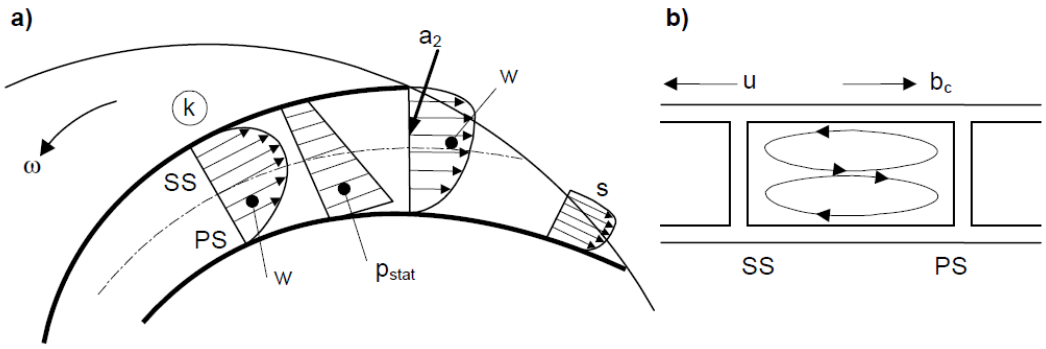

Figure 1.5.: Slip phenomenon in an impeller channel. **a** Flow between the blades; **b** Secondary flow [6]

Energy is transferred to the fluid when a lower pressure prevails, thus when higher relative velocities occur on the suction side, than on the pressure side. The theoretical blade work is obtained from the integral of the pressure distribution on the surface. It is important to consider that the effects of the blade forces and the Coriolis force are opposed to each other. While the maximum relative velocity due to the flow around the blade tends to the suction side (Fig.1.5 section k), the Coriolis force would rather shift the maximum velocity to the pressure surface.[6]

c) Meridional curvature effects

The investigated centrifugal impeller deflects the flow by 90% from the axial entry to the radial outlet. Considering a flow through a simple bend, the highest velocity at the inlet is measured at the inner streamline due to the conservation of angular momentum according to $c \times r = const.$

The pressure in a curved bend decreases from the outside to the inside in direction of the center of the curvature. The forces acting on a fluid element on a curved streamline can be illustrated as follows.

The absolute velocity $c_n(s,t)$ normal to the streamline is a function of time and space. Therefore, we can write for the change in velocity:

$$\mathrm{d}c_n = \frac{\partial c_n}{\partial t}\mathrm{d}t + \frac{\partial c_n}{\partial s}\mathrm{d}s \quad \Longrightarrow \quad \frac{\mathrm{d}c_n}{\mathrm{d}t} = \frac{\partial c_n}{\partial t} + \frac{\partial c_n}{\partial s}\frac{\mathrm{d}s}{\mathrm{d}t} \tag{1.6}$$

Substituting $\frac{\mathrm{d}s}{\mathrm{d}t} = c$ and $\frac{\partial c_n}{\partial s} = \frac{c}{r}$ the acceleration normal to the streamline becomes:

$$\frac{\mathrm{d}c_n}{\mathrm{d}t} = \frac{\partial c_n}{\partial t} + \frac{c^2}{r} \tag{1.7}$$

The equilibrium of the forces perpendicular to the streamline yields:

$$\frac{\partial c_n}{\partial t} + \frac{c^2}{r} + g\frac{\partial z}{\partial n} + \frac{1}{\rho}\frac{\partial p}{\partial n} = 0 \tag{1.8}$$

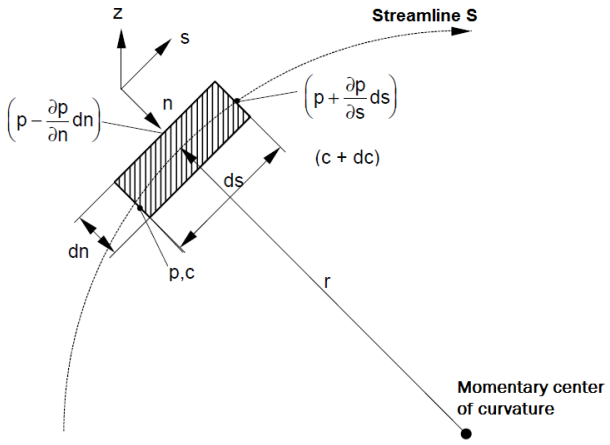

Figure 1.6.: Forces acting on a fluid element [6]

Neglecting gravity and substituting $\mathrm{d}n = -\mathrm{d}r$ we obtain the pressure gradient perpendicular to the flow direction for steady flow according to

$$\frac{\partial p}{\partial n} = \rho \frac{c^2}{r} \tag{1.9}$$

This pressure gradient generates a centripetal force which enables the flow in a bend to follow a curved path in the first place, keeping the centrifugal force at equilibrium.

Considering a rotating channel, secondary flows build up due to centrifugal forces and boundary layers when the fluid progresses through the channel. The centrifugal forces shift the maximum of the velocity distribution near the outlet of the channel towards the outer wall. These mechanisms are applied in Figure 1.7 to the meridional flow of a radial impeller.

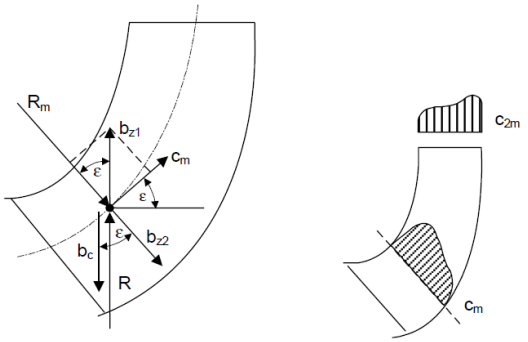

Figure 1.7.: Meridional section of an impeller.[6]

Figure 1.8.: Meridional curvature of the investigated pump, $n_q = 70$

According to Equ.(1.10), the pressure difference between hub and shroud can be calculated using

$$\Delta p = \rho c^2 \frac{B}{R_m} \tag{1.10}$$

where R_m is the radius of curvature of the center streamline and B the local distance between hub and shroud. This gradient is created through the centrifugal acceleration $b_{z2} = \frac{c_m^2}{R_m}$ by the curvature and contributes together with a component of the Coriolis acceleration $b_c = 2w \times \omega$ to deflect the flow towards the hub. These accelerations are opposed by the centrifugal component $b_{z1} = \frac{u^2}{R}$ caused by the rotation of the impeller.

Considering additional effects of blade forces and e.g. backflow from the spiral casing at partload, the flow becomes fully 3-dimensional and unpredictable because of alternating predominant effects at different times. This implies that the maximum velocity distribution can be found either near the shroud, when centrifugal forces predominate in those parts of the blade channels, where the flow has an axial component, or near the hub, when the influence of the meridional curvature is determining the flow.

A centrifugal pump with a specific speed n_q between 50 to 100 is found to be particularly difficult to assess regarding the flow since the blade trailing edges are severe near the zone where the curvatures of the meridional section (Fig.1.8 illustrates the curvature of the investigated pump). This shows, that even though significant developments in numerical calculations and measurement methods have been carried out, still the velocity distribution of a given pump can neither be predicted nor readily explained, unless a distinct mechanism is found to be predominant.

1.3.5. Recirculation in an impeller

At partload, recirculation develops at the impeller inlet, due to backflow of the fluid on the outer streamline from the impeller into the draft tube. In particular, excessive curvatures in the meridional section of the shroud can lead to flow separations. The flow re-enters the impeller closer to the hub and contains a circumferential velocity evoked through energy transfer by the rotating blades. The recirculation arises near the blade edges and generates a circular flow between the impeller channels and the pressure and/or suction side. The recirculated flow can have an impact on the liquid in the draft tube as far as $L/D > 10$ by inducing a pre-swirl to the flow by exchange of momentum. To prevent the recirculating flow of affecting and distorting the measurements, structures have to be considered in order to reduce the deviation from the actual suction pressure. Some recirculation patterns are schematically shown in Fig.1.9. [6]

It is found that two pre-requisites must be fulfilled for triggering recirculation at the impeller inlet, where only one of these is not sufficient, namely:

1. local flow separation
2. high pressure gradients must develop normal to the direction of the main flow

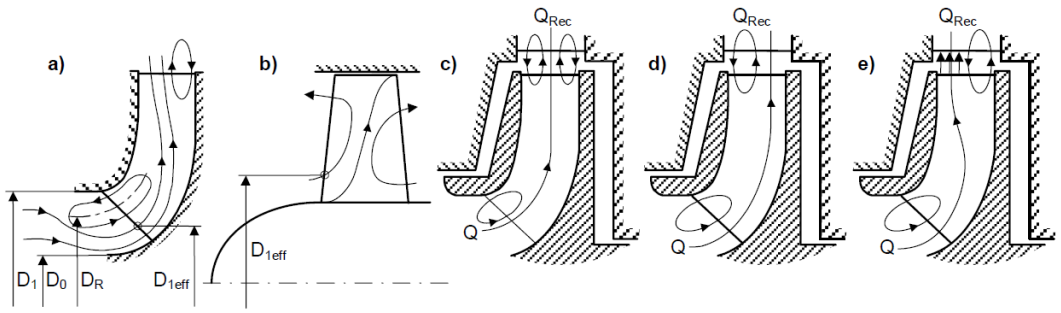

Figure 1.9.: Observed recirculation flow patterns.[6]

Local flow separations depend on boundary layer effects and on the equilibrium of forces, determined by several geometrical parameters and the flow rate. The pressure gradient normal to the direction of the main flow, is also determined by different parameters, such as the ratio of the inner and outer diameters d_{1a}/d_{1i} at the blade leading edge, the curvature of the shroud in the meridional section, the number of blades, the velocity distribution upstream of the impeller etc. Therefore, the pressure gradient results from higher centrifugal forces at the outer streamline and is directed from the hub to the shroud.

Figure 1.9 shows another zone of recirculating flow in an impeller, namely between the impeller outlet and the volute casing. This is caused by the different mechanisms (section 1.3.4) which have major influence on the velocity distribution, and thus cause a strongly non-uniform distribution of c_{2m} and c_{2u} along the circumference.

It should be noted that general methods for the quantitative evaluation of centrifugal pumps in terms of intensity and onset of recirculation have not been found to date.

Recirculation effects on the theoretical head

Based on the example of partload, it is intended in the following to explain why the theoretical head (Equ.(1.11)) of the pump increases with decreasing flow rate. The recirculation at the inlet of the impeller reduces the inlet cross section of the "normal" flow (Fig.1.9), since it blocks the outer region of the impeller inlet, by means of diverting the flow to the hub. This causes a displacement of the effective streamline, which enter the blading on a smaller radius than without recirculation. The effect of recirculation can be explained by using the one-dimensional theory according to the velocity triangles of an impeller at inlet and outlet:

$$H_{th} = \frac{u_2^2 - u_1^2}{2g} + \frac{w_1^2 - w_2^2}{2g} + \frac{c_2^2 - c_1^2}{2g} \tag{1.11}$$

The first term on the right hand side of the equation corresponds to the head component generated by centrifugal forces which depend only on the ratio between the inlet and outlet diameter, thus the circumferential velocity. Due to the reduction of the effective flow inlet area, the velocity u_1 is reduced and increases the centrifugal head component in Equation (1.11). The middle term complies with the head component caused by the deceleration

of the relative velocity in the impeller due to the cross sectional enlargement. The latter term corresponds to the component generated through acceleration of the absolute flow and subsequent conversion in the collector into static pressure through deceleration.

1.3.6. Recirculation in a spiral casing

The volute casing of the examined pump contains two functions: firstly, an efficient conversion of the kinetic energy into pressure in the stator, and collecting the fluid around the circumference of the pump. Near the best efficiency point, a fluid element downstream of the impeller outlet moves according to the conservation of angular momentum $c_{2u} \times r_2 = const$, thus the circumferential velocity drops with growing radius. On the other hand, the static pressure increases from the inside to the outside.

The volute cross sections do not correspond to the impeller outlet velocities in partload and overload operation. Beyond the BEP, radial thrust induces forces on the shaft and on the foundation of the pump which are generated by physical mechanisms. The direction of the flow at the impeller outlet compared to the cutwater camber angle, plays a major role on the recovering efficiency of the casing. The flow angle near the BEP corresponds well to the cutwater camber angle, thus the flow deceleration largely follows the conservation of angular momentum and a nearly uniform pressure distribution can be expected - provided a correct volute design - except for local perturbations around the cutwater. The spiral casing area at partload is too large on the entire circumference of the pump, which decelerates the absolute velocity c_2 according to the local flow rate and area. The approaching fluid causes a local depression in the static pressure and results in a zone with increased turbulence. The static pressure rises in the spiral casing from a minimum downstream of the cutwater to a maximum which is reached near the outlet area. Conversely, at flow rates above BEP the volute section is too small, which causes an acceleration of the flow and a decrease of the static pressure downstream of the impeller. The approach flow angle is too large and generates a flow separation in the discharge nozzle.

Considering the absolute frame, the flow follows a curved path and the local pressure distribution varies along the circumference in order to balance the centrifugal forces induced by the curvature of the flow path (Equ.(1.10)). Therefore, the flow around the impeller blades depends on the actual circumferential position of the blades. The blade forces vary, thus a different lift changes over the circumference and the resultant force yields the radial thrust created by the impeller. This implies that the impeller channels have different flow characteristics at each circumferential position.

The pressure distribution at the BEP varies little over the impeller circumference and yields only a small resultant radial force, whereas the non-uniform flow at partload implies strong variations of the static pressure, generally acting in the direction of the cutwater. Conversely, the resultant force due to the non-uniform flow at overload is found to typically act towards the opposite side of the cutwater, with decreasing static pressure in circumferential direction from a maximum at the cutwater. The radial thrust at BEP can be traced back to asymmetries induced by the flow around the cutwater, geometrical tolerances and friction losses; all of

which are not uniform over the circumference. These effects influence the pressure build-up in the volute depending on the circumferential position.[6]

1.3.7. Q-H-curve instability

A stable operation of a pump requires a head capacity curve that has only a single intersection with the head capacity curve of the hydraulic system in order to define a unique stable operating point. Flow separations in the flow channel of a pump can lead to instability of the characteristic curve. The Q-H-curve is obtained from the theoretical blade work and the losses in various parts of a pump, also depending on the operating point.

The investigated pump in this work shows a specific type of instability due to a trough of the characteristic curve, which is known in the literature as the saddle type or "Type S" instability. This instability was found to occur at $Q_{opt} = 60\,\text{to}\,90\%$. This phenomenon is in agreement with observations conducted in [6] and [22]. In this, simplified models were developed which attempt to describe the flow processes causing instabilities of this pattern.

A saddle is noticeable through a decrease in head when the flow is reduced and indicates that the flow patterns in the impeller and/or diffuser have changed. The velocity distribution within the impeller should develop continuously from the uniform profile at the best efficiency point to the asymmetrical distribution with fully developed recirculation. Sudden changes of the flow pattern should neither occur at the inlet nor at the outlet. In order to avoid instabilities, separation and recirculation zones should remain at the same location at all OP and increase continuously with partload. A sudden change of the flow pattern upon a minor decrease in flow causes a reduction of the head. The obtained results of the FV calculations at partload are shown in Figure 1.10, which indicate the recirculation zones at the impeller outlet. A closer analysis of the transient results revealed a local movement of the recirculation zone between the front and the rear shroud. Similar observations are documented in [22], where this shift in flow separation is accompanied by some hysteresis. During this shift, a flow range is passed where the recirculation almost disappears, causing the effective cross section to increase, and leading to a reduction of the head. Assuming recirculation having a "self-healing" effect by reducing the flow channel so that the remaining channel cross section operates quasi normally, one-sided or asymmetric velocity distributions at the impeller outlet are found to be better than symmetrical distributions. An explanation for that could be the generation of two weak symmetrical recirculation zones in comparison to a one-sided velocity distribution generating a more intensive recirculation. Gülich notes that a Type-S instability *is expected if the recirculation, which immediately follows the separation in the impeller, is not sufficiently intense.*

A hysteresis within the Q-H-curve is caused by the fact that the change of the flow pattern occurs at different values of Q depending on whether the flow rate is reduced or increased. These switching flow patterns can be caused by a delay of separation or a sudden change of the impeller outlet recirculation between the rear and the front shroud. In contrast to the "normal" flow separation which starts as a tiny separation zone and grows continuously, the delayed separation is triggered late, where stalled fluid suddenly covers a large zone. In pump

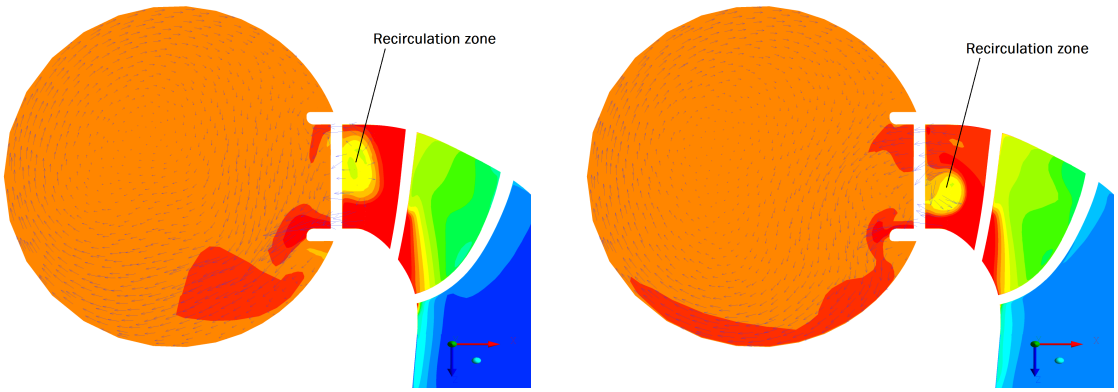

Figure 1.10.: Flow separation zones at impeller outlet (total pressure) - transient results.

application it is crucially important that the minimum head rise produced in the unstable region of the characteristic is above the head rise demanded by the hydraulic system.

The impeller channels of the investigated pump with $n_q = 70$ are relatively short compared to their width, leading to an onset of separation and recirculation near Q_{opt}. Therefore, the flow is found to be in a kind of quasi-stable equilibrium, where the impeller flow and Q-H-curve can react with great sensitivity to changes in the volume flow. The annular seal flow injection also affects the boundary layer on the outer streamline. Systematic investigations of these phenomena are highly elaborate. To determine the real partload head, it is vital to capture the interaction between the impeller and the diffuser correctly.

1.3.8. Mechanical losses

Mechanical losses P_m are caused by bearings, which determine the shaft in radial and axial directions as well as shaft seals. These losses belong to the external losses since no heat is established into the flow. Therefore, these losses mainly depend on the selection of the bearings according to the field of application of the pump.

2. Some Aspects of Numerical Simulation

The following section will give an introduction into the numerical simulation as well as into the theoretical background of the investigated methods, and is based on LIU and LIU[13], FERZIGER and PERIĆ [4] and SANZ [23].

2.1. Numerical simulation

Computational Fluid Dynamics deals with the numerical solution of the governing equations of fluid dynamics in engineering and science. Due to the increase of the computational performance achieved in the last decades it has become an indispensable method for solving complex flow phenomena. Thereby, a physical problem is transformed into a discrete form of the mathematical description and is solved on one or several computers, which reveal phenomena virtually.

An advantage of this discipline is the ability of giving the analysts an alternative tool for scientific investigations, that allows to reduce expensive experiments in laboratories, which can be considered as time consuming and sometimes even dangerous. An approximate numerical solution of a flow phenomena is described by the governing equations (integral or differential equations), which have to be transformed to a system of algebraic equations and solved on computers. These approximations are a set of algebraic equations (or ODEs with respect to time only), which allow obtaining numerical values for the field functions (such as density, pressure, velocity, etc.) at discrete points in space and/or time.[13] The informations obtained allow an insightful disclosure of the investigated field, which often cannot be measured or where experimental investigation simply turns out to be too costly.

A typical numerical simulation of a CFD problem involves the following factor:

1. governing equations,
2. proper boundary conditions and/or initial conditions,
3. domain discretization technique,
4. numerical discretization technique,
5. numerical technique to solve the resultant algebraic equations or ordinary differential equations (ODE)

2.1.1. General numerical simulation procedure

The mathematical models are generally formulated in the form of governing equations with appropriate boundary and/or initial conditions, in order to determine the field variables in space and time. The governing equations can be a set of ordinary differential equations (ODE), partial differential equations (PDE) or integrative equations.

The investigated domain is sub-divided into discrete volumes in order to solve the governing equations. The computational frame for the numerical approximation that is to be solved is discretized by a finite number of volumes which represent the continuum problem.

This frame traditionally consists of a mesh, including grid nodes to evaluate the field variables. Another, more recent developed method is the mesh-free particle description, which employs a finite number of discrete particles to represent the state of a system and to record the movement of the system. The level of discretization for both, mesh-based and mesh-free, methods is closely related to the accuracy of the numerical approximation.

When domain and numerical discretization are applied, a set of algebraic or ordinary differential equations can be obtained out of physical equations, which can be solved by using existing numerical solvers. These methods require a translation of the domain decomposition and numerical algorithms into a computer code, where accuracy and efficiency represent two important parameters. Further considerations might be robustness or consistency of the code, a clear structure, application and modification, etc. To verify the code concerning its applicability on practical problems, it should be done by using experimental data or results from other established methods. These verifications, conducted by MARONGIU and LEDUC, have been elaborated for various practical applications on ASPHODEL (see introduction), as the impingement of a jet on a plate [14] and surface tension models [11]. Since the aim of this work is to apply the SPH-ALE method on pump geometry, the primary focus was the preparation of the code regarding the boundary conditions. This work was performed in collaboration with Dipl. Ing. Magdalena NEUHAUSER, who is writing her PHD thesis on the numerical simulation of transient flows in hydraulic machines by a coupled SPH - finite volume method. [1] I assisted in the preparation and execution of simulations, which enabled me to create and simulate a pump geometry in ASPHODEL. Therefore the aforementioned preliminary simulations were qualitatively compared with existing test cases investigated within the SPHERIC [2] community. They included numerous simulations on simple 2D geometries as cylinders, squares and NACA airfoils. Due to the scope of this study to compare different numerical methods on a centrifugal pump, these two-dimensional test cases were not included in this report.

From the conservation laws we can establish the governing equations for different fluid mechanic problems, where the system field variables such as mass, momentum and energy have to be conserved during the evolution of the flow through the system. The governing equations are a set of mathematical equations which contain the fundamental physical principles of the fluid problem. The behavior of the fluid system is determined by the three

1. PHD thesis by Magdalena NEUHAUSER: *"Simulation Numérique des Ecoulements Transitoires dans les Machines Hydrauliques par une méthode couplée SPH et Volumes Finis."*
2. SPH European Research Interest Community

fundamental principles of conservation together with the conditions at the initial stage and additional information about the nature of the fluid.

2.2. Frame of reference

A velocity field is represented by a regular array of velocity vectors, within which there is a material fluid volume and a control volume. The material volume (Lagrangian frame) is made up of specific fluid elements that are carried along with the flow. The control volume (Eulerian frame) is fixed in space, and the sides are imaginary and invisible as far as the flow is concerned (Fig. 2.1). The fluid material inside a control volume is continually changing, assuming that there is a fluid flow. The essence of a Lagrangian representation is that we observe and seek to describe the position, pressure, and other properties of material volumes; the essence of an Eulerian representation is that we observe and seek to describe the fluid properties inside control volumes. The continuum model assumes that either a material volume or a control volume may be made as small as necessary to resolve the phenomenon of fluid flow.[19]

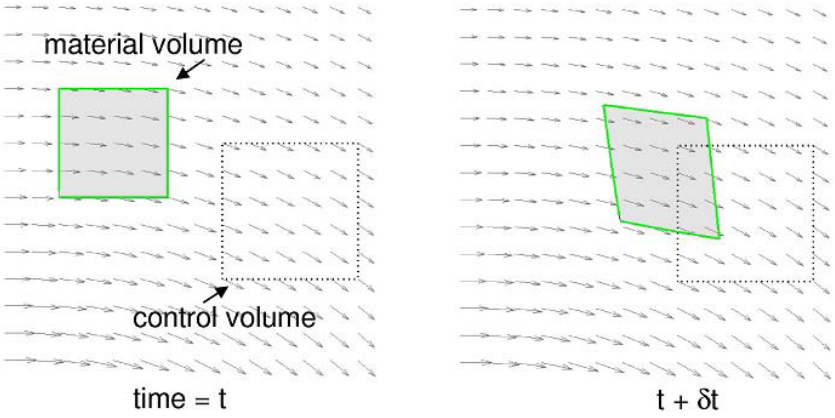

Figure 2.1.: Velocity field.[19]

Lagrangian methods are natural for many observational techniques and for the statement of the fundamental conservation theorems. On the other hand, almost all of the theory in fluid mechanics has been developed in the Eulerian system.

We consider initially two different representations of the velocity vector.

2.2.1. The Euler and Lagrange description

The local coordinates in a fixed Cartesian System are given with $\mathbf{x} = (x_1, \ldots, x_d)$ and the time t. We consider the velocity vector $\mathbf{v} = (v_1, ..., v_d)$. If $\mathbf{v}$ is a function, which assigns a

velocity $\mathbf{v}$ to a particle with position $\mathbf{x}$ and time t, we speak of Euler coordinates. Based on the SPH notation, variables written in bold represent vectors.

$$\mathbf{v} = \mathbf{v}(\mathbf{x}, t) \tag{2.1}$$

This formulation describes the change of a field variable at a fixed point in space. One may also consider a fixed fluid element, which was located at $\mathbf{x}_0$ at the time $t = 0$. This element is being tracked, so that at time t it is located in

$$\mathbf{x} = \mathbf{x}(t) = \Phi(\mathbf{x}_0, t) \tag{2.2}$$

For the velocity vector we obtain

$$\mathbf{v}(\mathbf{x}, t) = \frac{d}{dt}\Phi(\mathbf{x}_0, t) = \frac{d}{dt}\mathbf{x}(t) \tag{2.3}$$

In this context we speak of the Lagrangian coordinates. This description follows the change of a chosen mass point in time.

2.2.2. Material derivative

For a scalar function f, depending on position and time in Eulerian coordinates, we construct for a given position $\mathbf{x}_0$ in Lagrangian coordinates the corresponding function $\tilde{f}$ [2]. We obtain

$$\tilde{f}(t) = f(\mathbf{x}(t), t) = f(\Phi(\mathbf{x}_0, t), t) \tag{2.4}$$

If we consider the derivative of the function $\tilde{f}$, we obtain with the chain rule

$$\frac{d\tilde{f}}{dt} = \frac{\partial f}{\partial t} + \frac{\partial f}{\partial x}\frac{\partial x}{\partial t} + \frac{\partial f}{\partial y}\frac{\partial y}{\partial t} + \frac{\partial f}{\partial z}\frac{\partial z}{\partial t} \tag{2.5}$$

since $\mathbf{x}$ is the particle trajectory and thus $\dot{\mathbf{x}} = \mathbf{v}$, we obtain

$$\frac{Df}{Dt} = \frac{\partial f}{\partial t}(\mathbf{x}, t) + (\mathbf{v} \cdot \nabla f) \tag{2.6}$$

The correlation between Eulerian and Lagrangian coordinates is called the material derivative.

$\frac{Df}{Dt}$ ... variation of the mass point along the particle path = *material derivative*

$\frac{\partial f}{\partial t}$ ... temporal change of the function f in the coincident point in space
= *local derivative*

$(\mathbf{v} \cdot \nabla f)$ ... variation of f at the mass point due to its motion at the velocity $\mathbf{v}$
= *convective derivative*

2.3. Errors in CFD

The following section is dedicated to the definition of errors, occurring in numerical methods.

CFD calculations can lead to considerable differences in the results compared to the actual flow, which is why it is particularly important to define and isolate the errors. It is necessary to specify the bandwidth of errors committed with numerical simulation tools. They often become apparent when comparing the numerical results with experiments and empirical data. The difficulty of determining the errors is apparent, when one considers that only the discretization error can be accurately determined with mathematical methods.[8]

2.3.1. Sources of errors

Several terminologies are proposed by a number of associations, which shows the different perspectives on various applications. In the following, the pertinent definition by the AIAA [1] for numerical simulations is given, which was primarily interested in the accuracy of numerical solutions in numerous fields, as computational mechanics, structural dynamics, as well as computational heat transfer.[16]

AIAA directive:

Verification: The process of determining that a model implementation accurately represents the developer's conceptual description of the model.

Validation: The process of determining the degree to which a model is an accurate representation of the real world from the perspective of the intended use of the model.

A classification of the errors is proposed by Roache [21], who subdivides the errors in modelling, discretization and iterative errors, where the latter two represent the numerical errors.

- modelling error: The modelling error is the difference between real value ϕ_{real} and the exact solution $\phi(x_i, t)$ obtained from fluid dynamic equations. It comprises all simplifications and assumptions conducted for the modeling of the problem, as establishing boundary conditions, material values, time-dependent processes, as well as the choice of the turbulence model. The categorization and quantification of these sources of errors is difficult, and heavily relies on experiences in the respective field.

- discretization error: This error arises due to the approximative approach between the exact solution of the differential equations $\phi(x_i, t)$ and the solution of the discrete linear equations ϕ_i^n. Depending on a consistent discretization scheme, this error should tend to zero, under condition of mesh refinement and smaller time steps.

1. American Institute of Aeronautics and Astronautics

- iterative error: Iterative errors occur due to the application of iterative methods, which can not achieve the accuracy of the exact solution. Roache denotes the solution error as the difference between the exact solution of the discrete linear equations ϕ_i^n and the calculated result $\langle\phi\rangle_i^n$.

The numerical error, hence the sum of discretization and solution errors, arises due to the specification of convergence criterias, rounding errors, as well as bugs within the code.

2.3.2. Modelling error

The purpose of determining the modelling error is to enable an estimation of the impact of various errors on the solution of a CFD calculation. The exact numerical reproduction of a pump geometry is very difficult, and is often limited by the capacity of the available hard- and software. Therefore, simplifications have to be introduced, e.g. coarse resolution of the blade leading edges. It occurs that the final geometry of the pump is determined by the numerical mesh created for the simulation, since mesh generation tools have their peculiarities.

The implementation of the correct boundary conditions for the investigated problem is vital. It is important that the implementation of physical conditions at entry are set correctly, as well as a reasonable distance to investigated domain. For the simulations conducted in this work, the boundary condition at inlet was defined by a velocity deducted from the flow rate, as well as additional parameters according to the chosen k-ω turbulence model. A constant static pressure was defined at the outlet of the pump, which represents a further simplification of the model, since the influence of the pressure line is not considered.[8]

The wall roughness has been neglected in this work, which is also the case in practical applications these days. This means in terms, that the wall conditions were set on 'smooth wall' and 'no slip' conditions, which implies a relative velocity of the fluid at the boundary of null.

A negligible error is committed when defining constant properties, as density and dynamic viscosity, for water. This is a common simplification in the numerical simulation of hydraulic turbo machinery, since the temperature rise due to friction is relatively low.

Runner - Spiral Casing interface

Interactions between rotating and stationary components as they occur in centrifugal pumps, in fact do not permit a quasi-steady-state consideration. Still these methods are often used in practice, since transient calculations are very elaborate and have high demands on the hardware capacities.

Over time a number of methods have been developed in order combine different mesh components, which are moved relatively to each other. The simplest method, therefore, is the simulation of a single impeller channel by imposing periodicity at the circumference. This method is often used to compare individual geometries with each other, by calculating the stationary solution of the flow. The equations are solved in the rotating reference system, where additional fictitious forces are taken into account in the momentum equations. A

disadvantage of this method is the imposition of a uniform circumferential pressure distribution at outlet, which does not correspond to the real flow in pumps. Therefore, the application of constant pressure boundary conditions represents a modelling error that must be considered.

For the numerical analysis of the runner-spiral casing interactions of centrifugal pumps, the Frozen-Rotor and Sliding Mesh methods are frequently applied. These two methods will be explained in section 4.6, since they have been compared in this work.

2.3.3. Numerical error

As stated earlier in this section, the numerical error arises from the sum of the discretization and iteration error. The methodology for the estimation of this error is identical for all numerical calculations. The minimum error of the solution is verified by setting limits on the residuals, as well as by verifying the progress over the iteration history. The discretization error is determined by examining the consistency of the discretization method used. Thereby, a consistent discretization method provides a continuous decrease of the error with finer mesh discretization. The mesh used in this work was provided by the R&D department Graz, which was previously developed with excellent results.

Since this work was confined to the comparison of the methods described earlier in this report, an evaluation of the numerical error was omitted. Basic information about the applied mesh is stated in section 4. Even if the discretization error affects the total error in a small extent, the choice of the turbulence models for the correct wall treatment is of great importance. The fundamentals of the applied turbulence models used for the FV calculations will be described in section 3.2.2.

3. Finite Volume Method

This chapter deals with the fundamentals of FV methods. This method considers the flux balance between adjacent volumes and is therefore conservative. The mathematical description of fluid flow is a closed system of partial differential equations. Unfortunately this system is non-linear so that an exact analytical solution is impossible, except in special cases and is subject to the condition of a number of simplifying assumptions. This is why we try to approach the solution through numerical simulations. The goal is no longer to obtain an analytical solution of the flow but to approximate the pressure field, velocity field, temperature field etc. in a number of points in space and for a specified time, which is called the discrete solution.

3.1. Governing Equations

The following section deals with the conservation principles which are applied to describe a flow field as well as an equation to include the viscous dissipation and friction in the near wall zone. The conservation laws can be derived by considering a quantity of matter or control mass and its extensive properties, namely, mass, momentum and energy. The fundamental variables are rather intensive properties, which are independent of the total amount of matter considered, e.g. density ρ as mass per unit volume or velocity $\boldsymbol{v}$ as momentum per unit mass. This section is based on the book [4].

If ϕ represents any conserved intensive property, then the corresponding extensiv property Φ can be written as:

$$\Phi = \int\limits_{\Omega_{CM}} \rho\phi d\Omega \tag{3.1}$$

where Ω_{CM} denotes the volume occupied by the control mass. For the conservation of mass, ϕ equals 1, and for the conservation of momentum $\phi = \mathbf{v}$. The conservation equation for a control volume - called the Reynolds' transport theorem - can therefore be written as:

$$\frac{d}{dt}\int\limits_{\Omega_{CM}} \rho\phi \, d\Omega = \frac{d}{dt}\int\limits_{\Omega_{CV}} \rho\phi \, d\Omega + \int\limits_{S_{CV}} \rho\phi(\mathbf{v} - \mathbf{v}_0)\cdot \mathbf{n} \, dS \tag{3.2}$$

where Ω_{CV} represents the control volume, S_{CV} the surface enclosing the CV, $\boldsymbol{n}$ the unit vector orthogonal to S_{CV} and directed outwards, $\mathbf{v}$ the fluid velocity and $\mathbf{v}_0$ is the velocity of the moving CV surface. This equation is fundamental for this work, as two different approaches will be employed. The first one is the finite volume method using ANSYS CFX, which considers a fixed control volume with $\mathbf{v}_0 = 0$ and the first derivative of the right hand

side becomes a local (partial) derivative. In words, this equation states that the rate of change of the amount of the property ϕ in the CM, is the rate of change of the property within the control volume plus the net flux of it through the CV boundary due to the fluid motion relative to the CV boundary. If the CV moves with the same velocity of the control mass $\mathbf{v}_0 = \mathbf{v}$, the boundaries coincide and the convective term will be zero. Equation (3.2) represents the general form, which assumes that all fluid and flow properties vary in space and time. In many applications the fluid density can be assumed to be constant, as for flows of liquids and gases with Mach numbers below 0.3.[4] This equation is fundamental for this work and will be discussed in section 6 for the applied SPH-ALE method.

The current state of scientific knowledge considers that the best description of the macroscopic flow of Newtonian fluids available is formed by the system of the Navier-Stokes equations. The conservation laws for mass, energy and momentum form the actual basis of fluid dynamics. These describe the observation that neither mass, momentum or energy can be destroyed or created in a closed system. The Navier-Stokes problem is a mathematical description of the motion of viscous, in case of hydrodynamics, incompressible fluids. By applying these conservation laws to an infinitesimal volume element of a flowing fluid, we obtain partial differential equations. These equations completely describe the three-dimensional flow field which, in general, cannot be solved analytically but only numerically.

3.1.1. Conservation of mass

The integral form of the conservation of mass describes the change of mass through a control volume, by setting $\phi = 1$:

$$\frac{\partial}{\partial t}\int\limits_{\Omega} \rho d\Omega + \int\limits_{S} \rho \mathbf{v} \cdot \mathbf{n}\, dS = 0 \tag{3.3}$$

This equation states that the temporal change of mass of the control volume added with the incoming flow and subtracted by the outgoing flow yields null. In this work the flow is assumed to be incompressible. Applying the Gauss' divergence theorem to the convection term, the surface integral can be transformed into a volume integral if the vector field is continuously differentiable. The conservative form of the continuity equation for incompressible flow can therefore be written as:

$$\int\limits_{\Omega} \nabla \cdot \mathbf{v}\, d\Omega = 0 \tag{3.4}$$

Transforming this equation into the Cartesian form in both tensor and expanded notation, leads to:

$$\frac{\partial v_i}{\partial x_i} = \frac{\partial v_x}{\partial x} + \frac{\partial v_y}{\partial y} + \frac{\partial v_z}{\partial z} = 0 \tag{3.5}$$

where v_i or (v_x, v_y, v_z) are the Cartesian components of the velocity vector $\mathbf{v}$ and x_i (i=1,2,3) or (x,y,z) are the Cartesian coordinates.

3.1.2. Conservation of momentum

According to Newton's 2^{nd} law of motion, the change of the momentum of a mass over time is equal to the vectorial sum of all volume and surface forces $\boldsymbol{f}$ acting on the mass. The conservative variable is the momentum density $\rho\mathbf{v}$. These forces are:
– pressure forces p at the boundaries of the control volume
– friction forces due to wall shear stresses τ
– external forces on fixed walls f_e
– body forces as gravity, centrifugal and Coriolis forces etc.
Applying the Reynolds' transport theorem according to Equ.(3.2), while replacing ϕ by $\mathbf{v}$ for a fixed volume in space, we obtain the momentum conservation equation:

$$\frac{\partial}{\partial t}\int_{\Omega}\rho\mathbf{v}\,d\Omega+\int_{S}\rho\mathbf{v}\mathbf{v}\cdot\mathbf{n}\,dS=\sum\boldsymbol{f} \tag{3.6}$$

The integral form of the momentum conservation equation becomes:

$$\frac{\partial}{\partial t}\int_{\Omega}\rho\mathbf{v}\,d\Omega+\int_{S}\rho\mathbf{v}\mathbf{v}\cdot\mathbf{n}\,dS=\int_{S}\mathbf{T}\cdot\mathbf{n}\,dS+\int_{\Omega}\rho\boldsymbol{f}d\Omega \tag{3.7}$$

where $\mathbf{T}$ represents the stress tensor, as the molecular rate of transport of momentum. The differential coordinate-free form of the momentum conservation equation is obtained again by applying the Gauss' divergence theorem to the convective and diffusive terms:

$$\rho\left(\frac{\partial\mathbf{v}}{\partial t}+\mathrm{div}(\mathbf{v}\mathbf{v})\right)=\nabla\cdot\mathbf{T}+\rho f_e \tag{3.8}$$

The left side of the equation describes the time dependent or/and convective effects, while the right side sums the external forces and the divergence of stress. The investigated fluid is assumed to be Newtonian, which is the case for water. For Newtonian fluids and incompressible flow the stress tensor can be written as:

$$\mathbf{T}=2\,\mu\,\mathbf{D} \tag{3.9}$$

with μ representing the dynamic viscosity and $\mathbf{D}$ the strain (or deformation) tensor according to:

$$\mathbf{D}=\frac{1}{2}\left[\nabla\mathbf{v}+(\nabla\mathbf{v})^{T}\right] \tag{3.10}$$

3.1.3. Conservation of energy

Under consideration of a hydraulic pump and inviscid flows, the third conservation equation, the energy equation is neglected. In order to construct an efficient numerical method, it is necessary to analyze the type of flow that we seek to represent. The Navier-Stokes equations allow a very rich representation of the phenomena involved, but this richness is reflected by both, modelling challenges and higher computational costs. First we try to simulate water flow without major thermal phenomena (heat). The equation of energy conservation thus shows that only the terms of compressibility and viscous stresses are likely to change the temperature. Since water is a liquid, it can be regarded as incompressible (or very low compressible). On the other hand the molecular viscosity of water is very low. The heat capacity of water compared to air is quite high, it requires a large variation of internal energy so that the temperature varies significantly. All these arguments consider that the temperature is constant in the flow. This allows to remove the equation of energy conservation out of the system of equations, which is being solved.

3.2. Turbulence Modelling

This section is addressed to the theory of the applied turbulence models, which describe turbulent flows.

As already stated, flows are completely described by the mathematical relationships of the Navier-Stokes equations. The conservation equations for mass, momentum and energy are valid for both laminar and turbulent flows. The transition from laminar to turbulent flow is defined by the Reynolds number *Re*. This dimensionless number represents the ratio between inertial and viscous forces, where at high Reynolds numbers, as they appear in centrifugal pumps, the influence of viscous forces is low. Analytical solutions of the non-linear Navier-Stokes equations are available only for a few special cases, as in laminar flow layers and for similarity solutions for turbulent flows, but they are often inapplicable for technically relevant flows.
For the calculation of these turbulent flows, different approaches can be applied to describe the stochastic distributions of turbulent flow variables in space and time. Especially in rotating components, these turbulent flows are associated directly with three-dimensional effects. The different characteristics of turbulent flows must be considered by the numerical turbulence models, and must be reproduced in the most accurate manner.

3.2.1. Reynolds Averaged Navier-Stokes equations

The models examined in this work belong to the group of statistical turbulent models - the so-called RANS models. In statistically steady flow, every variable can be written as the sum of a time-averaged value $\overline{\phi}$ and a fluctuation about that value ϕ'.

$$\phi(x_i, t) = \overline{\phi}(x_i, t) + \phi'(x_i, t) \tag{3.11}$$

Therefore, all of the unsteadiness is averaged out and the unsteadiness is regarded as part of the turbulence. It is unlikely that any single turbulence model is able to represent all turbulent flows, which is why they should be regarded as engineering approximations for specific applications. Applying the Reynolds averaging processes described in [4] on the incompressible Navier-Stokes equations yields the RANS equations. Some calculation rules have to be considered as:

$$\overline{\phi} = 0 \quad \overline{\overline{\phi}\psi'} = \overline{\phi'\overline{\psi}} = 0 \quad \overline{\phi'\psi'} \neq 0 \quad \overline{\overline{\phi}\,\overline{\psi}} = \overline{\phi}\,\overline{\psi} \tag{3.12}$$

The averaged continuity and momentum equations can be written for incompressible flows (without body forces) in tensor notation and Cartesian coordinates as:

$$\frac{\partial \rho \overline{v}_i}{\partial x_i} = 0 \tag{3.13}$$

$$\frac{\partial \rho \overline{v}_i}{\partial t} + \frac{\partial}{\partial x_j}\left(\rho \overline{v}_i \overline{v}_j + \rho \overline{v_i' v_j'}\right) = \frac{\partial \overline{p}}{\partial x_i} + \frac{\partial \overline{\tau}_{ij}}{\partial x_i} \tag{3.14}$$

where $\overline{\tau}_{ij}$ represent the mean viscous stress tensor components and $\overline{p}$ the mean static pressure.

New terms appear as $\rho\overline{v_i'v_j'}$ which are called Reynolds stresses. Therefore, the conservation equations are not closed anymore, hence they contain more variables than equations. The exact derivation of the transport equations of Reynolds stress tensor for incompressible fluids yields:

$$\frac{\partial \overline{v_i'v_j'}}{\partial t} + \overline{v}_k \frac{\partial \overline{v_i'v_j'}}{\partial x_k} = \overbrace{-\left(\overline{v_j'v_k'}\frac{\partial \overline{v}_i}{\partial x_k} + \overline{v_i'v_k'}\frac{\partial \overline{v}_j}{\partial x_k}\right)}^{\text{Production } P_k} \overbrace{-2\,\nu \overline{\frac{\partial v_i'}{\partial x_k}\frac{\partial v_j'}{\partial x_k}}}^{\text{Dissipation } \varepsilon} + \overbrace{\overline{\frac{p'}{\rho}\left(\frac{\partial v_i'}{\partial x_j} + \frac{\partial v_j'}{\partial x_i}\right)}}^{\text{Pressure-strain correlation}} \tag{3.15}$$

$$\underbrace{-\frac{\partial}{\partial x_k}\left[\overline{v_i'v_j'v_k'} - \nu\frac{\partial \overline{v_i'v_j'}}{\partial x_k} + \overline{\frac{p'}{\rho}\left(\delta_{jk}v_i' + \delta_{ik}v_j'\right)}\right]}_{\text{Diffusion } D} \tag{3.16}$$

The transport equations of the Reynolds stress tensor now include triple correlations of the unknown fluctuations, causing the closure problem to be shifted to a higher level.[23] In order to close the equations, some approximations are introduced to describe the turbulent stresses with empirical models. A prevalent turbulence model for technical applications is based on the Boussinesq approach, which adds a turbulent viscosity μ_t to the Newtonian viscosity μ, according to:

$$-\rho\overline{v_i'v_j'} = \mu_t\left(\frac{\partial \overline{v}_i}{\partial x_j} + \frac{\partial \overline{v}_j}{\partial x_i} - \frac{2}{3}\frac{\partial \overline{v}_k}{\partial x_k}\delta_{ij}\right) - \frac{2}{3}\overline{\rho}k\delta_{ij} \tag{3.17}$$

where the turbulent kinetic energy is introduced as:

$$k = \frac{1}{2}\overline{v_i'v_i'} \tag{3.18}$$

3.2.2. Turbulence models

The turbulent viscosity is not a material property, but a variable depending on the current local state of the flow. By means of a dimensional analysis, it can be shown that μ_t depends on a characteristic turbulent velocity v_t and a turbulent length scale L_t.

The turbulence models used in this work belong to the group of the two-equation models. Here, the SST turbulence model by Menter is a combination of two models, namely the k-ϵ and the k-ω. These models are well described in their characteristics in [1],[8],[4]. The SST approach uses the advantage of both models by blending and trying to avoid their respective disadvantages. For the purposes of this work, the properties of these models are described briefly.

The k-ϵ model is found to be the most reliable in modelling the flow far from the solid walls. It introduces in addition to the turbulent kinetic energy k the rate of viscous eddy dissipation ϵ. A major weakness of this model is the low sensitivity at unfavourable pressure gradients. In case of overproduction of turbulent viscosity, it may come to a delay or entire absence of boundary layer separations. The k-ω two-equation model of Wilcox solves in addition to the turbulent kinetic energy equation, the turbulent eddy frequency, or the specific dissipation rate, ω. The advantage of this model is a relatively simple formulation within the viscous wall layer by specifying a Dirichlet boundary condition. As a result, this model has proven to be better in accuracy and robustness for solving boundary layer flow and does not require artificial damping close to the wall. A major disadvantage of this model lies in the strong dependence of the turbulent viscosity on the boundary conditions for ω in the free flow.

The blending SST model combines the advantages of each turbulence model, by calculating the inner part of the boundary layer with the k-ω approach and the outer section as well as the remainder of the flow with the k-ϵ model. This hybrid model shows its strength in flows which are exposed to zones with flow separations. Regarding the ability to predict the reattachment of detached flows, no significant improvements were identified.[8]

3.2.3. Boundary layer modelling

The boundary layer contains a zone of low velocity and strong shear in its vicinity, due to the presence of the no-slip condition $v = 0$. This zone has to be modelled in order to resolve the effects in the boundary layer with reasonable computational costs. ANSYS CFX uses a scalable wall function approach to determine the velocity profiles near the wall with a logarithmic relation with the wall shear stresses. The near wall region can be subdivided into three layers, starting with the innermost layer, called 'viscous sublayer'. In this layer the flow is almost laminar-like, and the (molecular) viscosity plays a dominant role. The outer layer is called the fully-turbulent layer, where turbulence plays a major role. Between the viscous sublayer and the fully-turbulent layer, an interim region is identified where the effects of molecular viscosity and turbulence are equally important.[23] The transition zone is characterized by a logarithmic velocity profile according to:

$$v^+ = \frac{1}{\kappa} ln\left(y^+\right) + B \tag{3.19}$$

with the dimensionless velocity v^+, the Kármán constant κ, y^+ the dimensionless distance from the wall and an empirical constant represented by B. The non-dimensional velocity v^+ is obtained by using the following definitions:

$$v^+ = \frac{\overline{v_t}}{v_\tau} \qquad y^+ = \frac{\rho v_\tau y}{\mu} \tag{3.20}$$

where v_t denotes the mean velocity tangent to the wall at a distance y, the shear velocity according to $v_\tau = \sqrt{\frac{\tau_w}{\rho}}$. Two approaches are applied to model the near-wall region. In the first approach called the 'wall-function' approach, the viscosity affected inner region (viscous sublayer and buffer layer) is not resolved. Instead, semi-empirical formulas called wall functions are used to bridge the viscosity-affected region between the fully-turbulent region and the wall. This obviates the need to modify the turbulence models to account for the presence of the wall. In the second approach, the turbulence models are modified to enable the viscosity-affected region to be resolved with a mesh all the way to the wall, including the viscous sublayer. This method is termed 'near-wall modeling' approach. The wall-function approach is robust, economical and reasonably robust, but is inadequate in situations where the low-Reynolds-number effects are pervasive in the flow domain. Such situations require near-wall models that are valid in the viscosity-affected region and accordingly integrable all the way to the wall.[23] The applied SST model takes advantage of the fact that the k-ω model used in the boundary layer leads to a stable numerical solution without arbitrary damping factors required to apply k-ε models close to the wall. It allows to resolve the boundary layer consistently using mesh resolutions down to the viscous sublayer.[1]

4. ANSYS CFX

ANSYS CFX is a high-performance fluid dynamics program that has been applied to solve wide-ranging fluid flow problems. This commercial software based on the finite-volume-method is used at the R&D department for the numerical evaluation of different pump models.[30] The following section describes the investigated model in this work and describes also the specified settings for the numerical simulations. The relative motion between rotating and static components is modelled with the FR approach and the transient runner motion using the sliding mesh method. Both methods will be evaluated considering their ability to predict the flow within a centrifugal pump.

The following table gives information of the mesh, provided by the R&D department. Basically the model is divided into three components: draft tube, runner and spiral casing.

	Nodes	**Elements**	**Surfaces**
DT	673.027	663.552	59.520
RN	1.126.818	1.064.448	156.384
SC	777.999	729.388	96.474
SC_SEP	67.602	65.088	4.768
Global	2.645.446	2.522.476	317.146

Table 1: Mesh information.

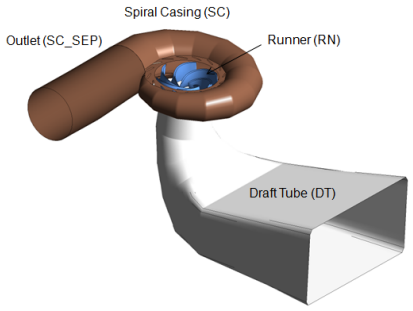

Figure 4.1.: Pump model.

4.1. Draft Tube (DT)

The *inlet* condition was set at the intake of the draft tube with the specified cartesian velocities. Further, the SST and k-ω turbulence model were selected with the respective turbulent kinetic energy k and the turbulent eddy frequency ω. The boundary condition for the solid walls was defined with the 'no slip wall' type, the wall roughness was set on 'smooth wall'. The fluid adjacent to the wall assumes the velocity to be zero at the wall. This corresponds to the prototype, where the impeller channels were improved through additional finishing. In turn, 'free slip wall' would imply a shear stress of zero at the wall and the fluid velocity is not retarded by any wall friction effects near the wall. The configuration was established without buoyancy and with the Shear Stress Transport (SST) turbulence model. A comparison of the SST model with the $k-\omega$-model from Wilcox was performed, to show the difference and advantages. The turbulence option for the fluid was set on 'Medium

Intensity and Eddy Viscosity Ratio', where medium stands for a turbulence intensity of 5% and viscosity ratio of 10.

The mass and momentum model at the interface between the draft tube and the runner was set on 'Conservative Interface Flux'. This implies that the quantity in question is flowing between the investigated boundary and the boundary on the other side of the interface, which means that the conservative interface flux must be used on the other side of the interface.

4.2. Runner (RN)

The domain motion of the runner was set on *rotation* with an angular velocity of 141.7 $\left[\frac{rad}{s}\right]$ and the 'Alternate Rotation Model'. This is a model for the advection term in the momentum equation, which modifies the advection term so that it involves the absolute frame velocity u_{abs} instead of the relative frame velocity u. The main advantage of this model appears when the absolute frame velocity is constant, but the relative frame velocity has a high swirl component. In that case, the advection of the relative frame velocity would have a high component of error, while advecting a constant absolute frame velocity will have less error.[30]

The type of interface was set for both interfaces, DT/RN_{LP} and RN_{HP}/SC, with 'Conservative Interface Flux' and the interface type 'Fluid Fluid'. The interface model 'General Connection' connects the non-matching grids between DT, RN and SC, which is needed here due to the stationary frame of reference of the DT and SC on one side and the rotating frame of reference of the RN on the other side. This allows to select three types of 'Frame Change/Mixing Model', namely, Frozen Rotor, Stage and Transient Rotor Stator. The stage model is the most common used in the R&D department, which is why the other two methods were chosen in this work for comparison. More to the analysis is described in section 7.

Another detail has to be specified when choosing the General Connection, which is the pitch change. The mesh connection method was set on GGI, which stands for General Grid Interface. This method is used for grid connections, where the grid on either side of the connected surfaces are incompatible. This connection is made in a conservative and implicit manner, even if the nodes do not match. It handles also the case, where the connected regions differ in their size, by connecting the mutually overlapping surfaces. According to the CFX manual, even in the case that the surfaces do not fit perfectly together (e.g. a gap) conservation is guaranteed and strictly enforced. In this context, it is recommended by the developers of CFX to use the 'Direct Intersection Control'. It suggests an exact computation of the area fractions, and is faster and more accurate than the bitmap method. However, it will be shown in section 7.3.5 that inappropriate values are obtained at these GGI interfaces of the investigated pump model.[30]

4.3. Spiral Casing (SC) with outlet (SC_SEP)

The SC geometry was set in stationary domain motion and with a static pressure of 0 [Pa] at the outlet. The turbulence model was set to the SST model with 'Medium Intensity and Eddy Viscosity Ratio'. The interface was similarly initialized as the previously described RN.

4.4. Modelling errors

The modelling errors (see 2.3.2) of this simulation of the pump with a FV method are as follows:

– no consideration of impeller sidewall gaps
– constant static pressure at the spiral casing outlet
– manufacturing inaccuracies, e.g. narrow curvatures

4.5. Boundary conditions

The initial conditions for the numerical calculation of the pump were provided by DI. Michael Buchmayr, who has already carried out numerous comparisons with OpenFOAM. The nomenclature was adopted for the configuration and the results from the ANSYS CFX calculations were used for further comparison with the results obtained from OF. In addition to the comparison of the characteristic of the pump, an evaluation of the numerical errors was carried out. Detailed analysis of the comparison of individual interfaces between rotating and stationary domains took place. These results are not included here, as they will be published by the author at a later stage.

For the calculation of the initial conditions u, k, ω, information was required regarding the dimension of the pump (D_1, D_2, b_2), the inlet cross-section of the draft tube and the rotational speed of the impeller. Depending on the specified flow rates, multiple operating points were obtained, providing the initial conditions for preprocessing of the methods used.

4.6. Steady/Transient calculation

In order to simulate the relative motion between the components, as well as their influence on the flow, it is required to consider the entire centrifugal pump. This becomes more obvious if one considers our model, where the flow is collected after the impeller in the spiral casing, which consists of a variable cross-sectional geometry. Generally, there are three types of GGI frame change connections available in ANSYS CFX-5, namely Stage, Frozen-Rotor and Transient Rotor-Stator. In the following, the latter two methods are discussed.

4.6.1. Frozen-Rotor

The FR method makes no geometric simplifications, however, this method makes use of different reference systems. The rotating and static components are calculated each in a stationary frame, so that the grid is not rotated. The coupling is realized at each node of the interface by means of transformation of the velocity vector from the relative system of the runner to the absolute system of the spiral casing. This leads to the term "frozen" since the relative position of the individual components during the calculation remains unchanged. This method does not consider the transient terms of the Navier-Stokes equations. The result of the flow pattern is somewhat of a snapshot of the flow inside the pump.

The conservation equations stated in section 3.1 in vector form are applicable for any coordinate system. The simulations performed in this work were carried out under the assumption of an incompressible fluid without heat exchange, whereby the energy equation is not solved.[8] The conservation equations are written for the inertial system, and shall hereinafter be converted into a rotating frame of reference, as it is of great significance for the calculation of flows in turbomachinery.

The solution of the equations of motion in the rotating frame of reference must take the rotational acceleration into account, by considering additional terms in the momentum equation. It can generally be stated that the relative system can be exposed to a translation with the velocity $\mathbf{v}_t$ and a rotation with an angular velocity ω. Thus, the absolute velocity $\mathbf{c}$ of the inertial system is composed of the relative speed $\mathbf{w}$ and the local vector $\mathbf{r}$ in the relative system. It can be written as:

$$\mathbf{c} = \mathbf{v}_t + \mathbf{w} + \omega \times \mathbf{r} \tag{4.1}$$

In the case of a rotating impeller, the translation $\mathbf{v}_t$ is zero. Additional terms appear in the rotating system in the momentum equation, which act as body forces. These forces are fictitious forces because they are not due to external forces and act only on the observer in the relative system. In this case the term $2\rho\,(\omega \times \mathbf{w})$ denotes the Coriolis force. The Coriolis force acts in the opposite direction of the rotation in the tangential direction, which deflects a fluid particle to the blade pressure side. The term $\rho\omega \times (\omega \times \mathbf{r})$ represents the centrifugal force which acts radially outward. These two fictitious forces are zero, if the relative system does not rotate (hence $\omega = 0$). The continuity and momentum equations for the rotating reference frame can be written as:

$$\frac{D\rho}{Dt} = \frac{\partial \rho}{\partial t} + \nabla \cdot (\rho \mathbf{w}) = 0 \tag{4.2}$$

$$\rho \frac{D\mathbf{w}}{Dt} = -\nabla p + \rho f_e - 2\rho\,(\omega \times \mathbf{w}) - \rho\omega\,(\omega \times \mathbf{r}) + \nabla \cdot T \tag{4.3}$$

The frozen rotor method is considered as robust and a good compromise between computational effort and costs, but the results are often inapplicable for transient flows. A disadvantage is the influence of the impeller position on the results. Since the impeller rotation is not subjected to real motion, the position of the rotor blades to the stator has significant influence on the observed phenomena. The position of the impeller was calculated for a single angular

position, which was chosen arbitrarily. Gugau notes that the FR method basically allows the consideration of interactions between static and rotating components, however, according to his studies, this method leads to better results for radial turbines than for pumps.[8]

4.6.2. Sliding mesh method

The previously mentioned modelling error is almost entirely repealed through the application of the sliding mesh method. The coupling of the sections in the absolute system takes place directly via an auxiliary surface. This auxiliary surface is regenerated at each time step and allows conservative transfer of flows at the interface. The impeller grid is rotated relative to the stationary components at each time step. The rotation angle results from the selected time step and the rotational speed of the impeller. Depending on the specified minimum residuals, a solution is determined for each time step. Merging the individual time step results allows a time-dependent calculation of the overall solution, and subsequently enables averaging the integral values $(Q, H, \dots)$ over a defined number of revolutions. This method allows the calculation of transient flows in turbo engines and comes closest to real physical phenomena. A significant disadvantage is the increased demand for computation and evaluation time.[8] The transient simulations conducted in this work required between 1 and 4 weeks. This represents a clear disadvantage compared to the quasi-stationary frozen-rotor method, which claims between 2 and 4 days, and also requires less computational resources to perform the simulations of 17 operating points, compared to 4 transient OP calculations.

The evaluation of the results is described in chapter 7.

4.7. Frozen-Rotor Settings

The analysis type of the simulation was chosen for the first simulation run with 'Frozen Rotor'. The first step was the adaptation of the queuing script used at the R&D department to launch multiple simulations at a time. The values for u, v, w, k, ω have to be defined for each operating point of the pump, which is to be investigated. In this case a number of 17 operating points was chosen to be evaluated for both turbulence models used.

The flow direction at inlet of the calculated domain, which corresponds to the draft tube inlet, is set perpendicular to the inlet boundary. The characteristic curve of the pump was determined between $0.4 \leq Q/Q_{opt} \leq 1.33$. At the outlet of the pump, a static pressure of $p_{stat} = 0\,[\text{Pa}]$ was specified. The turbulent parameters k and ω were obtained according to equations (4.4) and (4.5)

Turbulent kinetic energy:
The turbulent kinetic energy per unit mass k was calculated for the boundary condition according to the equation below. This equation represents a rough approximation for the inlet distribution of k since no other data were available at the beginning.

$$k_{DT\_LP} = \frac{3}{2} \cdot (u_{avg} \cdot I)^2 \qquad \left[\frac{m^2}{s^2}\right] \tag{4.4}$$

where I denotes the intensity of the turbulence. The turbulence intensity is defined as the ratio of the velocity fluctuation u' and the average velocity of the flow u_{avg}.[27]

Turbulent eddy frequency (dissipation):
The second BC of the turbulence models is for the turbulence frequency $\omega = k/\epsilon$ according to

$$\omega_{DT\_LP} = \frac{\sqrt{k}}{C_{\mu}^{1/4} \cdot l} \qquad [Hz] \tag{4.5}$$

where l represents the turbulence length scale, which is a physical quantity related to the size of the large eddies that contain energy in the turbulent flows. It is assumed to have a fully developed flow at the inlet of the draft tube. Therefore, a relationship between l and the relevant dimension of the duct L can be approximated, according to $l = 0,07 \cdot L$. The factor *0,07* is based on the maximum value of the mixing length in fully turbulent pipe flow.[31]

Solver Control settings

The following tables summarize the settings of the conducted simulations. More information can be found in the appendix. The configuration for the Solver Control in ANSYS CFX was set:

Advection scheme	▷ High Resolution	
Turbulence Numerics	▷ High Resolution	
Convergence Control	▷ min. Iterations	5
	▷ max. Iterations	1000
	▷ Fluid Timescale Control	Local Timescale Factor = 10
Convergence Criteria	▷ Residual Type	Max
	▷ Residual Target	1.E-5
	▷ Conservation Target	Value = 0.005

The configuration for the Execution Control was set:

Partitioning Details	▷ MeTIS
Partitioning Weighting	▷ Automatic
MeTIS Type	▷ k-way

These are settings which are preferably used in the R&D department.

To launch the simulations on the cluster for multiple operating points, some specifications have to be set: the number of the processors used for the simulation, the different boundary condition parameters for each operating point and other configurations concerning the scripts.

The results were obtained in form of different output-files, which enabled a more detailed analysis and are shown in section 7.3.1.2.

4.8. Transient calculation settings

The same pump model was applied for the transient calculations using the SST turbulence model, which required adaptations in the starting script. The implementation of the turbulent kinetic energy k and turbulent eddy frequency ω were enabled, as well as an inlet velocity as initial condition. This allowed the import of data for different operating points by launching the initial condition script. Before these simulations were started, some changes had to be made in the CFX-Pre settings. The analysis type was set to *transient* mode, and different simulation parameters were defined, which are based in large extent on experiences of the developers of the R&D department. The transient calculations were launched by using the results obtained from the Frozen Rotor run. On the basis of 500 completed iterations, the transient calculations were launched with the following settings.

Time steps	▷ Adaptive	update time = 0.042
Timestep Update Frequency	▷ 1	
Time step adaptation	▷ Numeric Coeff. Loops	
	▷ Min. Timestep	2.3E-5
	▷ Max. Timestep	2.3E-3
	▷ Target Min. Loops	2
	▷ Target Max. Loops	4
	▷ Timestep decrease factor	0,8
	▷ Timestep increase factor	1,06
Initial Time	▷ Automatic with value	0 [s]

The settings for the mesh are based on the previous Frozen Rotor settings.

Solver Control settings

The configuration for the Solver Control of the transient calculations was set:

Advection scheme	▷ High Resolution	
Transient scheme	▷ Second Order Backward Euler	
Timestep initialization	▷ Automatic	
Turbulence Numerics	▷ High Resolution	
Convergence Control	▷ min. Iterations	1
	▷ max. Iterations	50
	▷ Fluid Timescale Control	Coefficient Loops
Convergence Criteria	▷ Residual Type	RMS
	▷ Residual Target	1.E-5
	▷ Conservation Target	Value = 0.005

5. Smoothed Particle Hydrodynamics (SPH)

The following chapter deals with the so-called Smoothed Particle Hydrodynamics method. The SPH method has been developed by Monaghan, Lucy and Gingold in 1977 originally intended for astrophysical applications, and VILA [28] (1999) extended the method to an Arbitrary Lagrange Euler formulation. These developments were adopted by J.C. Marongiu and further developments together with J. Leduc led to a code named ASPHODEL.

The following summarizes the different approaches to this method in this work.

Finite Volume Method

The calculation of the flow balance using the finite volume method is achieved by performing an integration on the boundary surface of the discretized cell (Fig.5.1). The entering flux into the volume is identical to that leaving the adjacent volume, so that this method is considered to be conservative. Thus, the control volume is closed and the area of each surface element is known ($\sum S_j \mathbf{n}_j = 0$).

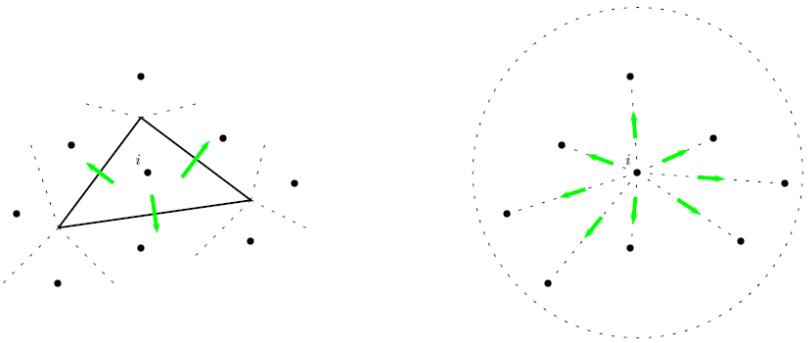

Figure 5.1.: Flow balance integration methods. left: finite volume method, right: smoothed particle hydrodynamics.[14]

SPH

The calculation of the flow balance is performed in a different way, namely by performing a volumetric integration over the domain. The kernel function contains a number of calculation points, referred to as particles. These particles have a spatial distance over which the flow properties are smoothed by the kernel function. The physical quantity of any particle is calculated by summing the relevant properties of all particles which lie within the range of this function. The contribution of each particle is weighted according to their distance from the particle of interest. Generally one can say that the kernel function is a Gaussian function. Cubic splines are used in order to obtain a function which is zero for particles with greater distance. This is a major difference to the mesh based methods.

5.1. The standard SPH method

The following section describes the standard SPH method and will further lead to the ALE formalism used for the code ASPHODEL, which has been developed at ANDRITZ HYDRO Vevey. It will explain the basics of the meshless numerical scheme, which will be adapted for the numerical simulation of flows. The literature for this section is based on [14],[13] and [11].

This numerical method is based on the reconstruction of a scalar or vector field from discrete values within a domain. This method uses a so-called smoothing function in order to interpolate the field variables of the domain. A 'kernel' function approximates a field value at one point by a weighted average of the values in vicinity. The formulation of SPH is divided into the *kernel* and the *particle approximation*, as described in the following.

5.1.1. Kernel approximation

The integration of an arbitrary function and a smoothing kernel function gives the kernel approximation. The function is then approximated by the total of the values of the nearest neighbours in order to obtain the particle approximation of the function at a discrete point.

5.1.1.1. Integral representation of *f*

The concept of an integral representation of a function $f(x)$ used in the SPH method starts from the following identity. At any point in space Ω and at the border $\partial\Omega$, the value taken by f can be written as the product of f with the Dirac function δ.

$$f(x) = \int_{\Omega} f(x')\,\delta(x - x')\,dx' \tag{5.1}$$

where f is a function of the three-dimensional position vector $\mathbf{x}$, and $\delta\left(\mathbf{x} - \mathbf{x}'\right)$ is the Dirac delta function given by

$$\delta(x - x') = \begin{cases} 1 & x = x' \\ 0 & x \neq x' \end{cases} \tag{5.2}$$

Equation (5.1) implies that a function can be represented in an integral form. This integral representation is exact since the Dirac delta function is used, as long as $f(x)$ is defined and continuous in Ω.

If the Delta function kernel $\delta\left(\mathbf{x} - \mathbf{x}'\right)$ is replaced by a smoothing function $W\left(\mathbf{x} - \mathbf{x}', h\right)$, the integral representation of $f(x)$ is given by

$$\langle f(x)\rangle_h = \int_{\Omega} f(x')\,W(x - x', h)\,dx' \approx f(x) \tag{5.3}$$

where W represents the *smoothing kernel function*. In the smoothing function, h is the smoothing length defining the influence area of the smoothing function W. As long as W is not the Dirac function, the integral representation in Equation (5.3) can only be an approximation. This formula represents an approximation of Equ.(5.1) in proportion to the weights of the adjacent points which rapidly decrease with the distance to x. This is typically achieved by using kernel functions of the Gaussian type. The Gaussian function itself can be used, but it has the disadvantage of having an infinite support. It thus involves all points in space in the calculation of Equ.(5.3) even if the weights of the distant points tend to zero. For this reason, other functions with compact support are used, which are briefly discussed in section 5.1.3. In the SPH convention, the *kernel approximation operator* is marked by the angle bracket $\langle\rangle$.

The smoothing function should satisfy a number of conditions. The first one is the *normalization condition* that states

$$\int_{\Omega} W(x - x', h)\, dx' = 1 \tag{5.4}$$

This condition is termed as the *unity condition* since the integration of the smoothing function produces the unity.

The second condition which has to be satisfied is the *Delta function property* that is observed when the smoothing length approaches zero.

$$\lim_{h \to 0} W(x - x', h) = \delta(x - x') \tag{5.5}$$

The third condition is the *compact condition*

$$\int_{\Omega} W(x - x', h) = 0 \text{ when } \mid x - x' \mid > \kappa h \tag{5.6}$$

where κ is a constant related to the smoothing function for a point at x, and defines the non-zero or effective area of the smoothing function. This effective area is called the *support* domain for the smoothing function of point x. Using the compact condition, the integration of the entire problem domain is localized as an integration over the support domain of the smoothing function. Therefore, the integration domain Ω is usually the same as the support domain.

The fourth condition is the *symmetric condition*, which is generally regarded as satisfied when using kernel function pairs.

$$\int_{\Omega} (x - x') W(x - x', h)\, dx' = 0 \tag{5.7}$$

It guarantees the reproducibility of linear functions. Under these conditions, the method of reconstruction (Equ.5.3) described above is therefore of spatial accuracy of second order. It is important to understand now that in case the integration domain is truncated, that is to say, when the reconstruction point $\mathbf{x}$ considered is close to the boundary of the calculation, the conditions (5.4) and (5.7) are no longer satisfied with a symmetric kernel function W, and this simple method of reconstruction is no longer of the same degree of accuracy.

Fifth, the kernel function must also be positive throughout the entire support domain and be monotonically decreasing with distance to the point of interest to realize a local average.

The sixth and last condition a smoothing function should satisfy is, to be a continuous and differentiable function.

5.1.1.2. Integral representation of the gradient of *f*

A major advantage of SPH is the possibility to calculate the gradient of a field using discrete values taken in the field without making assumptions on the spatial distribution of these points. The approximation of the spatial derivative $\nabla \cdot f(x)$ gives, when substituting $f(x)$ with $\nabla \cdot f(x)$ from equation (5.3)

$$\langle \nabla f(x) \rangle = \int_{\Omega} \left[\nabla f(x') \right] W(x - x', h)\, dx' \tag{5.8}$$

Integration by parts leads to:

$$\langle \nabla f(x) \rangle = \int_{\Omega} \nabla \left[f(x')\, W(x - x', h) \right]\, dx' - \int_{\Omega} f(x')\, \nabla W(x - x', h)\, dx' \tag{5.9}$$

where the first integral on the right hand side of equation (5.9) can be converted by using Green's theorem, which transforms the integral into a surface integral

$$\langle \nabla f(x) \rangle = \int_{\partial\Omega} f(x')\, W(x - x', h)\mathbf{n}\, dS - \int_{\Omega} f(x')\, \nabla W(x - x', h)\, dx' \tag{5.10}$$

where $\mathbf{n}$ is the unit normal vector to the surface S. Thus, this equation has a surface and a volumetric contribution. In most practical applications of SPH, it is convenient to use the kernel function with compact support because of its efficiency. We consider now a kernel function W with compact support. The parameter h is introduced as a measure of this support of the function W at x, which we denote by $D(x)$. Since the smoothing function W is defined to have compact support the surface integral becomes zero when the integrated domain is located within the problem domain. If the integrated domain is not fully contained in the calculated domain, the smoothing function W is truncated by the boundary and the surface integral is no longer zero (Fig.5.2). We obtain

$$\langle \nabla f(x) \rangle = \int_{\partial D(x)} f(x')\, W(x - x', h)\mathbf{n}\, dS - \int_{D(x)} f(x')\, \nabla W(x - x', h)\, dx' \tag{5.11}$$

where $\partial D_{(x)}$ is the intersection of the integrated domain D with the boundary $\partial\Omega$.

In the case of a point being sufficiently far from a boundary, using a compact support makes it possible to have no surface influence. On the other hand, if we impose a field boundary condition of zero, such as imposing a pressure $p = 0$ for free surface, the contribution of

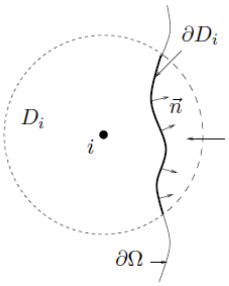

Figure 5.2.: Domain truncation caused by the boundary of the investigated domain.[14]

the surface integral vanishes also for the calculated points close to such a boundary of the problem domain. That is why the standard SPH formalism is reduced to

$$\langle \nabla f(x) \rangle = - \int_{D(x)} f(x') \, \nabla W(x - x', h) \, dx' \tag{5.12}$$

and using the symmetry of the kernel function leads to

$$\langle \nabla f(x) \rangle = \int_{D(x)} f(x') \, \nabla W(x' - x, h) \, dx' \tag{5.13}$$

5.1.2. Particle approximation

Another key operation in the SPH methods is the particle approximation, where the entire system is represented by a finite number of particles, where each one carries mass and occupies space.

The continuous integral representations of the kernel approximations (Equ.(5.3)) can be converted to discretized forms of summation over all the particles in the support domain (Fig.5.3). The infinitesimal volume $d\mathbf{x}'$ in the integration at the location of particle j is replaced by the finite volume of the particle ΔV_j that is related to the mass of the particles m_j by

$$m_j = \Delta V_j \cdot \rho_j \tag{5.14}$$

where ρ_j is the density of particle j (=1, 2, ..., N) in which N is the number of particles within the support domain of particle j.

In practice, this method means integrating the product $f \cdot W$ by a method of rectangles or Riemann sum. We obtain for a point $\boldsymbol{x}$ distant from the boundary $\partial\Omega$ the particle

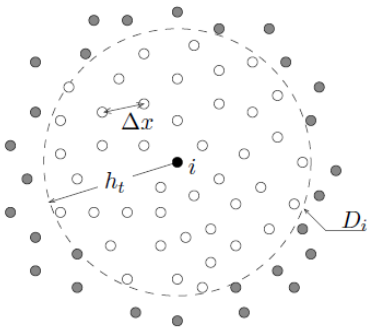

Figure 5.3.: 2D representation of the support domain and the considered adjacent particles.[14]

approximation:

$$\begin{aligned}\langle f(x)\rangle &= \int_D f(x')\, W(x-x',h)\, dx' \\ &\approx \sum_{j=1}^{N} f(x_j) W(x-x_j,h)\Delta V_j \\ &\approx \sum_{j=1}^{N} f(x_j) W(x-x_j,h)\frac{1}{\rho_j}\left(\rho_j \Delta V_j\right) \\ &\approx \sum_{j=1}^{N} f(x_j)\, W(x-x_j,h)\, \omega_j\end{aligned} \tag{5.15}$$

where N is the number of particles within D and ω_j is the mathematical weight associated to each point. ω_j has the meaning of a volume in 3D, which is calculated with $\omega = (area\, of\, base) \cdot height$. Height is the height of a layer of particles, which is usually equal to the targeted discretization size. Further, the particle approximation for a function at particle i can be written as

$$\langle f(x_i)\rangle = \sum_{j=1}^{N} f(x_j)\, W_{ij}\, \omega_j \tag{5.16}$$

where

$$W_{ij} = W(x_i - x_j, h) \tag{5.17}$$

Equation (5.16) states that the value of the function at particle i is approximated using the average of those values of the function at all the particles in the support domain of particle i weighted by the smoothing function.

For the spatial derivative of the function, we obtain

$$\langle \nabla f(x) \rangle = \sum_{j=1}^{N} f(x_j) \nabla W(x - x_j, h) \omega_j \tag{5.18}$$

where the gradient ∇W in equation (5.18) is taken with respect to the particle j. The particle approximation for a function at particle i can finally be written as

$$\langle f(x_i) \rangle = \sum_{j=1}^{N} f(x_j)\, W_{ij}\, \omega_j \tag{5.19a}$$

$$\langle \nabla f(x_i) \rangle = \sum_{j=1}^{N} f(x_j) \nabla_i W_{ij}\, \omega_j \tag{5.19b}$$

$$W_{ij} = W(x_i - x_j, h) = W(\mid x_i - x_j \mid, h) \tag{5.19c}$$

$$\nabla_i W_{ij} = \frac{x_i - x_j}{r_{ij}} \frac{\partial W_{ij}}{\partial r_{ij}} = \frac{x_{ij}}{r_{ij}} \frac{\partial W_{ij}}{\partial r_{ij}} \tag{5.19d}$$

where r_{ij} is the distance between particle i and j.
Substitution of the function $f(x)$ with the density function ρ in equation (5.19a), the SPH approximation for the density is obtained as

$$\rho_i = \sum_{j=1}^{N} m_j\, W_{ij} \tag{5.20}$$

This equation is often referred to as *summation density approach*. It should be noted that W_{ij} has a unit of the inverse of the volume. The equation above states that the density of a particle is a weighted average of those of all the particles in its support domain.

The SPH method is essentially a mathematical tool able to handle discrete data on a set of points of disordered discretization. This makes it very flexible to use and enables it to manage a large deformation of the mesh. By that, it appears appropriate for the construction of a Lagrangian numerical method.

5.1.3. Smoothing kernel function

The smoothing kernel function can be considered as equivalent to discretization schemes in mesh dependent techniques such as finite difference, for example. Properties as accuracy, stability and the simulation costs of an SPH simulation heavily depend on the smoothing kernel chosen and its associated smoothing length.[24]

It can be represented in a general form as

$$W\left(\mathbf{r}_{ij}, h\right) = \frac{1}{h^d} f\left(\frac{\mathbf{r}_{ij}}{h}\right) \tag{5.21}$$

where h denotes the smoothing or support length, which represents the spatial resolution of SPH. $\mathbf{r}_{ij}$ is the magnitude of the distance between particle i and j and d the dimension of the problem. One can find a wide variety of different kernel functions which satisfy the conditions listed in 5.1.1.1.

5.1.4. Convergence criterion

The SPH method involves two spatial discretization parameters. As all numerical methods, it uses a discretization of the computational space characterized by a certain length scale Δx, which is an average distance between particles. But the SPH method also involves a second parameter - the size of the field interpolation - which is proportional to the smoothing length h. The latter parameter controls the average number of neighbouring points used in the interpolation scheme. Like any numerical method, the SPH method is called consistent if the discrete solution obtained after resolution of discrete equations describing the flow tends to the exact solution when the sample size Δx tends to zero. At the same time the Equ.(5.2) approaches the exact solution if the kernel function is a proper approximation of the Dirac function as h tends to zero. The last criterion implies an infinite number of particles to obtain the exact solution.

The convergence of the SPH method is ensured if the following three relations are simultaneously satisfied:

$$\begin{cases} \Delta x & \longrightarrow 0 \\ h & \longrightarrow 0 \\ \frac{h}{\Delta x} & \longrightarrow \infty \end{cases} \tag{5.22}$$

For reasons of application and computational costs, it is evident that the ratios for $\frac{h}{\Delta x}$ must be finite. For the simulations run in ASPHODEL an aspect ratio of 1.2 was chosen.

5.2. Solving the Euler Equations with the Standard SPH Method

The mathematical tools presented can be used to numerically solve the system of equations (5.25). If we assume to have a set of calculation points x_i achieving a satisfactory discretization of the investigated fluid, each point has its own velocity v, density ρ and pressure p. Further, each point is assigned an elementary volume ω - also called weight. The standard numerical SPH method involves the calculation of the spatial terms to transform the partial differential equations (PDE) into ordinary differential equations (ODE) and a time integration of the obtained ODE.

5.2.1. Euler Equations

For this application, the governing equations are composed of the conservation of mass and momentum, while neglecting the conservation of energy.

If we neglect the viscous terms in the Navier-Stokes equations, thus we obtain the system of Euler equations for a isothermal flow. This system can be written in non-conservative form as:

$$\frac{\partial \rho}{\partial t} + [\mathbf{v} \cdot \nabla]\rho = -\rho \nabla \cdot \mathbf{v} \tag{5.23}$$

$$\frac{\partial \mathbf{v}}{\partial t} + [\mathbf{v} \cdot \nabla]\mathbf{v} = -\frac{1}{\rho}\nabla p + f_e \tag{5.24}$$

These equations are written for a fixed reference and therefore represent an Eulerian description of the flow. In the context of a Lagrangian description, which will be used in the following, the reference is related to the flow and the system is rewritten:

$$\begin{cases} \dfrac{D\rho}{Dt} = -\rho \nabla \cdot \mathbf{v} \\ \dfrac{D\mathbf{v}}{Dt} = -\dfrac{1}{\rho}\nabla p + f_e \end{cases} \tag{5.25}$$

where $\frac{D}{Dt}$ is the total derivative with respect to time also known as the Lagrangian derivative. This system of equations will be the basis for the construction of the SPH numerical method which was initially conducted for the simulation of free surface flows.

There are several approaches to the formulation of the conservation equations for the SPH method. The formulation used in ASPHODEL was developed by VILA [28] and COLAGROSSI [3]. The reason why the developers of this code chose this formulation is the suitability for multiphase flows showed by OGER [17], which was thoroughly investigated in ASPHODEL by LEDUC [11].

The obtained system of discrete equations is:

$$\begin{cases} \dfrac{D\rho_i}{Dt} = \rho_i \sum\limits_{j \in D_i} \dfrac{m_j}{\rho_j}(v_i - v_j)\nabla W_{ij} \\ \dfrac{D\boldsymbol{v}}{Dt} = -\sum\limits_{j \in D_i} m_j \left(\dfrac{p_i + p_j}{\rho_i \rho_j}\right) \nabla W_{ij} + f_e \end{cases} \tag{5.26}$$

To close the system of equations there is a need for a correlation in order to calculate the pressure p_i. The Tait equation (Equ.(5.27)) is typically used in SPH to simulate the behaviour of water. This equation of state implies that the pressure p_i is a function of the density ρ_i.

$$p_i = \frac{\rho_0 c_0^2}{\gamma} \left[\left(\frac{\rho}{\rho_0} \right)^{\gamma} - 1 \right] \tag{5.27}$$

The variables with the index *0* represent the state of reference, with ρ_0 and p_0 as the reference density and pressure for water. The parameter γ represents the adiabatic exponent, which is defined for liquid water with the value 7. In the case of a hydraulic pump we consider the fluid as incompressible, but the calculation of the pressure using the Tait equation implies a compressibility of the fluid, which is directly related to the reference speed of sound. Despite that fact, this law is able to describe incompressible fluids in an accurate manner as long as we consider the actual speed of sound of the investigated fluid, which is defined for water with 1484 m/s. This value is directly associated with an increase of the simulation costs since the time integration uses a time step, which is limited by the reference speed of sound c_0. This makes it necessary to verify the necessity of the physical speed of sound for our application. Marongiu states, that considering hydraulic flows with Mach numbers below 0.1 in the entire system, leads to a variation of the density lower than 1%. The reference speed of sound is therefore chosen with 10 times the maximum speed of the flow. This simplification is acceptable for the development of the code, while it must be noted that the simulation costs will significantly increase for the application on an actual pump design.[12],[14]

6. Calculations with the SPH code ASPHODEL

This section focusses on the methodology and formalism applied in ASPHODEL, which is based on the thesis of the initial developer J.C. MARONGIU, who accurately described the applied formalisms of the SPH-ALE developments.

The hybrid ALE formalism has been originally developed by Jean-Paul VILA in the 90s ([20],[28],[29]) and is based on conservative formulation of the conservation laws, referring to a moving control volume with velocity v_0. The velocity of the considered control volume can be chosen *arbitrarily*. In the case of defining the velocity $v_0 = 0$ leads to the Eulerian description, whereas setting the velocity equal to the flow speed, i.e. $v_0 = v$, results in the Lagrangian description. This allows the treatment of boundary conditions with already proven methods developed for Eulerian descriptions.

The standard SPH method is built on a non-conservative form of the Euler equations written in a Lagrangian frame, from which MARONGIU, LEBOEUF and PARKINSON initially developed ASPHODEL. This code is based on the *previous work from VILA, an Arbitrary Lagrange Euler (ALE) description together with a weak form of the Euler equations. This leads to a hybrid method directly linked to the finite volums methods* [15]. The developers chose this formulation originally for the application on Pelton turbines. The characteristic of this method was the ability to treat solid walls in order to provide a mathematically and physically more rigorous model, whereas being suitable for the treatment of complex geometries of Pelton turbines applied at ANDRITZ HYDRO Vevey.

The equations of motion are written in conservative form by conducting a flow balance on the periphery of the control volume and are expressed in a reference frame related to a mobile control volume. This leads to the following flow balance

$$\left.\frac{d}{dt}\right|_{v_0} \int_{\Omega} \Phi \, d\Omega + \int_{S} \Phi(\mathbf{v} - \mathbf{v}_0) \cdot \mathbf{n} \, dS = \int_{S} Q_S \cdot \mathbf{n} \, dS + \int_{\Omega} Q_V \, d\Omega \tag{6.1}$$

where Φ is the vector containing the conservative variables, v_0 the velocity of the control volume in motion, S denotes the boundary of the control volume Ω, $\boldsymbol{n}$ the unit normal vector perpendicular to the surface and Q_S and Q_V represent the surface and volume source terms, respectively. $\left.\frac{d}{dt}\right|_{\boldsymbol{v}_0}$ denotes the derivative along the trajectory followed by the control volume. When transforming the surface terms into volume integrals by means of the Gauss' theorem and assuming that the source term is reduced to the surface pressure, we obtain a conservative form of the system of conservation laws that can be put in the form:

$$L_{\boldsymbol{v}_0}(\Phi) + div(\mathbf{F}_E(\Phi) - \boldsymbol{v}_0 \, \Phi) = Q_V \tag{6.2}$$

where $L_{\boldsymbol{v}_0}(\Phi)$ is the transport operator associated to the field of transport $\boldsymbol{v}_0$, and $\boldsymbol{F}_E$ denotes the vector of flux associated to the Euler equations (Equ.(6.4)). In three dimensions these flows are given by:

$$\boldsymbol{v} = \begin{pmatrix} u \\ v \\ w \end{pmatrix}, \quad \Phi = \begin{pmatrix} \rho \\ \rho u \\ \rho v \\ \rho w \end{pmatrix} \tag{6.3}$$

$$F_E^{(1)}(\Phi) = \begin{pmatrix} \rho u \\ p + \rho u^2 \\ \rho uv \\ \rho uw \end{pmatrix}, \quad F_E^{(2)}(\Phi) = \begin{pmatrix} \rho v \\ \rho uv \\ p + \rho v^2 \\ \rho vw \end{pmatrix}, \quad F_E^{(3)}(\Phi) = \begin{pmatrix} \rho w \\ \rho uw \\ \rho vw \\ p + \rho w^2 \end{pmatrix} \tag{6.4}$$

With this formulation it is possible to describe the flow regardless of the perspective of the coordinate system, where $\boldsymbol{v}_0\Phi$ describes the movement of the control volume. This implicates the possibility to define $\boldsymbol{v}_0 = \boldsymbol{v}$, where the flux terms disappear and we obtain the Lagrangian description, or $\boldsymbol{v}_0 = 0$ leading to the Eulerian description.

MARONGIU found that the calculation of the interaction between the particles, regarding the discrete equations of motion formulated by VILA (see Equ.(5.26)), involve only the gradient of the kernel function, hence ∇W. The calculation of the gradient of a function previously stated in Equ.(5.11) is hence,

$$\langle \nabla f(x) \rangle = \int_{\partial\Omega} f(x')\, W(x - x', h)\mathbf{n}\, dS - \int_{\Omega} f(x')\, \nabla W(x - x', h)\, dx' \tag{6.5}$$

If the particles close to the border are considered, it can be noticed that the field of interpolation intersects with the boundary $\partial\Omega$, thus the kernel function W is not null at $\partial\Omega$. The surface integral is only zero when regarding special cases where the boundary conditions are actually zero, which typically occurs in the case of a free surface flow.

In the case of a non-adherent solid wall, neither pressure nor velocity are initially set to zero, which is why this term can not be neglected, as done in the Standard SPH formalism. The omission of this term is the reason for the non-consistency of the numerical scheme, so that there are attempts to treat the solid walls by means of virtual particles.

The approach adopted by MARONGIU calculates the surface integral directly. The approximation of the gradient of the function f was modified to

$$\langle \nabla f \rangle_i = \sum_{j \in D_i} f_j \nabla W_{ij}\, \omega_j + \sum_{j \in \partial D_i} f_j W_{ij} S_j \mathbf{n}_j \qquad \text{with } W_{ij} = W(x_i - x_j, h) \tag{6.6}$$

and S_j defines the area of the surface element associated to the discretization point j on the solid wall. MARONGIU states that *"with this new approximation it is now possible to keep the same precision at the boundary, as in the core of the computational domain, since the same quadrature formula is used."*[1]

1. translation from MARONGIU: *"Cette nouvelle approximation permet de restaurer la consistance du schéma numérique et présente à priori la même precision au bord qu'au coeur du domaine de calcul puisque la même formule de quadrature est utilisée."*

As mentioned this part of the theory refers to the thesis of the developer [14], which applied the ALE formalism developed by VILA [ref] for complex geometries. This has been successfully applied for the simulation of Pelton buckets and further developments at ANDRITZ HYDRO Vevey concerning the parallelization of the code now enable now the simulation of entire turbines in a remarkable time.

A main difficulty of the SPH method, which still requires development and innovation, is the adequate modelling of boundary conditions due to the truncation of the field of interpolation. This leads to significant errors in the evaluation of the field and its gradients in areas near the boundaries. In order to solve this problem, different methods have been developed, as the application of a virtual extension of the computational domain beyond the adjacent walls. This allows to find a suitable number of neighbouring particles in the interpolation scheme and restore the consistency of the numerical scheme. However, these methods are not satisfactory for the application on complex geometries.

Further analysis of applications on violent phenomena such as the impact of a water jet on a wall were conducted, which comprise the risk of an inadequate representation of the flow interaction with the solid wall. The correct representation of the flow interaction with solid walls has been extensively investigated. Further developments are being carried out at this stage by Magdalena NEUHAUSER at ANDRITZ HYDRO Vevey with the objective to combine SPH with the Finite Volume Method. This is possible due to the ability of the ALE formulation to change between a Lagrangian and Eulerian description, where the conservation laws are written in an arbitrarily moving frame of reference.

The discrete equations describing this ALE method are finally given by [15],[28]:

$$\begin{cases} \dfrac{d}{dt}\left(\mathbf{x}_i\right) = v_0\left(x_i, t\right) \\ \dfrac{d}{dt}\left(\omega_i\right) = \omega_i \sum\limits_{j \in D_i} \omega_j \left(v_0\left(x_j\right) - v_0\left(x_i\right)\right) \nabla W_{ij} \\ \dfrac{d}{dt}\left(\omega_i \rho_i\right) + \omega_i \sum\limits_{j \in D_i} \omega_j 2 \rho_{E,ij} \left(v_{E,ij} - v_0\left(x_{ij}, t\right)\right) \cdot \nabla W_{ij} = 0 \\ \dfrac{d}{dt}\left(\omega_i \rho_i \boldsymbol{v}_i\right) + \omega_i \sum\limits_{j \in D_i} \omega_j 2 \left[\rho_{E,ij} v_{E,ij} \otimes \left(v_{E,ij} - v_0\left(x_{ij}, t\right)\right) + p_{E,ij}\right] \nabla W_{ij} = \omega_i \rho_i g \end{cases} \tag{6.7}$$

Providing a velocity for the calculated points different from the flow speed allows to treat a delayed speed throughout the convective flow. The mathematical description of the ALE method is generally conservative, so that the mass and momentum remain constant within the flow. However, if the velocity of the moving calculation points was considered to be in a pure Lagrangian description, thus $\boldsymbol{v}_0 = \boldsymbol{v}$, the convective flows are no longer zero. This implicates an exchange of matter, where $m_i = \omega_i \rho_i$ is no longer constant in time, unlike in the classical SPH method.

The developers of this method seek for an approach with the widely used Finite Volume Method. The ALE method allows to employ techniques developed for mesh-based Eulerian methods, which have been successfully elaborated in the last decades on complex flow conditions.

6.1. Generated 2D geometries for test cases

As already mentioned, the first task was the further development of the code by imposing inlet and outlet boundary conditions. This took place in cooperation with the developers of this code in the R&D department Vevey. So far this code was exclusively applied for free surface flows, as found in Pelton turbines. The implementation of boundary conditions is currently in the process of development. Many proposals circulate in the SPH community, however, no method has so far come forward as the most suitable one. These studies are in progress at present and will be able to deliver in the near future a more detailed analysis of these development steps. In the course of this work, we finally came to a stage where the specification of boundary conditions was possible, but this requires much more detailed evaluation to confirm the applicability. The last weeks of my stay in Vevey were dedicated to the integration of the three-dimensional pump geometry. In the following these processes are documented.

6.1.1. Cylinder and square geometry

First simulations were conducted on geometries created in `C++` containing a cylinder or a square (Fig.6.1). The geometry consists of particles arranged at the circumference of the cylinder, with a specific particle diameter. A prerequisite for the correct application of this method is, that the distance between the center-points of the solid particles has to be smaller than the fluid particle size. Further, each solid particle is assigned by a unit normal vector. Together this represents the surface of the geometry.

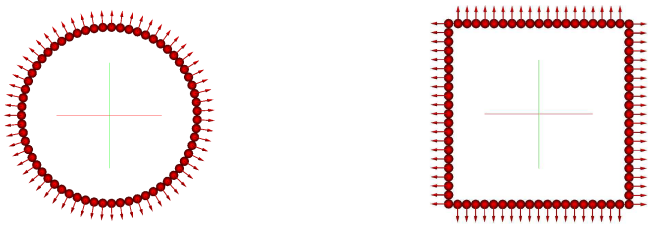

Figure 6.1.: Geometry created in C++ including normals

6.1.2. Subdivision in moving and static domain in ALE mode

This section describes the creation of two-dimensional geometries in order to attempt to simulate a rotor-stator-interaction with SPH. The calculation domain was modified, in order to separate the moving from the static calculation points. Since the focus is more on the development and evolution of the code, a simple square geometry is used at the beginning in order assess the feasibility of the intended test-case. A schematic sketch is shown in Figure 6.2. The code was changed in a manner, which allows to specify an arbitrary particle velocity in z-direction, which does not depend on the flow speed and also may be non-zero. Further,

an acceleration phase according to Equ.(6.8) was included to stabilize the initial phase of the simulation, by means of avoiding an abrupt movement of the particles.

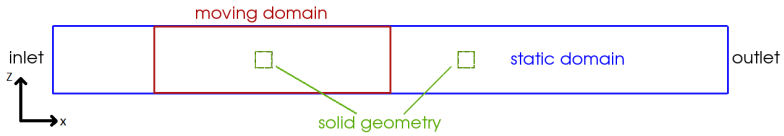

Figure 6.2.: Subdivided domain for Eulerian calculations.

$$\begin{cases} v_z = \frac{v_{z,end}}{2} \cdot \left[1 + sin\left(\left(\frac{t}{t_1} - \frac{1}{2}\right) \cdot \pi\right)\right] & t \leq t_1 \\ v_z = v_{z,end} & t > t_1 \end{cases} \tag{6.8}$$

with:
v_z ... current speed
$v_{z,end}$ ... maximum speed
t ... physical time
t_1 ... acceleration time

6.1.3. NACA Airfoil

For further evaluation of the code, it was decided to generate a geometry based on the NACA airfoils developed by EASTMAN et.al. [1933]. A cambered geometry was created by adapting a script written by J.C. Marongiu on `C++` for a symmetric 4-digit profile. In the following, the equations and parameters for the geometry are briefly described.

Symmetric Airfoil

$$y_t = \frac{t}{0.2} \cdot c \cdot \left[0.2969\sqrt{\frac{x}{c}} - 0.1260 \cdot \left(\frac{x}{c}\right) - 0.3516 \cdot \left(\frac{x}{c}\right)^2 + 0.2843 \cdot \left(\frac{x}{c}\right)^3 - 0.1015 \cdot \left(\frac{x}{c}\right)^4\right] \tag{6.9}$$

with:
c ... chord length
x ... position along the chord from 0 to c
y_t ... half thickness at a given value of x
t ... maximum thickness as a fraction of the chord

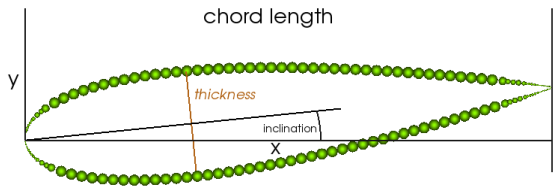

Figure 6.3.: symmetric NACA geometry generated in C^{++}.

Cambered Airfoil

For the generation of a cambered foil equation (Equ.6.9) is extended by the following equation to create the camber.

$$\begin{aligned} 0 \leq x \leq p \cdot c \qquad & y_c = m \cdot \frac{x}{p^2} \cdot \left(2p - \frac{x}{c}\right) \\ p \cdot c \leq x \leq c \qquad & y_c = m \cdot \frac{c-x}{(1-p)^2} \cdot \left(1 + \frac{x}{c} - 2p\right) \end{aligned} \tag{6.10}$$

with:
y_c ... mean camber line at a given value of x
m ... maximum camber
p ... location of the maximum camber

Thus, the coordinates arise from:

$$\begin{aligned} \textbf{upper camber} \qquad & x_U = x - y_t \cdot sin\phi \quad ; \quad y_U = y_c + y_t \cdot cos\phi \\ \textbf{lower camber} \qquad & x_L = x + y_t \cdot sin\phi \quad ; \quad y_L = y_c - y_t \cdot cos\phi \\ & \text{with} \quad \phi = arctan\left(\frac{\mathrm{d}y_c}{\mathrm{d}x}\right) \end{aligned} \tag{6.11}$$

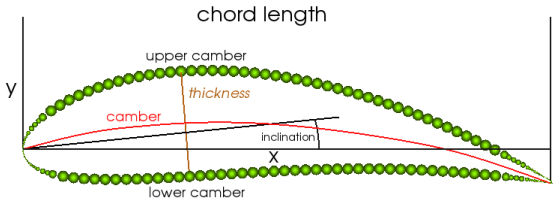

Figure 6.4.: Cambered NACA geometry generated in C++.

6.2. Boundary condition developments

This section summarizes the performed developments on ASPHODEL which were carried out on different geometries during a three-month internship at ANDRITZ HYDRO Vevey. The results are the basis for comparisons with existing experimental data and the previously mentioned finite volume calculations, in order to present the applicability of this code. In the beginning, investigations on 2D geometries as cylindrical and square shapes were carried out, which subsequently led to more complex geometries as airfoils and three-dimensional geometries. It should be noted that my task was the preparation and analysis of the numerical simulations run on ASPHODEL, while Magdalena NEUHAUSER and J.C. MARONGIU conducted the modifications in the code. The results of 2D simulations are not shown in this work, because more detailed examinations are required and the main focus of this report was laid on the applicability for a centrifugal pump.

During the development process, two different fluid motion types were conducted - the Lagrangian and Eulerian description for the simulations - which at the same time demonstrate the flexibility of ASPHODEL. The first type used was the Lagrangian description, where the velocity of the particles is set equal to the fluid velocity, which enables tracking of each particle throughout the domain.

$$\frac{dx_i}{dt} = v_i \tag{6.12}$$

The motion type has been changed in the course of the work to Eulerian due to reasons, which will be explained in section 6.2.2. Therefore, the calculation points in the discretized domain are spatially fixed with a velocity of null.

$$\frac{dx_i}{dt} = 0 \tag{6.13}$$

The first step was the adaptation of ASPHODEL for internal flows, enabling inlet and outlet conditions at the boundaries. Since the parallel mode of the code was initially developed for 3D simulations, the 2D calculations had to be executed on one core, either on the local host or on the cluster. Thereby, converged solutions were generated after an average computational time of 10 to 30 hours. The simulations were partly run simultaneously.

Even though adaptations of the method had to be carried out continuously, some basic settings for the execution of the software are stated. These settings have no claim for general applicability of the conducted simulations, but can be seen as a reference.

ASPHODEL INI-File Settings

The following description shows the structure of an initial file, which in addition to the mentioned parameters requires information about the output configuration as well as the fluid and solid geometries.

```
Fluid parameters
        gamma = 7
        reference density = 1000.
```

```
        reference speed of sound = 10x fluid velocity

Case parameters
        gravity
        CFL

Numerical parameters
        length ratio = 1.2              ...parameter for the kernel
                                           function
        r0 = 0.002                      ...particle radius
        time integration scheme = RK3
```

The parameter γ represents the heat capacity ratio of water; the reference density and speed of sound are used in the Tait equation (Equ.(6.15)). Since the code is determined by the Euler equations, the fluid viscosity is not considered.

6.2.1. Lagrangian motion description

The first simulations were conducted with a cylinder geometry, while setting the motion type on Lagrangian mode. In the following, some observations and findings from the results will be commented, in order to describe the complexity of the evaluation, since experiences are very limited in this field.

It is obvious that some influential parameters can be determined, as the fluid particle size, which is a measure for the discretization of the investigated domain, as well as the Courant-Friedrichs-Levy condition, which is a stability limit for solving partial differential equations numerically.

$$\mathrm{CFL} = \frac{v \triangle t}{\triangle x} \tag{6.14}$$

A CFL-number of 0.5 resulted in an acceptable ratio between stability and simulation costs. Further, the MUSCL scheme was chosen which is known to provide accurate results in solutions also affected by shocks and discontinuities as well as the Riemann Solver.

MUSCL is a method used to avoid spurious oscillations and obtains a high-order accuracy by data reconstruction. This acronym stands for Monotone Upstream-centred Scheme for Conservation Laws by Van Leer (1979) and is used for the generation of second-order upwind schemes through variable extrapolation.[25]

The fluid particle size is a parameter which has been varied several times. As stated earlier in this section it should be noted, that the fluid particle size should not be smaller than the solid particle size, because of the inevitable penetration of the fluid particles due to spatial gaps. Nonetheless, dimensioning the wall particles too small leads to non-physical outcomes in areas, where solid particles are not influenced by any fluid in the domain. Results showed at an early stage that some modifications were necessary to obtain exploitable results, since one of the main issues in Lagrangian mode is the correct reproduction of the flow around

a bluff body (Fig.6.5). An increase of the reference speed of sound showed no significant improvements, but an increase in computational costs. The code includes up to this point a numerical viscosity in the momentum equation to stabilize the scheme, but no viscous terms.

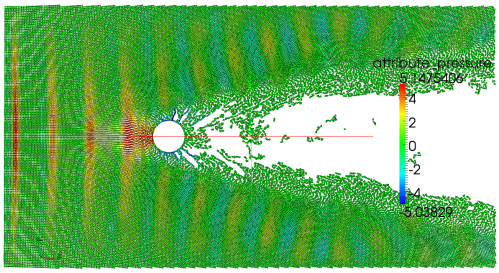

Figure 6.5.: Pressure distribution in Lagrangian mode.

a) Inlet boundary condition

A first step was, to eliminate the inlet particles. The second step was to replace the MUSCL scheme by constant reconstruction throughout a specified length at inlet. Constant reconstruction was conducted in order to improve the boundary conditions, which were affected by reflected waves at inlet. Constant reconstruction has the characteristic of being very diffusive, therefore, it was only applied at the inlet to reduce these reflected waves at the boundaries. This change was only of limited benefit since the reproduction of the pressure field was not satisfactory, due to the damping effects along the fluid domain, e.g. suppressing flow effects as Kármán vortex shedding.

b) Background pressure

A background pressure was introduced with the attempt to improve the numerical stability and to decrease the pressure waves generated at the boundaries of the domain. For this, the Tait equation has been assigned with a constant pressure, and numerous simulations were carried out to verify the impact.

$$p = \frac{\rho_0 c_0^2}{\gamma}\left[\left(\frac{\rho}{\rho_0}\right)^{\gamma} - 1\right] + p_{ref} \tag{6.15}$$

Expectations of high improvements concerning the pressure waves were limited, but this attempt was used as start-up for further modifications, since the implementation was straightforward. The results showed an increase in the stability of the simulation.

c) Inlet and outlet condition based on fictive forces

As a further step, it was decided to introduce a fictive force at the outlet of the considered domain, in order to overcome the pressure inconsistencies at low Mach numbers. Therefore a buffer was implemented, in which the pressure and the buffer size can be set to a defined value. This leads to a deceleration of the particles entering the buffer and in consequence,

the area behind the bluff body is subsequently filled up with fluid particles until $p_{[i]} \geq p_{ref}$ is reached. A force is introduced both at inlet and outlet, to improve the boundary conditions of the fluid domain. The force at the inlet is based on the velocity (Equ.(6.16)), and the force at outlet on the pressure (see Equ.(6.17)). These forces are added to the momentum equation if the particle is located either in the inlet buffer zone or in the outlet buffer zone (Fig.6.6).

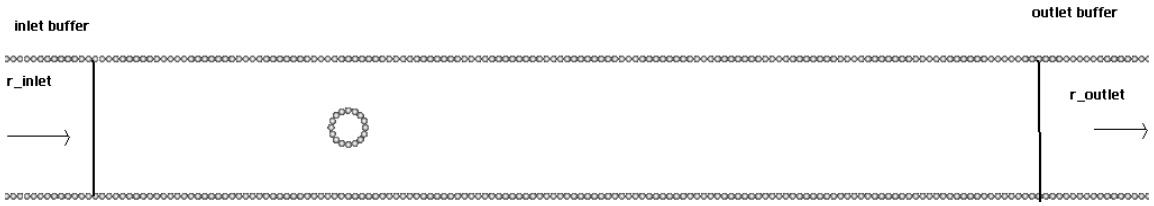

Figure 6.6.: In- and outlet buffer zone.

Buffer zone at inlet
The inlet force was based on the fluid velocity:

$$f_{inlet} = \frac{(v_i - v_{ref})^2}{2 \cdot g} \mathbf{n}_{inlet} \tag{6.16}$$

ρ_i ... fluid density
v_{ref} ... reference velocity
$\mathbf{n}_{inlet}$ ... unit normal of inlet boundary

Buffer zone at outlet
The outlet force was based on the pressure:

$$f_{outlet} = \begin{cases} 0 & \text{if } p_i \geq p_{ref} \\ \dfrac{p_i - p_{ref}}{\rho_i \, g} \mathbf{n}_{outlet} & \text{if } p_i < p_{ref} \end{cases} \tag{6.17}$$

p_{ref} ... reference pressure
$\mathbf{n}_{outlet}$ ... unit normal of outlet boundary

These modifications led to the intended filling of the domain, but led to inconsistencies in handling the particles. For example, a reflection was generated by the outlet condition, which generated a vortex in the opposite direction of the flow (Fig.6.7). The particles exit the domain at the outlet, as well as through the solid walls, starting when the domain is entirely filled with particles.

Several simulations were conducted to verify the influence of the force at the outlet boundary. These modifications filled the domain as intended with particles, but led to violent fluctuations at the outlet and inappropriate calculations of variables. Further investigations concerning the discretization (fluid particle -) size are still being conducted.

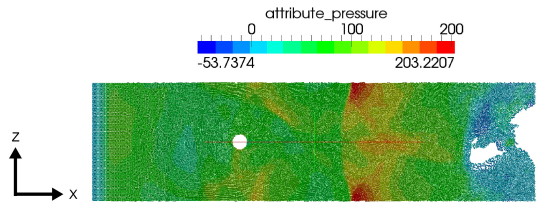

Figure 6.7.: Execution in Lagrangian mode.

6.2.2. Eulerian motion description

For reasons of inappropriate reproduction of the flow in Lagrangian mode, due to boundary reflections and penetrating fluid particles through wall boundaries, it was decided to shift to the Eulerian mode, by setting the velocity of the calculation points to zero.

Therefore the creation of the geometry had to be modified, in order to generate the fluid domain, which yielded a solid and fluid VTK-FILE. In case of curved geometries and fluid particles based on a Cartesian pattern, unequal distances occur between the solid and the nearest fluid particles. In order to reduce the discretization error around the solid, an algorithm proposed by Bouscasse et. al. [Particle initialization through a novel packing algorithm, 6th SPHERIC workshop, 2011] was applied by J.C. Marongiu as an extended package of the code (Fig.6.8). This algorithm is based on the use of Van der Waals like forces to place particles throughout the fluid domain. These developments for 2D applications are equally applicable for 3D geometries without modifications.

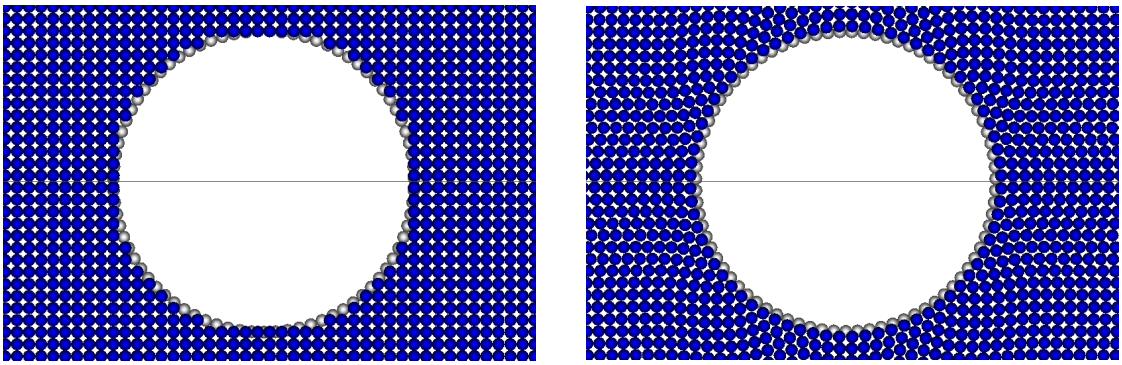

Figure 6.8.: Fluid domain correction using the Bouscasse algorithm. left: without Bouscasse algorithm, right: using Bouscasse

During the course of this procedure, some simulations were conducted simultaneously on straightforward geometries, such as squares and rectangles in order to move forward with the development of the boundary conditions.

Further modifications were applied on the Riemann Solver and on non-reflecting conditions at inlet. A tangential velocity component was implemented into the 1D Riemann Solver, to reduce the flux error at the outlet. Additionally to the non-reflecting conditions proposed

by Ghidaglia and Pascal [2004], and the adaptations on ASPHODEL by Marongiu and Neuhauser, a fluid particle correction was conducted.

Until this correction the gradient of the kernel function was symmetric, hence

$$\nabla W_{ij} = -\nabla W_{ji} \tag{6.18}$$

Due to the correction developed by Magdalena NEUHAUSER the symmetry condition could not be fulfilled any longer (Equ.6.19). This correction is based on the sum of the weights and the kernel function, hence $\omega_j \nabla W_{ij}$ which enforces Equ.(**??**) to be null.

$$\nabla W_{ij} \neq -\nabla W_{ji} \tag{6.19}$$

These developments and their influences are part of the thesis of the developer, which is why the background and the formulation of these findings are not stated. It should be briefly mentioned that the modifications led to improvements in the simulation of the flow conditions. Similarly to the cylinder simulations, calculations on a square geometry were conducted. At the beginning the calculations were performed in Lagrangian form, which finally led to the Euler description. Figure 6.9 shows the difficulties that are encountered, caused by reflective boundary conditions in Lagrangian mode. In order to reduce the error due to reflections at the boundaries, symmetry conditions were set in vertical direction.

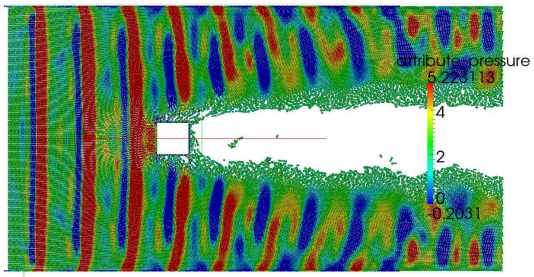

96.000 timesteps

Figure 6.9.: Pressure distribution in Lagrangian mode.

As stated before, it was decided to switch to Eulerian mode. It was evident that a simple square geometry would be convenient for this type of simulation, since the required solid and fluid geometry was straightforward. Figure 6.10 shows the generated domain including the square geometry (left) and the solid particles with their respective normals (right). For the representation of the square walls in the flow it was decided to create horizontal normals at the square corners.

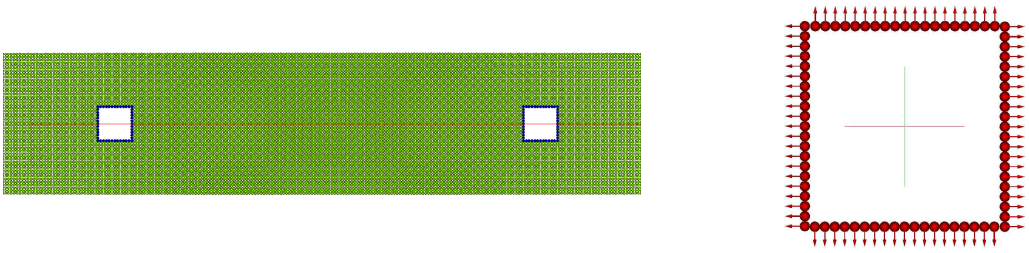

Figure 6.10.: left: fluid and solid domain; right: square geometry including normals

a) NACA airfoil interaction

For the simulations of the NACA geometries with Eulerian description we re-applied the Bouscasse algorithm (see 6.2.2) on the fluid domain to reduce the discretization error around the geometry.

Figure 6.11 shows the subdivision of the investigated domain for the Eulerian simulation. The two exterior areas of the domain are kept static (without calculation point movement), whereas the area in between is exposed to a motion in vertical direction, which allows to verify the possibility of subdividing the domain in zones of different speeds.

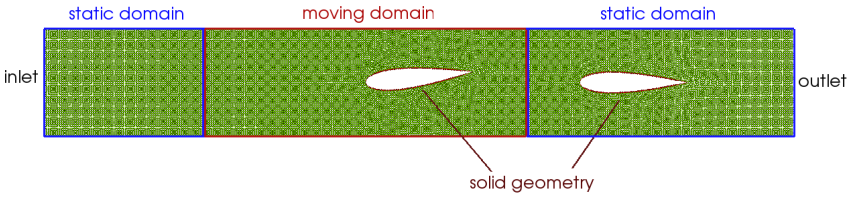

Figure 6.11.: Investigated domain with two NACA airfoils.

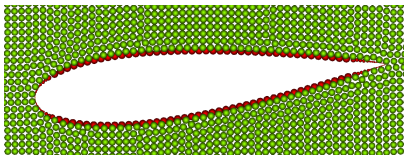

Figure 6.12.: Fluid domain around airfoil after application of algorithm of Bouscasse.

The procedure for the NACA airfoils was conducted in a similar manner as for the previously discussed geometries. These simulations were occasionally conducted simultaneously, in order to examine the effects of different modifications.

To prevent surge and interference in the fluid domain an acceleration phase for the moving geometry was implemented (see 6.1.2). From here on some simulations were launched with different velocities up to $v_z = 0.5[m/s]$ (V16), which enabled identification of interactions between the leading edge and the inlet boundary.

To investigate the influence of the discretization of the fluid domain, four simulations were conducted with a particle diameter d_p of 0.002, 0.001, 0.0005 and 0.00025 [m]. The analysis of the boundaries did not show significant improvements, but due to the execution of the 2D simulations on one node we can determine that a decrease of the particle size by half, results in an increase of the computational cost by a factor of 4.5 to 6. Further, it was noticed that the wake depends strongly on the size of the particles.

Another comparison was made by varying the pressure p_{inf} imposed on the fluid particles. V14 (V... version) was carried out with a pressure $p_{inf} = 0$ and V21 with $p_{inf} = 100$ to examine the influence on the flow.Detailed analysis is being carried out at this stage, nonetheless, pressure fluctuations at the boundary conditions are still observed.

Next, simulations with multiple profiles were performed (V27), to observe the interactions between moving and static airfoils and the stability of the solver. The geometry with symmetric profiles was launched with an incidence angle of null for the moving profiles.

v_z	-1.0 [m/s]
p_∞	0 [Pa]
v_{jet}	5 [m/s]
acc. time	5 [s]

The results showed a good convergence behaviour of the code, where the simulation of a quasi rotor/stator interaction turned out to be stable after the acceleration phase. The findings from these tests should enable us on a later phase to run a pump simulation in a more stable manner, since a smoother flow formation can be expected because of the acceleration of the rotation of the impeller ($\omega = 0$ to max $\left[\frac{rad}{s}\right]$).

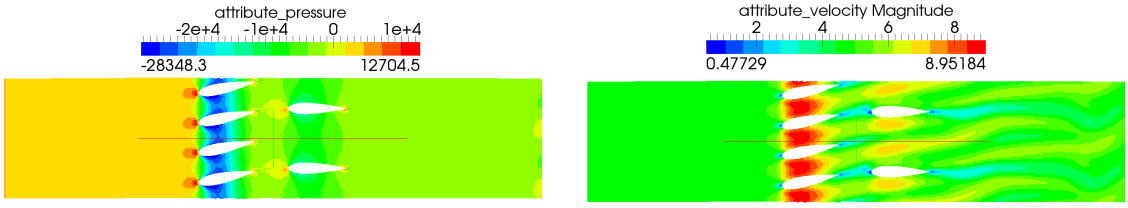

Figure 6.13.: Motion of 4 airfoils (V27); T=6.25[s].

It should be noted here, that these tests carried out in 2D were aimed as an approach for a simulation of the pump geometry. The focus was based on the verification of the performed work of the code, such as boundary conditions and fluid domain generation. The tests themselves are not really suitable for inviscid flow studies, but served to gather more experience with the code and showed the range of stability.

b) Verification of the boundary conditions (BC)

Boundary conditions are still one of the main issues that the SPH method is facing and where research is in progress. Initial boundary conditions were at the beginning of this work only under restrictive terms possible to impose at the boundaries. In case of Pelton turbines the only claim for the flow condition at inlet was the specification of a jet velocity. This could not be adopted for the application on a pump simulation, which represents a closed system. Therefore, some modifications were conducted by Magdalena NEUHAUSER, who has the task among others in her PhD thesis, to develop a method for the specification of adequate boundary conditions on the investigated system.

In order to verify the previously stated modifications in the code, an analysis of different boundary conditions at inlet and outlet of the symmetric airfoil test case (Fig.6.14) was performed. Furthermore, different verifications on the influence of the distance between the investigated geometry and the outlet boundary were conducted. This analysis had the objective to assess the influence of the boundary conditions on the flow.

Figure 6.14 shows the results obtained for a symmetric NACA 0020 airfoil (angle of attack = 0°), where different boundary conditions were imposed at the inlet and outlet, respectively. The test case was run with an array of 450×50 particles and the previously mentioned modifications. The uppermost result (V46) was conducted with the same inlet and outlet

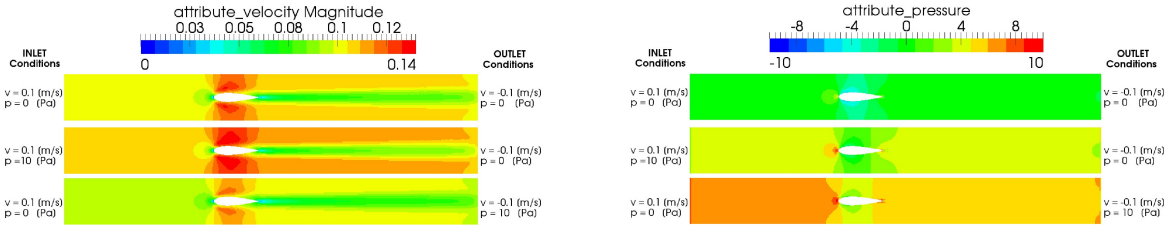

Figure 6.14.: Imposing different boundary conditions at inlet and outlet. left: velocity field; right: pressure field; from top to bottom: V46, V53, V54.

boundary condition on the flow. Therefore, a velocity of $0.1\left[\frac{m}{s}\right]$ is defined at both ends of the domain and a pressure of zero at outlet.

The boundary conditions of interest for numerical simulation are represented by the latter two results (V53 and V54). One can observe in V53, that the imposed pressure at inlet of the investigated domain influences the entire domain until the outlet, which in turn is not exposed to back pressure (for test purposes). Nevertheless, one can detect an influence at the outlet, which reveals the difficulties of correct implementation of boundary conditions. Further, imposing pressure at inlet causes an increase in velocity within the domain, until deceleration in the immediate vicinity of the outlet. Conversely, imposing outlet pressure results in deceleration of the velocity field, while causing an increase in pressure in the opposite direction of flow. This in turn corresponds to the anticipated effect of this pre-set. The quantitative evaluation of the boundary condition developments still requires further research, which is presently being conducted at the R&D department in Vevey.

6.3. Further test cases

In order to allow comparisons between ASPHODEL and other numerical codes, further test cases were created. In the following, they are briefly described and will allow the developers to validate the results.

6.3.1. Comparison with ISPH and a Finite Element Method

Investigations concerning a comparison between a SPH method and a finite element method were conducted by SHADLOO et al. in paper [24]. That work presents a numerical solution with ISPH for flow over a square and NACA airfoil. ASPHODEL uses a weakly compressible SPH formulation to solve the balance of the momentum equation, whereas the investigated ISPH method in that paper computes the pressure by means of solving a pressure Poisson equation. An advantage of the ISPH approach is the elimination of the speed of sound parameter in the time-step condition, which is necessary to determine the pressure term in the momentum equation by means of an artificial equation of state. Larger time-steps can be used in that approach, but under the restriction of higher computational costs due to solving the pressure Poisson equation at each time-step. The algorithm stability is satisfied by the CFL condition, which is defined by SHADLOO et al. with CFL = 0.125. A first order time-step scheme was used for time marching of the ISPH approach, which is an explicit time integration scheme. In that work the authors also describe a new type of solid boundary treatment called Multiple Boundary Tangents (MBT) and applied these recent developments on square and airfoil simulations in laminar flow.

That work illustrated that the method is able to capture complex physics of bluff-body flows as flow separation, wake formation at the trailing edge and vortex shedding. The results were validated with a finite element method, which showed good agreements.

As in our case of an initial particle domain, the writers pursued the same approach by removing the fluid particles within the solid body of the geometry. Nonetheless it should be noted, that these comparisons were performed in Lagrangian coordinate description, while ASPHODEL was tested in Eulerian mode, hence static calculation points throughout the domain.

Square

Although the examined code does not comprise physical friction - thus, viscous terms - the same initial conditions as those of that paper were taken. It is noted here that the SPH method is - according to the developers - commonly implemented with an artificial viscosity proposed by Monaghan. This is a major uncertainty in this code, which has not been elaborated in detail for ASPHODEL. The obtained results were intended as an initial assessment, and require much more intensive investigation. The flow was simulated for a range of Reynold numbers (100,200 and 300) according to the ISPH calculations, which are defined by the characteristic length l_c, density ρ, bulk flow velocity v_b and dynamic viscosity μ.

$$Re = \frac{\rho \cdot l_c \cdot v_b}{\mu} \tag{6.20}$$

This characteristic length is set equal to the edge length of the square obstacle and the chord length of the airfoil geometry, respectively. The simulation parameters were set by the authors with a fluid density $\rho = 1000[\frac{kg}{m^3}]$ and a dynamic viscosity $\mu = 1[\frac{kg}{m\,s}]$. The mass of each particle was set constant with a smoothing length for all particles equal to 1.6 times the initial spacing. The results were validated by the authors with results from a FEM based solver of a Comsol multiphysics software tool. The results were compared in terms of velocity contours and the pressure envelope for the airfoil.

Based on the test case with $Re = 100$, the inlet flow velocity v was calculated according to the initial values chosen in [24]:

Reynolds-Number: values from paper

$\rho = 1000\left[\frac{kg}{m^2}\right]$ ... fluid density

$Re = 100$ ... Reynolds number

$l_c = 0.7[m]$ ... side length of the obstacle

$\mu = 1\left[\frac{kg}{m\,s}\right]$ ... from paper

$$v = \frac{Re \cdot \mu}{\rho \cdot l_c} = \frac{100 \cdot 1}{1000 \cdot 0.7} = 0.1429[m/s] \tag{6.21}$$

Figure 6.15 shows the comparison of the results obtained with ASPHODEL and ISPH, concerning the velocity contours for two different Reynolds numbers, namely *Re = 100* and *200* for ISPH. The comparison of the results show a similar flow characteristic for both methods.

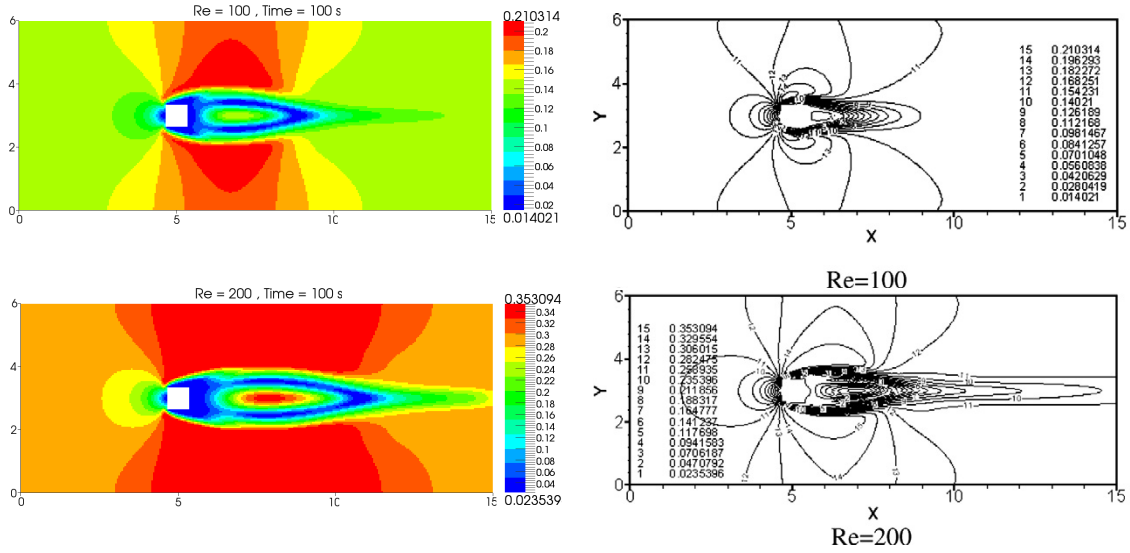

Figure 6.15.: Comparison of the obtained velocity contours with ASPHODEL (left) and ISPH (right) for Reynolds number in ISPH of 100 (top figures) and 200 (bottom figures) at T=100[s].[24]

One can observe in Fig.6.16 at a Reynold number of 300 the formation of vortex shedding at the rear section of the square obstacle. Shadloo et al. investigated this case and obtained satisfactory results, which were in good agreement regarding the magnitude of velocities as well as the position and the number of the vortices with the FEM results. Nevertheless, the authors noticed a slight discrepancy between both methods in terms of the separation point of the vortices from the rear edge of the bluff body.

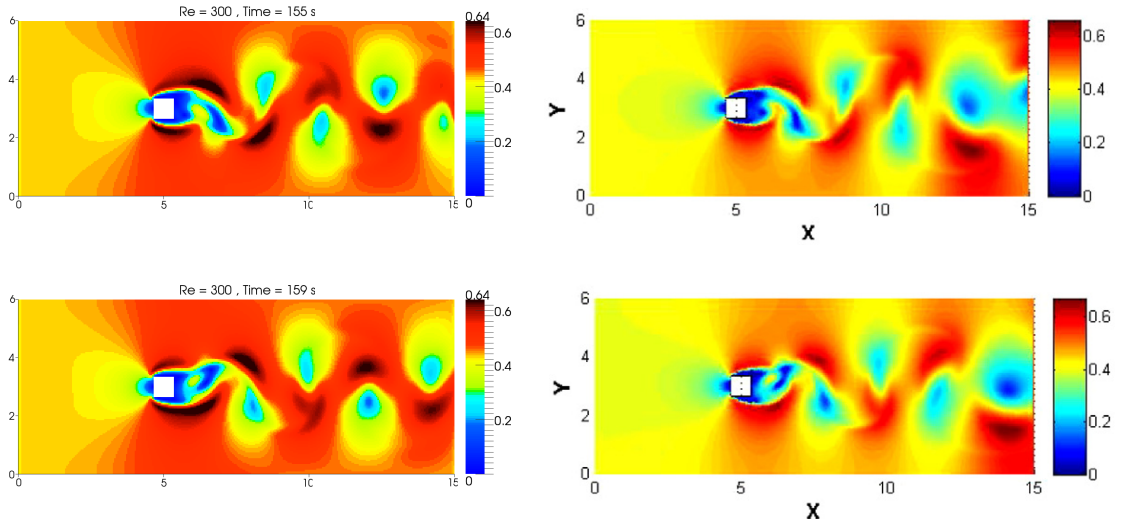

Figure 6.16.: Comparison of the obtained vortex shedding contours with ASPHODEL (left) and ISPH (right) for the case of vortex moving down (top figures) and up (bottom figures) for the Reynolds number of 300 in ISPH.[24]

Cambered NACA airfoil

A four-digit NACA 5515 airfoil series was defined, which denotes a maximum camber of 5% located 50% (chord length) from the leading edge with a maximum thickness of 15% of the chord (see 6.1.3).

The comparison of the flow was conducted on one hand for an angle of attack of 15° at a Reynolds number of 420 to reproduce a uniform flow around the airfoil, and on the other with an angle of attack of 10° and a Reynolds number of 1600. This leads to an initial flow velocity v of $0.21\left[\frac{m}{s}\right]$ and $0.8\left[\frac{m}{s}\right]$, where the characteristic length was set equal to the chord length. At this stage, these results are not comparable with the reference due to insufficient domain resolution.

Nonetheless, SHADLOO et al. note that there is a slight discrepancy in pressure for the upper side in the vicinity of the leading edge and the stagnation point, when comparing with the FEM results. This might be attributed to the dynamic nature of the used Lagrangian description in SPH, since the fluid particles are in continuous motion. A refinement of the discretization of the domain might lead to an improved reproduction of the features being studied, with the drawback of higher computational costs.

6.3.2. Moving square test case in Lagrangian mode

This test case was proposed by the scientific interest group SPHERIC to compare results from different SPH codes developed within the community. Several simulations were run, based on the SPHERIC test case **Test6** [1] and the thesis of CHERFILS [p. 129-156]. The case investigates the flow generated by moving a square within a Newtonian and incompressible viscous liquid in the absence of gravity. The computational domain is limited by a rectangular box (Fig. 6.17). The square initially static, undergoes a strong acceleration and reaches a stationary speed v_x until the end of the simulation.

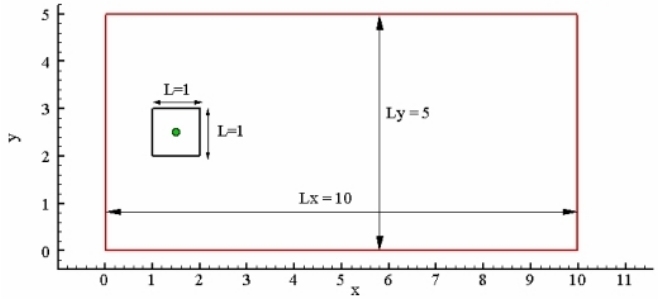

Figure 6.17.: SPHERIC Test Case 6: motion of a square (from left to right) in Lagrangian description.

6.3.3. Conclusions from these developments

All these comparisons provided a qualitative validation of the code, which affirmed the applicability of the code for complex geometries. Furthermore, these simulations should provide more insight into the influence of the artificial viscosity terms, which has not yet been thoroughly investigated. Further investigations are in progress. For our purposes at this stage, the validation of the results was kept rather short, due to the fact that the actual task was the application of a centrifugal pump on ASPHODEL.

1. A. COLAGROSSI; *Test6* , http://wiki.manchester.ac.uk/spheric/index.php/Test6, access 15.09.2011

6.4. Pump simulation with ASPHODEL

The following section describes the procedure for the preparation and creation of the pump geometry, as well as the associated initial fluid geometry. This process can be similarly applied to any geometry in any dimension. In our case, the generated geometry is used for the Eulerian description. However, it should be noted that this approach is also applicable for simulations in Lagrangian formulation, since the duration for the evolution of the flow throughout the pump can be significantly reduced by using an initial fluid domain. In order to make a direct comparison between the FV methods with the SPH method, the provided mesh geometry for this work was converted into a particle-based geometry. Here it shall be noted that this process is not suitable for future practical application in ASPHODEL. It should be avoided to generate the pump geometry based on a mesh.

6.4.1. Geometry generation procedure

This procedure was developed in the course of this work and requires further more detailed investigations. One goal might be to enhance the geometry converter with the generation of the fluid domain, so that the adaptation and optimization of the geometry could be considerably simplified. The figure on the right shows the sequence of the pump geometry generation for the execution in ASPHODEL. The different process steps are explained below.

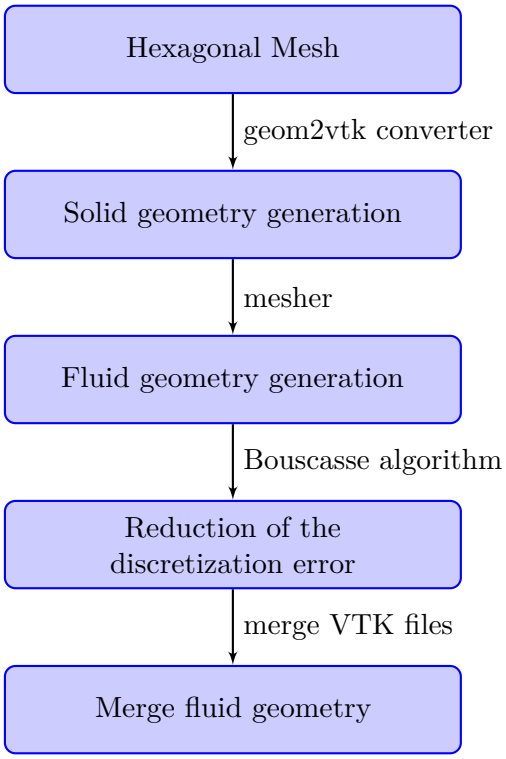

Figure 6.18.: Geometry generation procedure

6.4.2. Solid geometry generation

To generate the pump geometry for SPH from a finite-volume geometry, a converter was developed by Dr. Paul Pieringer for the R&D department. This converter transforms the hexagonal structure of the mesh geometry in a geometry, which is described by surface elements or 'two-dimensional particles', and their corresponding wall normal. Each mesh element is divided into particles, of which a maximum size is specified in advance. This maximum size is of great importance, since the maximum distance between wall particles must not exceed the defined fluid particle size, because otherwise particles would penetrate the examined area. This would cause an error in continuity and, ultimately, lead to instabilities. Furthermore, an additional criterion is defined, which is the maximum allowed angle of the mesh. By this means, a higher resolution of areas with strong mesh distortion is possible. This criterion has particular impact in areas of the rotor and stator blade edges. Thus the user needs an already existing solid mesh for the generation of the geometry and the specification of a maximum particle size at the wall. Based on these conditions, each mesh component is divided into particles, where particles which are in non-compliance with the requirements, are gradually subdivided, until the criterions are met. The execution of this converter requires a few seconds, and in the course of this work has proven itself in the application on different particle sizes of the pump geometry, as robust and reliable. Figure 6.19 shows the generated pump geometry for the application in SPH.

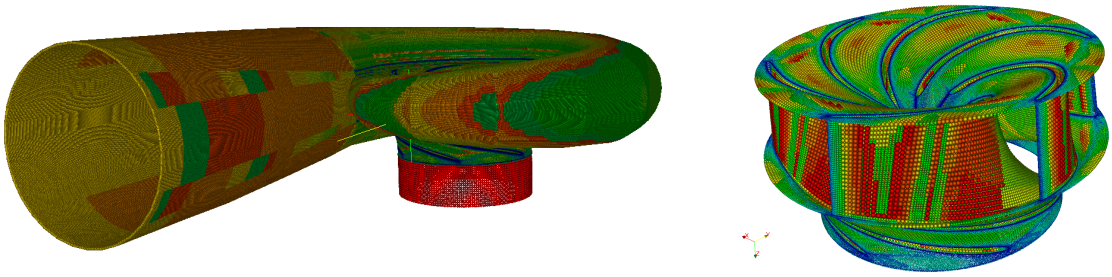

Figure 6.19.: Pump geometry in ASPHODEL.

6.4.3. Fluid geometry generation

The idea of a tool for generating the fluid geometry was developed in the course of this work in Vevey, when the decision was made to perform the simulations using the Eulerian description. As a result, an initial fluid domain had to be created. Therefore, a tool was used, which takes the particles and their respective normals into account. The fluid domain is consequently composed of particles generated in a Cartesian coordinate system, which encloses the entire pump. Under consideration of the direction of the wall normals, the externally situated particles are removed. During this process, the blade walls were found to be problematic, since not all particles in these regions were properly removed (<20 particles). A brief analysis pointed out that the accuracy of the data of the coordinates and normals of the solid geometry should be increased, as well as that an improved verification loop of

the wall normal criteria should be implemented. It was found that regions with normals perpendicularly situated to each other could lead to inappropriate results (see Fig.6.20).

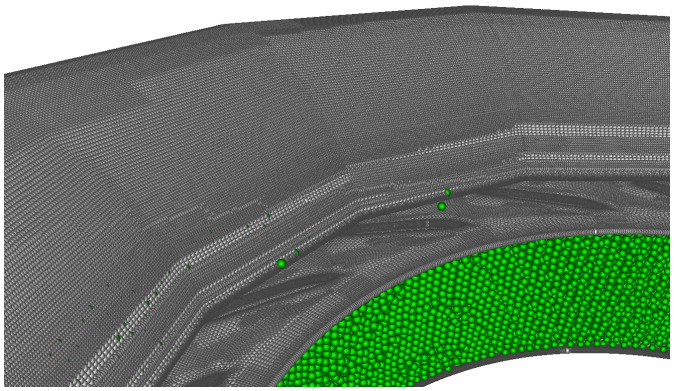

Figure 6.20.: Redundant particles after fluid domain generation and correction of position.

6.4.4. Reduction of the discretization error

After the fluid domain had been created, the previously described Bouscasse algorithm was used to decrease the discretization error of the generated fluid particles in the Cartesian scheme by repositioning them equally in the investigated domain (see Fig.6.21). During this

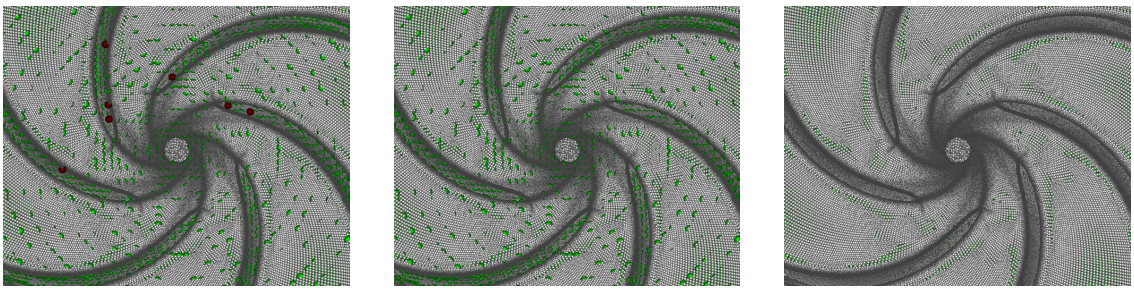

Figure 6.21.: Removing the redundant particles within the impeller blades and reallocation of the fluid particles.

process, this algorithm was modified for pump applications, where the re-positioning of the fluid particles at the interface between the rotating and stationary parts was allowed only in certain coordinate directions. This condition has been applied, for example, on the last particle layer (static) of draft tube and the first particle layer (rotating) in the runner (see Fig.6.22). This condition was also applied at the inlet and outlet boundary of the pump, in order to obtain a consistent layer.

A particle geometry was created between the runner outlet and the spiral casing inlet, which corresponds to a conical wall. In order to obtain a clear separation of the rotating particles in the runner and the static particles in the spiral casing, walls were created with normals

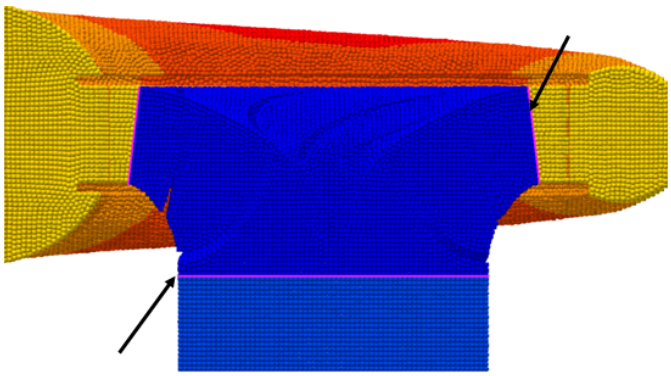

Figure 6.22.: Transition areas.

pointing in the respective domains (see Fig.6.23). By applying the Bouscasse algorithm, the particles were repositioned uniformly.

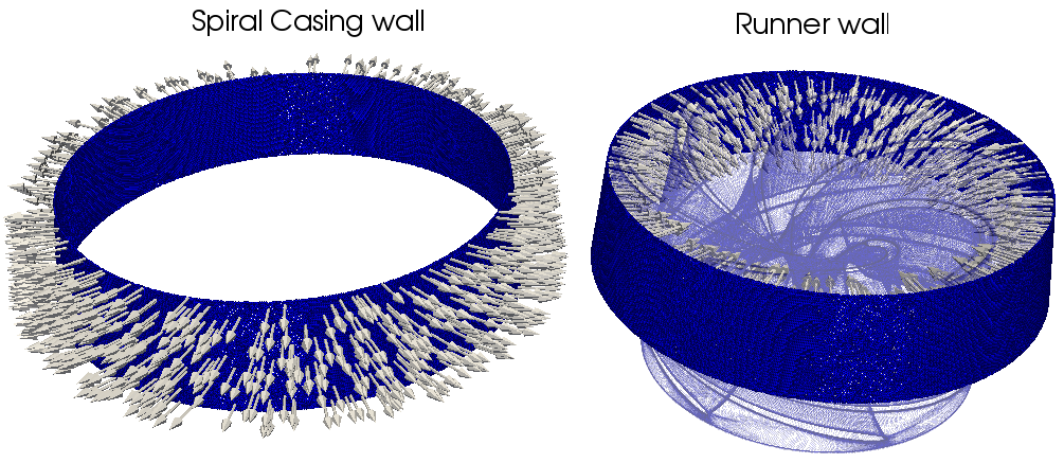

Figure 6.23.: Walls for the separation of rotating and static domain.

Finally, the generated fluid geometries were merged in a single VTK file. This is due to the structure of the initialization script, which requires a single fluid domain file for the entire pump. In order to consider the rotating section of the pump, attention has to be laid on the sequence in which the fluid geometries are merged. The rotating domain is selected first, followed by the remaining static geometries. This enabled implementing a condition, where the amount of fluid particles contained in the runner domain can be specified. Consequently, this amount of particles is subject to rotation.

Again it should be noted that this geometry creation process is not appropriate for industrial application, and should therefore only be applied for the purpose of direct validation with mesh-based methods.

7. Evaluation of the ANSYS CFX and Eulerkette results

The following chapter is devoted to the evaluation and comparison of the results, which have been carried out throughout this work. The investigated centrifugal pump with a specific speed of $n_q = 70$ has been developed prior to this work, during the development of a commercial project at the R&D department Graz. Detailed measurements at the test rig provided the basis for comparisons with numerical methods.

The n_q70 pump represents a complete pump unit, consisting of draft tube, runner and spiral casing (see. Fig.4.1). The aim of this development was the optimization of the total efficiency at optimum point and an improved part- and overload stability, in order to extend the field of application. The measurements on the test rig showed phenomena as the sudden drop of the characteristic pump curve (see Fig.7.2) near the optimum. This is consistent with the state of science, where fundamental research on separation zones and turbulent flows are being conducted in numerous research institutes. There are still no general formalisms known to describe these phenomena, which is why development continues to depend heavily on empirical data and experience. Due to this lack of knowledge, it is of great importance to minimize the errors connected to numerical methods in order to make these methods into a reliable tool for commercial developments.

The calculations were carried out with the FV method for different operating points. Since the code ASPHODEL is implemented with the Euler equations, this work examines more closely the optimum operating point, which - under restrictions - can be regarded as inviscid flow.

7.1. Eulerkette code

In evaluating the results, the conclusions of the calculations achieved by means of the so-called 'Eulerkette' represent the current state of technology of the hydraulic interpretation at the R&D site in Graz. The advantage of this code, developed by Dr. Arno Gehrer [1], is based on the efficient and rapid calculation of multiple pump and blade geometries within a very short time. Due to the preceding development of this project, the calculations and results were provided by the R&D department. These results were included together with the investigated methods. In the following, a brief description of the implemented methods can be found. Further details can be found in the publications of the author of the code [5].

1. Dr. Arno Gehrer developed this code during his employment as research and university assistant at the Institute of Thermal Turbomachinery and Machine Dynamics at Graz University of Technology.

This code has been developed in order to detect flow phenomena in blade rows of thermal turbomachines. Therefore, a time-dependent algorithm based on a cell-centred finite volume concept was created, which allowed to develop and evaluate individual tools, as efficient numerical algorithms or more advanced turbulence models, due to the modular structure of the code. For the convective terms (Euler flux balance), several discretization schemes were applied: a third-order accurate, TVD-Upwind scheme according to Roe (1981) and a central difference method, coupled with a non-linear artificial dissipation model. Two different time-stepping methods can be used independently of the user-specified spatial discretization. The governing equations are discretized in time either by using the Euler implicit method or alternatively by means of an explicit four stage Runge-Kutta scheme. For stationary problems, a local time stepping and a geometric multigrid method were included in order to accelerate convergence. The turbulent stresses are calculated using the Boussinesq approach (similar to Equ.(3.17)), which relates the turbulent stress tensor to the main strain tensor by an eddy viscosity.[5]

7.1.1. Euler Equations

This code was originally developed for research purposes, including the Navier-Stokes equations along with viscous terms. To accelerate the process of hydraulic design for the optimum point, the code was confined to inviscid and stationary calculations. If we neglect the viscous terms in the Navier-Stokes equations, these simplifying assumptions allow to describe the flow in the form of a simple system of equations called the Euler equations. This system can be written in conservative form and Cartesian coordinates as:

$$\frac{\partial \mathbf{U}}{\partial t} + \frac{\partial \mathbf{E}}{\partial x} + \frac{\partial \mathbf{F}}{\partial y} + \frac{\partial \mathbf{G}}{\partial z} = 0 \tag{7.1}$$

with the fluxes:

$$\mathbf{U} = \begin{pmatrix} \rho \\ \rho u \\ \rho v \\ \rho w \end{pmatrix}, \quad \mathbf{E} = \begin{pmatrix} \rho u \\ p + \rho u^2 \\ \rho uv \\ \rho uw \end{pmatrix}, \quad \mathbf{F} = \begin{pmatrix} \rho v \\ \rho uv \\ p + \rho v^2 \\ \rho vw \end{pmatrix}, \quad \mathbf{G} = \begin{pmatrix} \rho w \\ \rho uw \\ \rho vw \\ p + \rho w^2 \end{pmatrix} \tag{7.2}$$

where ρ represents the density, p the static pressure and u,v,w the Cartesian components of the velocity. The system of equations of the *Eulerkette* as well as of the following SPH method are established by neglecting the conservation of energy. The solver is a multiblock solver for incompressible 3D Euler flow. In this code the Euler equations are modified by an artificial compressibility. Convergence is accelerated by a *V-cycle* multigrid scheme.[18]

7.1.2. Model domain

For the Eulerkette simulation only the mesh of the impeller was used. This code allows the rapid generation and identification of a suitable impeller and blade geometry. Within a short time, numerous variations based on the design parameters can be evaluated and selected.

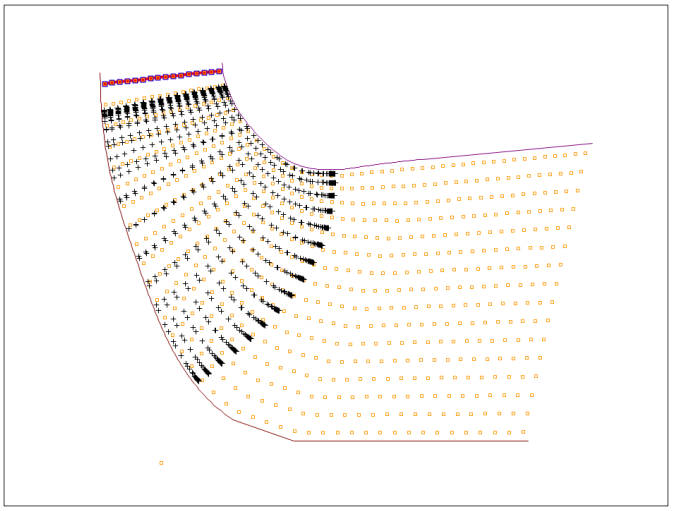

Figure 7.1.: Grid points of the Eulerkette calculations

Generally the Euler solver requires approximately one minute on a single CPU for 20,000 to 30,000 cells. This magnitude depends on the individual initial solution, boundary conditions and the applied CPU.

7.1.3. Boundary conditions

Basically, boundary conditions are imposed by the use of phantom cells. This is done through extension of the domain mesh by creating virtual cells. The values of the conservative variables $\mathbf{U}$ in the phantom cell are calculated in a way, that the value at the boundary (= mean value between phantom cell and the first inner cell), satisfies the corresponding condition. The discretization has to be consistent with the transport of information in a cell. Therefore, the informations entering the computational domain are replaced by boundary conditions, and information within the domain are transported outwards through extrapolation. Depending on the propagation speed it is possible to derive the number of boundary conditions to be imposed.

Generally, the following boundary conditions can be stated for three-dimensional subsonic flows:

Inlet
– 3 boundary conditions
  - stagnation pressure
  - velocity angle
– extrapolation of density ρ
Outlet
– 1 boundary condition
  - static pressure
– extrapolation of density ρ and velocity $\mathbf{v}$
Solid wall, inviscid
– 1 boundary condition $(\mathbf{v} - \mathbf{v}_g)\mathbf{n} = 0$ ($\mathbf{v}_g \ldots$ grid velocity)
– extrapolation of density ρ, pressure p and relative tangential velocity

The results from this code will be compared with the results from ANSYS CFX.

7.2. Post-processing of the CFX results

The operating points were selected together with the R&D department, where additionally to the BEP, points of interest were selected. The characteristic curve of the pump was calculated between $0.4 \leq Q/Q_N \leq 1.5$. For the the simulations two methods were applied, which have already been mentioned in chapter 4.6. One is the Frozen Rotor method, using the Shear Stress Transport and the k-ω turbulence models, and the other is the Sliding Mesh method for transient calculations, also using the SST model.

The evaluation of the results from the post-out files was performed by using an Excel calculation sheet, which assembled the results of the simulation and their corresponding time step outputs.

In the following, a brief description of the calculation procedure is given [10]. The notation is based on the simulations conducted on the same model with OpenFOAM at the R&D department in Graz.

specific speed n_q
Any pump application is characterized by the flow rate Q_{opt}, the head H_{opt} and the rotor speed n. These parameters determine to a large extent which impeller type and pump design is best suitable. Therefore, the specific speed n_q is introduced to describe the geometry of the impeller. The specific speed is often referred to as

$$n_q = \omega \cdot \frac{30}{\pi} \cdot \frac{\sqrt{Q}}{H^{\frac{3}{4}}} \tag{7.3}$$

or

$$n_s = 3,65 \cdot n_q \tag{7.4}$$

The specific speed of the investigated model resulted in $n_q = 70$.

Torque on the rotor

To verify the torque of the rotor, it is determined from the CFX calculations, firstly by summation of the torques effected on each mesh surface of the rotor,

$$T_{RN} = \quad T_{RN\_BL} + T_{RN\_HUB} + T_{RN\_SHR} \tag{7.5}$$

and secondly by means of the angular momentum.

$$T_{r\_c_u} = \quad -m_{RN\_in} \cdot (r \times c_u)_{RN\_in} + m_{RN\_out} \cdot (r \times c_u)_{RN\_out} \tag{7.6}$$

The flow velocity at DT inlet, defining the initial boundary condition, was calculated with:

$$c_m = \frac{m_{DT\_in}}{A_{DT\_in} \cdot \rho} \tag{7.7}$$

where ρ is specified at 20[°C] with $998\left[\frac{kg}{m^3}\right]$.

The total pressure is composed of the static and dynamic pressure at inlet and outlet of the pump, as:

$$p_{tot_{IEC}} = p_{stat} + \rho \cdot \frac{c_m^2}{2} \tag{7.8}$$

7.2.1. Head

The head was calculated according to the computed total pressure for each component as well as for the overall pump model:

draft tube $$H_{DT} = \frac{p_{tot_{DT\_out}} - p_{tot\_IEC_{DT\_in}}}{\rho \cdot g} \tag{7.9}$$

runner $$H_{RN} = \frac{p_{tot_{RN\_out}} - p_{tot_{RN\_in}}}{\rho \cdot g} \tag{7.10}$$

spiral casing $$H_{SP_{IEC}} = \frac{p_{tot\_IEC_{SC\_out}} - p_{tot_{SC\_in}}}{\rho \cdot g} \tag{7.11}$$

At the same time, the results were used to calculate the head inaccuracies at the interfaces:

$$H_{int} = (\mid p_{tot_{RN\_in}} - p_{tot_{DT\_out}} \mid + \mid p_{tot_{SC\_in}} - p_{tot_{RN\_out}} \mid) \frac{1}{\rho \cdot g} \tag{7.12}$$

In general the total head results from:

$$H_{tot} = (p_{tot\_IEC_{outlet}} - p_{tot\_IEC_{inlet}}) \frac{1}{\rho \cdot g} \tag{7.13}$$

The total head is calculated according to the IEC [2] regulations as:

$$\begin{aligned} H_{tot\_IEC} =& (p_{tot\_IEC_{SC\_out}} - p_{tot_{SC\_in}} + p_{tot_{RN\_out}} - p_{tot_{RN\_in}} \\ &+ p_{tot_{DT\_out}} - p_{tot\_IEC_{DT\_in}}) \frac{1}{\rho \cdot g} \end{aligned} \tag{7.14}$$

The purpose of this directive is the consideration of the interface errors of the employed methods.

The torque of the impeller which has to be transferred to the hydraulic flow is calculated according to:

$$H_{Torque} = T_{RN} \frac{\omega}{\rho \cdot g \cdot Q} \quad [m] \tag{7.15}$$

7.2.2. Efficiencies

The total efficiency according to IEC, taking the interface errors into consideration, results from:

$$\eta_{tot\_IEC} = \frac{H_{RN} + H_{SC\_IEC} + H_{DT}}{H_{Torque}} \cdot 100 \quad [\%] \tag{7.16}$$

The total efficiency without interface correction yields from:

$$\eta_{tot} = \frac{H_{tot}}{H_{Torque}} \cdot 100 \quad [\%] \tag{7.17}$$

Flow coefficient φ

For geometrically similar impellers, same kinematic conditions exist at a given flow coefficient regardless of size and speed. The flow coefficient φ is obtained according to:

$$\varphi_1 = \frac{c_{m1}}{u_1} = \frac{Q}{\frac{D^3_{RN\_out}}{8} \cdot \pi \cdot \omega} \tag{7.18}$$

$$\varphi_2 = \frac{c_{m2}}{u_2} = \frac{Q}{\frac{D^3_{RN\_in}}{8} \cdot \pi \cdot \omega} \tag{7.19}$$

2. IEC ... International Engineering Consultants

Pressure coefficient ψ
Since the kinematic ratio $\frac{c_u}{u}$ for model and prototype are of the same magnitude, a dimensionless pressure coefficient can be introduced independent of size and speed of the machine.

$$\psi_1 = \frac{H_{tot\_IEC} \cdot 2 \cdot g}{\left(\frac{D_{RN\_out}}{2} \cdot \omega\right)^2} \tag{7.20}$$

$$\psi_2 = \frac{H_{tot\_IEC} \cdot 2 \cdot g}{\left(\frac{D_{RN\_in}}{2} \cdot \omega\right)^2} \tag{7.21}$$

7.2.3. Verification of the interface errors

For the simulation with a grid-based method, different numerical errors arise. These inaccuracies can be evaluated for all investigated fluid parameters. Here we confine the evaluation on three parameters at the interfaces DT/RN and RN/SC (see 7.3.5).

$$\text{Pressure} \qquad \sigma_{p_{tot}} = 1 - \frac{p_{tot_{out}}}{p_{tot_{in}}} \tag{7.22}$$

$$\text{Swirl} \qquad \sigma_{r\_c_u} = 1 - \frac{(r \times c_u)_{out}}{(r \times c_u)_{in}} \tag{7.23}$$

$$\text{Flow rate} \qquad \sigma_Q = 1 - \frac{Q_{out}}{Q_{in}} \tag{7.24}$$

The flow rate error was evaluated for the entire pump as well as for the interfaces. The overall error between DT inlet and SC outlet led to a total error in the range of $2 \cdot 10^{-6}$ for the frozen rotor and transient calculation. The analysis revealed that the flow rate deviation between the interfaces is several orders of magnitude higher.

7.3. Pump characteristics

In the following, the results of the conducted calculations will be compared. Additionally, the provided measurement data and the results from the 'Eulerkette' calculations were included in the analysis. First, the Q-H und Q-η characteristics are compared and the prediction quality will be evaluated. 17 OP were determined for the FR calculations, which are found either in partload or overload, as well as at the BEP. Due to the significantly increased computational effort of the transient calculation, the number of OPs was confined to four.

For the analysis, the flow rate Q applied on the abscissa is related to the flow rate of the BEP. This non-dimensional representation was carried out on the ordinate for H and η.

All methods have in common, that they can locate and reproduce the BEP in an accurate manner. However, it should be noted that impeller sidewall gaps as well as mechanical losses were not taken into account. For this reason, in particular the conformity of the frozen-rotor results (red and green curves in Fig.7.2 and Fig.7.5) at the BEP are to be scrutinized. The description of the characteristics is done, starting from the highest flow rate towards decreasing flow rate concerning all respective methods. The local appearance of the hysteresis shows good correspondence with theory (see section 1.3.7), since the expected flow rate ranges between 70 and 90% (according to [6]) and complies with Fig.7.2.

7.3.1. Head capacity curve

The Q-H-curve of the investigated pump is presented below. Here the black solid line represents the measurements, where in the range of $Q/Q_{opt} = 0.7 \div 0.9$ we can divide the line into an upper and a lower curve. The upper curve is generated by throttling the flow into partload. The opposite applies for the lower curve.

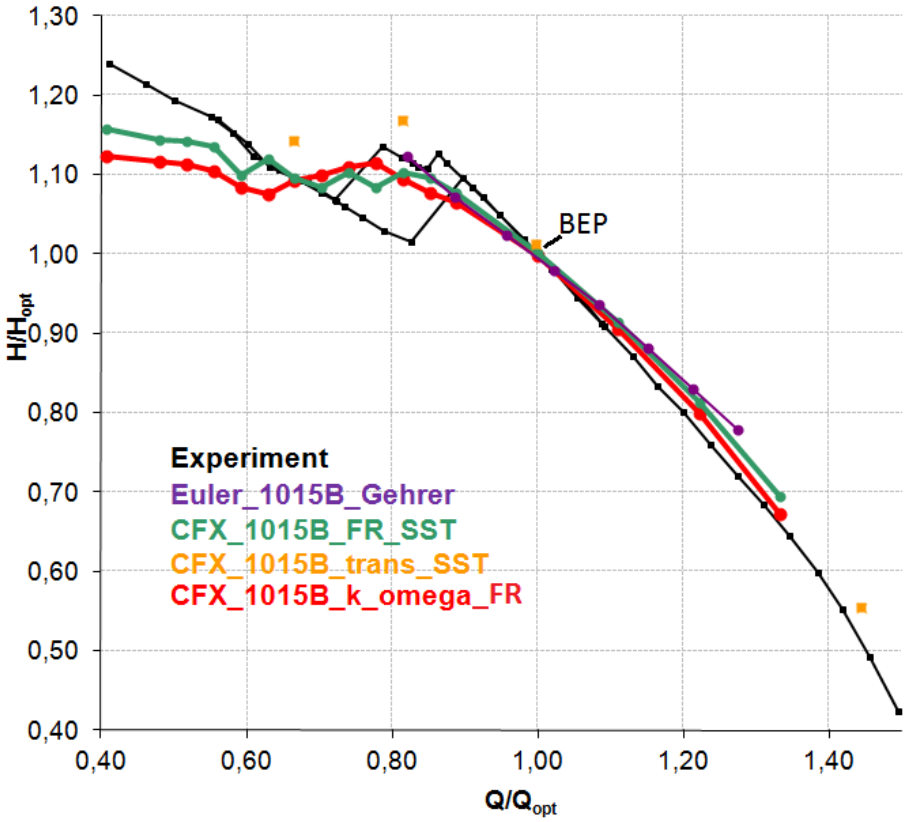

Figure 7.2.: Q-H-curve of the pump indicating the BEP.

7.3.1.1. Eulerkette

The Euler calculation for the BEP is in agreement with the measurements, which indicates the good applicability of this tool for the design of the impeller. These calculations were executed, prior to this work, during the period of the development of the pump. It is shown that this method can reproduce the BEP considering the flow rate very well. The deviation from the calculated H_{opt} at the design point is approximately 0.5%. The very fast and automated evaluation of geometry variations turns this FV method into an important tool with great advantages for the selection of the design.

7.3.1.2. Frozen Rotor

Several operating points were calculated to obtain a pump characteristic curve. These operating points were set in partload, overload as well as in the optimum point of the pump. The BEP was known because of previous calculations at the R&D department on the same model.

All presented CFX calculations were performed on the internal Linux cluster at the ASTROE department. The FR calculations were performed on Intel Core i7 CPUs with 3.47 GHz, 6 processors and 16GB RAM. The calculation of the optimum point lasted 2h30min for 500 iterations. The post processing took approximately 4% of the total simulation time, the rest accounted for the solver. The residual, which represents the termination criterion of the calculation was specified to 1.0E-5.

Shear Stress Transport turbulence model

Using the SST turbulence model for the calculations with the FR method led to the observation of interesting similarities between the partload range and the BEP. In overload slight disadvantages are observed in the head characteristic curve calculated with the SST model compared to the k-ω model. Beginning with the OP $Q/Q_{opt} = 1.33$ it is observed in Fig.7.2, that the SST model predicts the head 4% higher than the measurements. This difference decreases when reducing the flow rate, and achieves at the BEP a deviation with the measured value of +0.2%. This seems remarkable, as the mechanical and volumetric losses are neglected in the numerical calculations. Between the BEP and the area of the resulting hysteresis, the predicted head is mainly below the measurement, except for the last OP at $Q/Q_{opt} = 0.74$. During the test rig measurements it was found by the research engineers, that the first characteristic drop occurred due to flow separation in the stator vane at $Q/Q_{opt} = 0.86$. This was not confirmed by the numerical simulations in this particular OP. The head diminishes in this area compared to the upper curve, but the significant drop occurs later in the area of $Q/Q_{opt} = 0.8$. The severe drop which had been detected on the test rig between $Q/Q_{opt} = 0.72$ and 0.79, can be described by detachment of the flow at the impeller inlet. The obtained numerical results at $Q/Q_{opt} = 0.72$ show an approximately correct prediction of the characteristic drop. However, it is noted once again for the hysteresis, that a more precise analysis of the characteristic is required, which could be reached through more operating points in this range. It is also visible, that the onset or the location of these flow instabilities in the area of the hysteresis is not consistent with the measurement.

By further throttling the flow, the first OP following the hysteresis at $Q/Q_{opt} = 0.7$ shows again a good consensus with the head of approx. +0.4%. It is remarkable to observe the SST curve (green) at continuous reduction of the flow rate in the range of $Q/Q_{opt} = 0.6$, where a kink is noted. This area (near $Q/Q_{opt} = 0.6$) is characterized by separation and recirculation zones. The pictures in Figure 7.3 indicate at the cutwater, in the transition from the volute to the pressure tube, that the OPs show an evident recirculation zone at the *left* and *right* from $Q/Q_{opt} = 0.59$. This could be explained by the theory, that recirculations occur in partload, which generate a smaller effective cross section than the available geometric cross section. Analysing this OP the numerical result shows, that the recirculation zone collapsed, but this cannot be confirmed by observations on the test rig. The dark blue zones indicate areas of low flow velocity whereas bright regions show areas of higher velocity. Upon further reduction of the flow rate, the trend of increasing deviation between the numerical results and the measurement hardly allow conclusions.

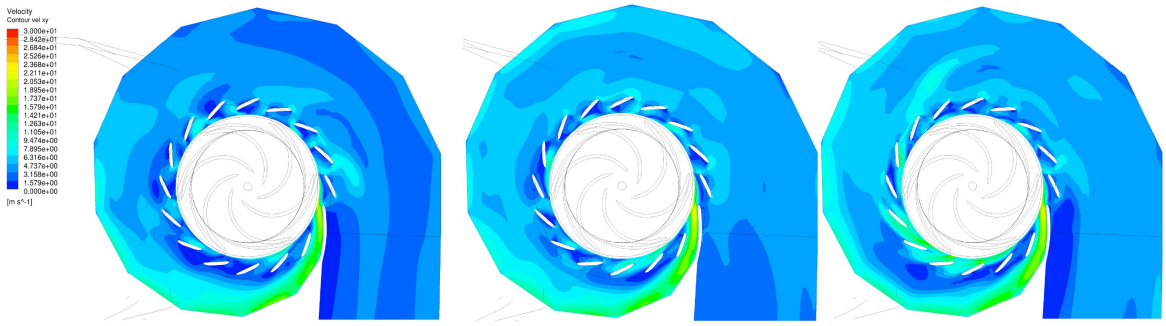

left: $Q/Q_{opt} = 0.51$ $Q/Q_{opt} = 0.59$ *right:* $Q/Q_{opt} = 0.62$

Figure 7.3.: Separation zone at the volute cutwater (velocity contours).

k-ω model

The discussion of the head is limited here to the values between the BEP and overload. Due to the large deviations of the FR k-ω results compared to the measurements and the SST model, it is decided to refrain from a detailed description of the hysteresis and partload area.

Generally it can be stated that the results of the k-ω model in overload altogether lie above the measurements, but are within the trend of the SST curve and the measured curve. The deviation at the maximum flow rate ($Q/Q_{opt} = 1.33$) is +1.5% and increases with decreasing Q. While approaching the BEP, the Q-H curve moves closer to the characteristic curve of the pump, and reaches in the BEP a deviation of -0.2%.

7.3.1.3. Transient

The transient calculations were launched by means of the sliding mesh method. Each of these simulations was run on 5 processors. Generally one can say that for the transient simulations,

it is of great importance that good initial solution of the operating point exists. This initial solution was taken from the Frozen Rotor calculations, which already passed 500 iterations.

Sliding Mesh SST

The considerably higher computational costs, which results from such transient calculations, has forced a restriction of the selected OPs. For this reason it was decided to perform these calculations at four points, namely the BEP, one OP in partload and overload, respectively and finally an OP within the hysteresis. In order to investigate the reproducibility of the flow effects in overload in a more visible manner, it was - subsequently to the FR calculations - decided to choose an OP further into overload ($Q/Q_{opt} = 1.44$) for the transient calculation.

The transient results overestimate both the Q-H as well as Q-η (Fig.7.5) characteristic curves throughout the investigated section. This is not really unexpected, due to neglecting various losses, such as mechanical and volumetric losses, so that the efficiency should lie therefore higher than the efficiency of the prototype. However, the efficiency of the pump in case of overload is so excessively higher, that it could be considered misleading in practice, when making conclusions referring to these results. The deviation measured for both η and the head is approx. +6%. With regard to the BEP, this difference decreases for η/η_{opt} to +1.6% and for H/H_{opt} to +1.26%. In the area of the hysteresis there is a deviation of about +5.8% for the efficiency and +4.2% for the head. Within the hysteresis it seems that, the OP in the Q-H diagram could be seen as a result from an extension of the upper branch - originating from the 'stable' side. Intersecting this extension with the part of the pump curve, which is caused by flow separation at the impeller inlet, could lead to the conclusion, that the measured kink in the stay vanes is not captured by the transient calculation. Ultimately, the deviation at partload ($Q/Q_{opt} = 0.64$) for η and H is +9.8% and +4.33%, respectively.

Figure 7.4 is in accordance with observations conducted in [6] page 528.

$Q < Q_{opt}$ Q_{opt} $Q > Q_{opt}$

Figure 7.4.: Separation zones in the spiral casing (velocity contours).

Although the transient calculation considers the rotation of the impeller, the results indicate that the modelling simplifications have a large impact. Therefore all influencing factors, such as impeller sidewall gaps and annular seals should be considered for an appropriate evaluation. Such cases have been investigated in several works [8] and [26].

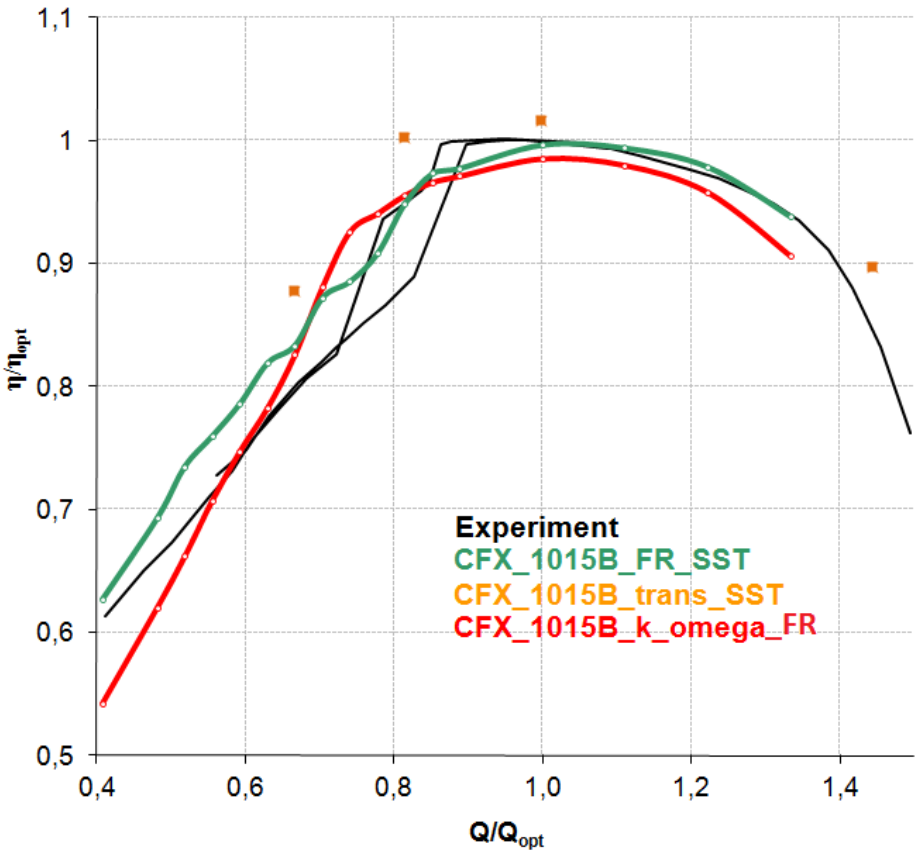

Figure 7.5.: Q-η-curve of the pump.

7.3.2. Efficiency curve

Next, the characteristic efficiency curves and the tendencies for the applied methods are described. Since the Eulerkette calculations were performed without viscous terms, an analysis of the efficiency is omitted. The numerical error of this method committed on the flow rate is in the range of 1.1%.

7.3.2.1. Frozen Rotor

SST model

The efficiency curve of the SST calculation shows at $Q/Q_{opt} = 1.33$ good accordance with the measurement. Here, the predicted value deviates by -0.4% from the measurement. With further decrease of the flow rate, the efficiency of the SST model exceeds the measurement values until reaching the BEP, with an accuracy of -0.3%. As decrease in flow rate continues, apparent discrepancies regarding the trend of what has already been observed in the Q-H curve are noted. However, the two OPs at $Q/Q_{opt} = 0.81$ and 0.85 are singled out, as they exceed the measurement results only by +0.17% and +0.64%, respectively. For this area,

it would be interesting to calculate more OPs, in order to better evaluate the effects of the flow in the pump. Decreasing the flow rate from $Q/Q_{opt} = 0.7$ shows that the efficiency curve significantly deviates (between 5 to 6%), but approaches the measurement towards the minimal partload point.

k-ω model
The efficiency curve of the k-ω model from the BEP to overload is located between 1.5 to 4% below the measured curve. This could be due to the weakness of this model described earlier in section 3.2.2, causing this approach to the overproduction of turbulent viscosity and thus effecting a delay or entire absence of boundary layer separations. In partload this turbulence model hardly allows conclusions, and is therefore not discussed.

7.3.3. Analysis of different operating points

In the following the transient results are evaluated and compared with the quasi-steady calculations.

7.3.3.1. BEP

At the BEP there is a good agreement between the results obtained from the FR and the transient FV methods in the Q-H curve. The integral values were determined over one revolution, as can be seen in Fig. 7.6. The pressure height of the FR calculation with the SST turbulent model lies near +0.2% above the measured value and -0.2% for the k-ω model. The transient result of this particular OP provides a head, which is in the range of 1.2% above the measured result. This could be expected when exclusively considering the hydraulic flow.

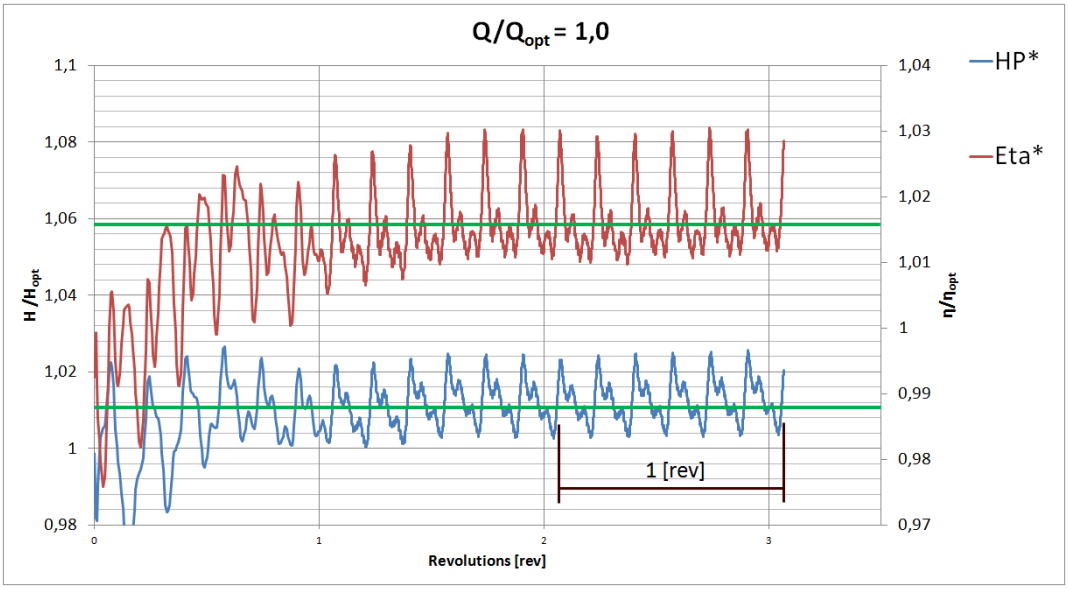

Figure 7.6.: Transient H and η plotted over the revolutions at the BEP.

The efficiency of the FR calculation with the SST turbulence model is about 0.3% lower than the measured value; the k-ω model deviates by -1.5%. The transient results in turn deliver an efficiency of 1.6% above the BEP, in a similar magnitude as the deviation of the head.

In summary, for the BEP the conclusion can be made, that the FR approach with the SST turbulence model provides good results on the predictability of the optimal operating point. The analysis of the transient calculation based on the post processing allows the conclusion, that - apart from periodic fluctuations - the flow is uniform at the circumference of the impeller outlet. The maximum of H and η are based on interactions between the impeller blades and the cutwater. This has been investigated and confirmed by verifying the data of the transient results.

The total computational time of the calculation shows clearly a disadvantage compared to the quasi-steady approach. The calculation requires approx. 1 revolution to stabilize the calculation. During this phase, a number of 50 coefficient loops (set as maximum) was necessary and required 30min for each timestep. After that phase, a number of 4 coefficient loops is sufficient to fulfill the residual target, comprising 4min per timestep. The simulation stabilizes after approx. 400 iterations, adapting the timestep automatically from initially 2° per iteration to finally 0.23°. The total number of iterations for the BEP is 3750, taking 500 iterations of the initial FR calculation into consideration. This yielded a total time of 164[h] for a physical time of 0.136[s] or 3 revolutions. The highest CFL number in the Runner resulted in 5.625. The simulation was run on 5 CPUs.

CPU requirements of numerical solution

The following table indicates a breakdown of the total calculation time for the BEP on individual operations:

Subsystem Name	Discretization	Linear Solution
Wallscale	2.3%	2%
Momentum and Mass	40.0%	9.9%
TurbKE and TurbFreq	11.1%	7.2%
Subsystem summary	**53.3%**	**19.2%**
Variable Updates	12.9%	
GGI intersection	0.5%	
Searches Calculations	0%	
File reading	0%	
File writing	8.4%	
Miscellaneous	5.7%	

7.3.3.2. Overload operating point

The operating point in overload was initially calculated for the two FR methods, which reached relatively good results compared to the measured data. As already mentioned in section 7.3, in order to investigate flow effects in overload in a more obvious manner, it was

decided to select an OP further into overload ($Q/Q_{opt} = 1.44$) to enable better comprehension for the transient results. Here, the integral values were again evaluated during one revolution (see Fig. 7.7).

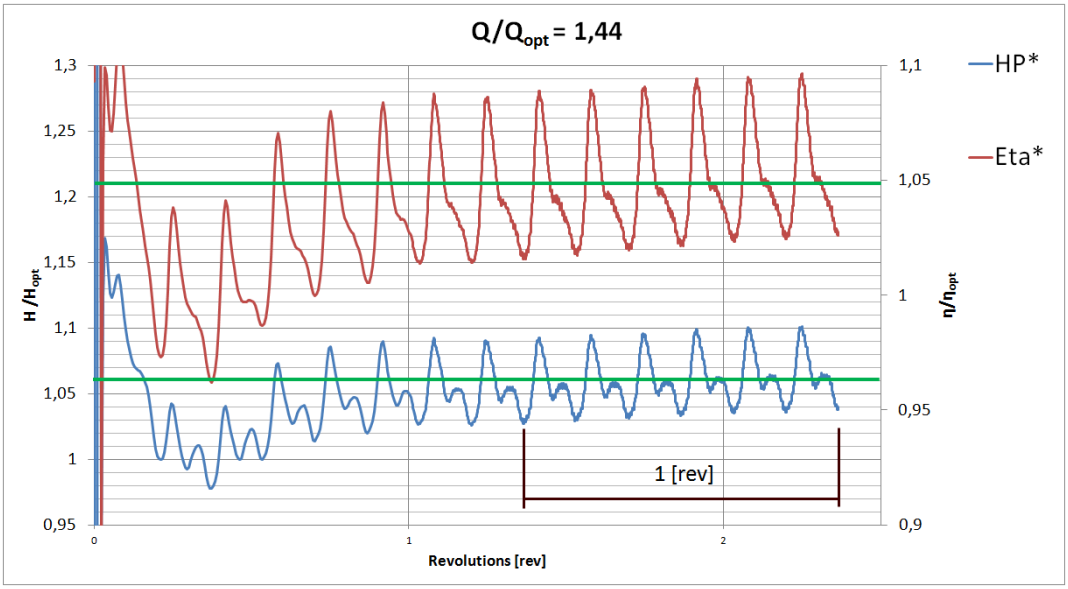

Figure 7.7.: Transient H and η plotted over revolutions at $Q/Q_{opt} = 1.44$.

Regarding the FR results it can be noted that both models (k-ω, SST) show higher pressure heads. The k-ω model lies with 1.5% deviation closer to the reference curve than the head of the SST calculation with 4%. The efficiency of the SST model is close to the measured point (-0.1%). In contrast, the k-ω model differs greatly from the measurement value and underestimates the efficiency by 3.5%.

The transient result (yellow) for the operating point in overload exceeds the pressure and efficiency level of the measurement by 6% and 3.6%, respectively.

In summary one can say that in overload the FR k-ω model reproduced the head level closer to the measurement, but compared to the SST model in turn greatly differs in efficiency.

7.3.3.3. Operating point within the hysteresis

The hysteresis is still a field in science, which bears many questions regarding its appearance and consequences, as stated in section 1.3.7. It is important to identify flow effects, where simple 1D-approaches may not necessarily show satisfactory reproduction. Therefore, research sets great efforts in the application of numerical methods, which could provide indications and explanations to the 3-dimensional effects. For this purpose, the results of the operating point at $Q/Q_{opt} = 0.81$ are subject to a more detailed analysis of the FV methods. The integral values were determined here throughout 2 revolutions.

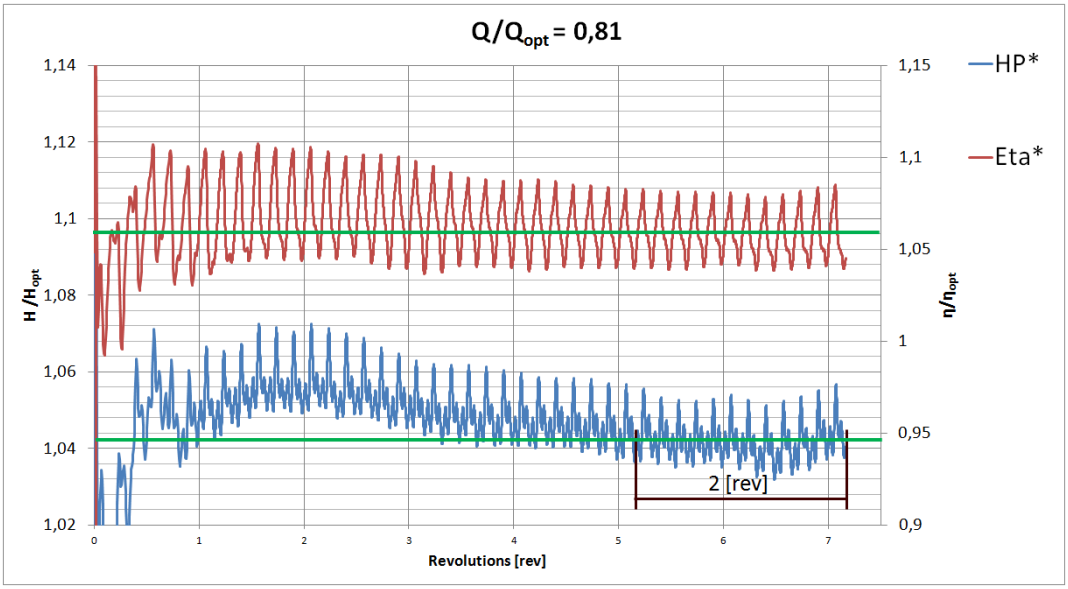

Figure 7.8.: Transient H and η plotted over the revolutions at $Q/Q_{opt} = 0.81$.

As described at the beginning of this chapter, flow separation takes place with decreasing flow rate after the BEP. This starts between the impeller outlet and stator, and is followed by a flow separation at the impeller inlet. The considered OP within the hysteresis is located directly between these two observed flow separations, which are detected by a drop in the Q-H as well as in the Q-η curve.

Although the onset of flow separation in the area of the hysteresis can be identified by the numerical results of the FR SST calculation, this result can not hide the fact, that the initial onset of the separation and eventual drop of the Q-H curve, appears dislocated compared to the measurement results. The head differs by -1.6% for the FR SST model and -2.4% for the FR calculation with the k-ω turbulence model.

The transient result at this particular OP exceeds the measured head by nearly 5%. Regarding the Q-H curve, it could be concluded that the chosen OP for the transient result does not predict the initial flow separation in the stator. However, while observing the Q-η curve, it is apparent that despite the increased head the efficiency declines compared to the BEP. Surprisingly, the efficiencies of the FR results show good correlation with the measured results (SST +0.2% ; k-ω +0.8%).

It can be generally noted, that the FR methods behave similarly, as they both (SST, $k-\omega$) overestimate the losses in the flow in relation to the Q-H curve (Fig.7.9). Despite the coarse distribution of the calculated OPs in this area, it could be concluded from the FR SST calculation, that the initial detachment of the flow in the stator vanes starts at the considered OP at $Q/Q_{opt} = 0.81$. Figure 7.10 shows the turbulent kinetic energy pattern of the considered point in the hysteresis with the adjacent left and right operating point calculated with the FR SST model. Based on the TKE, a glimpse of the beginning of the detachment is visible directly at the inlet guide vane. On closer examination, the *right* OP at $Q/Q_{opt} = 0.85$

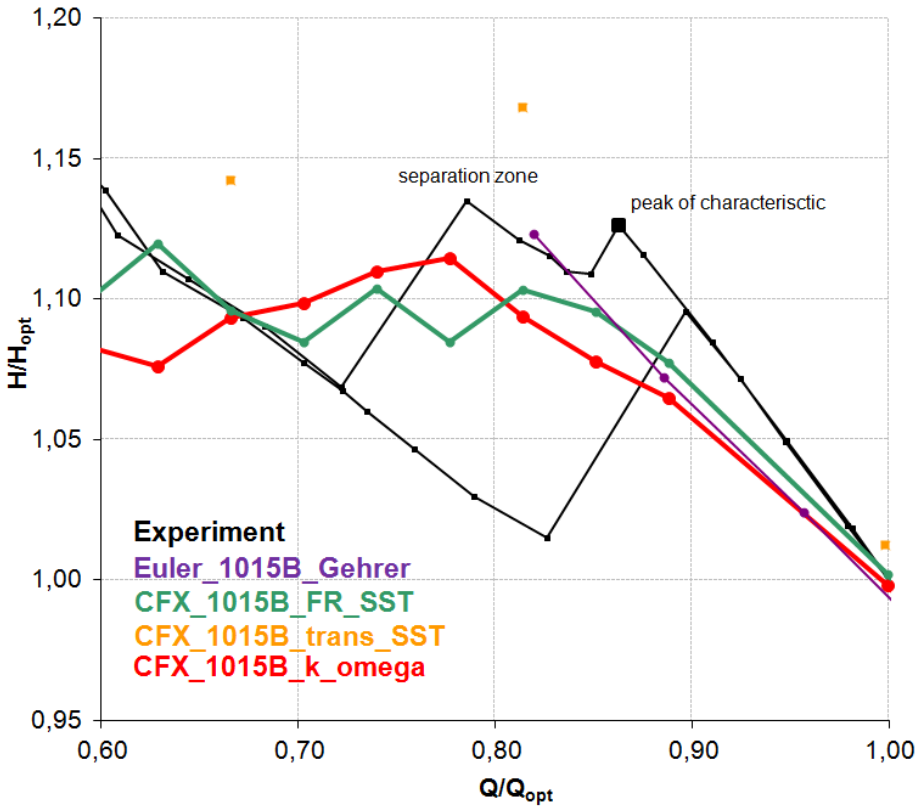

Figure 7.9.: Detail of the Q-H-curve - separation zone.

reveals, that the TKE is almost uniform at the circumference of the stator vane inlet. In contrast, at $Q/Q_{opt} = 0.81$ the TKE increases near the cutwater and affects the impeller channels, which is even more noticeable in the *left* OP.

A closer look at the flow conditions at the impeller inlet and outlet can be given by so-called 'turbo lines'. Hereby the swirl is evaluated along the channel inlet and outlet (Fig.7.11). This analysis gives an indication on the rate and position of $r \times c_u$. In Figure 7.12 the distribution of $r \times c_u$ between the different OPs can be observed at outlet (green) from hub (0) to shroud (1). The swirl remains almost unchanged close to the hub (the negative sign originates from the negative direction of rotation). The opposite can be found at the shroud, where $r_2 \times c_{u2}$ decreases with the flow, and thus coincides with the observation of the decreasing pressure head. The flow angle deviates at the outlet over the blade width only moderately, whereas the flow angle at the leading edge of the blades deviates on more than 20% alongside the channel width on the shroud side. This is consistent with the formation of recirculation zones, which have been elaborated in section 1.3.5.

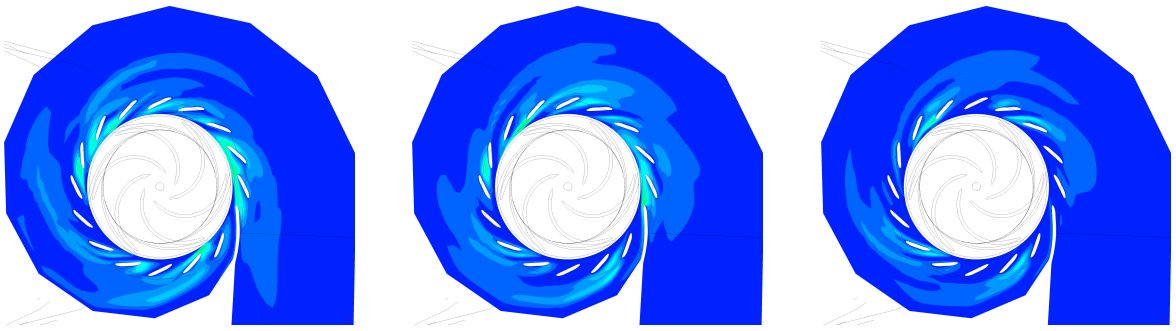

left of OP
$Q/Q_{opt} = 0.78$

OP
$Q/Q_{opt} = 0.81$

right of OP
$Q/Q_{opt} = 0.85$

Figure 7.10.: Turbulent kinetic energy within hysteresis (FR SST).

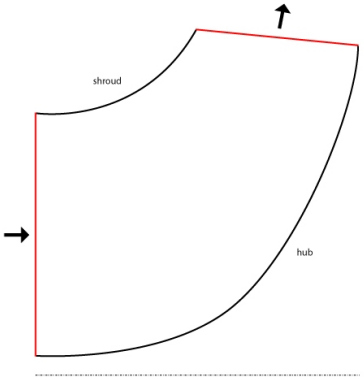

Figure 7.11.: Runner cross-section with turbolines (red).

7.3.3.4. Partload operating point

The next OP is situated in partload at $Q/Q_{opt} = 0.67$. This OP was chosen because of its proximity to the hysteresis. However, the flow in this area is stable, with regard to increasing and decreasing through-flow. It can be observed on the Q-H curve that the FR results coincide at this operating point. The SST model (green) shows a similar trend compared to the test rig measurements, whereas the k-ω model (red) reproduces only in this OP a good match with the measurements. The transient calculation provides an excess of the head of approx. 4%.

The efficiency for that point is exceeded by all methods. The transient result shows a deviation from the measured value of 8% and the quasi-steady methods show a deviation of 2.4% (k-ω) and 3.4% (SST).

In this operating point, the recirculation effects and their difficult prediction is apparent. This highlights the difficulties of three-dimensional effects in impeller channels as well as in the entire machine. These effects make reliable predictions for practical applications more

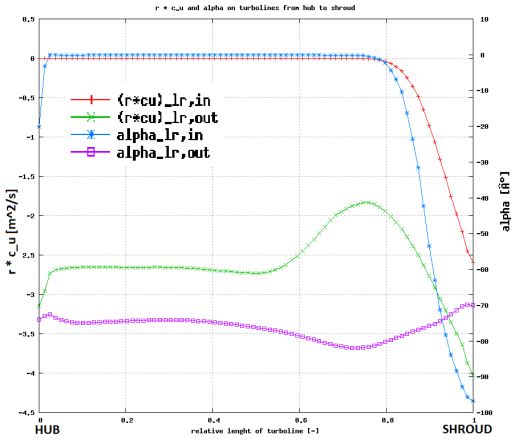

left of OP ($Q/Q_{opt} = 0.78$)

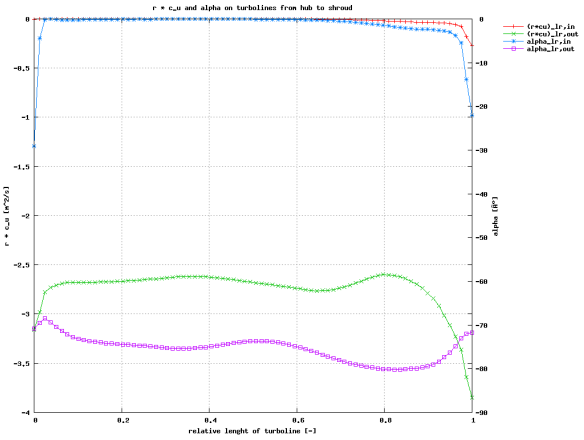

right of OP ($Q/Q_{opt} = 0.85$)

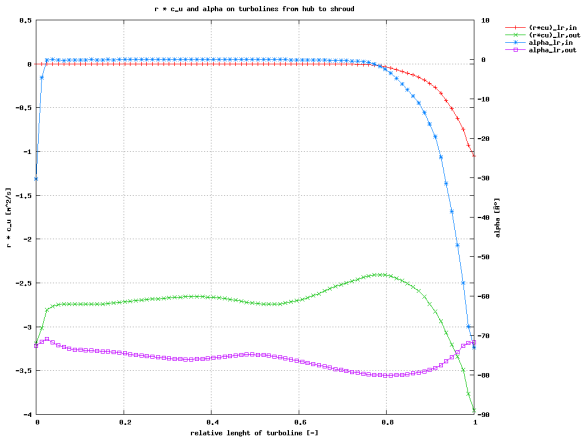

OP ($Q/Q_{opt} = 0.81$)

Figure 7.12.: $r \times c_u$ and flow angles along turbolines for an OP within hysteresis (FR SST).

difficult. The discussion here is confined to the qualitative comparison of the results with the described effects in section 1.3.3.

The cross-sectional reduction, caused by recirculation zones, can be determined in Fig.7.14. Herein it is shown - illustrated by the schematic vortex contours - that a recirculation zone develops at the outer streamline of the impeller inlet. The formation of this zone, and thus the resulting narrower inlet cross-section affects strongly the flow situation.

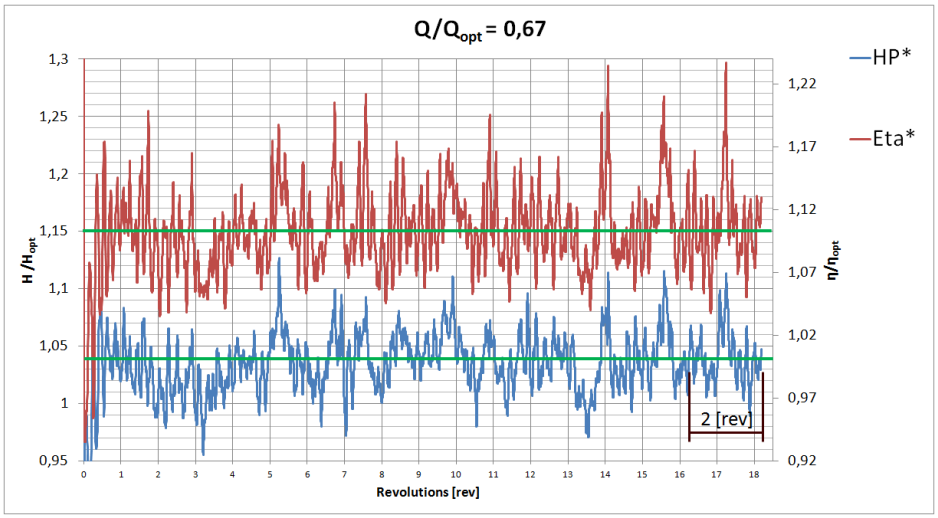

Figure 7.13.: Transient H and η plotted over the revolutions at $Q/Q_{opt} = 0.67$.

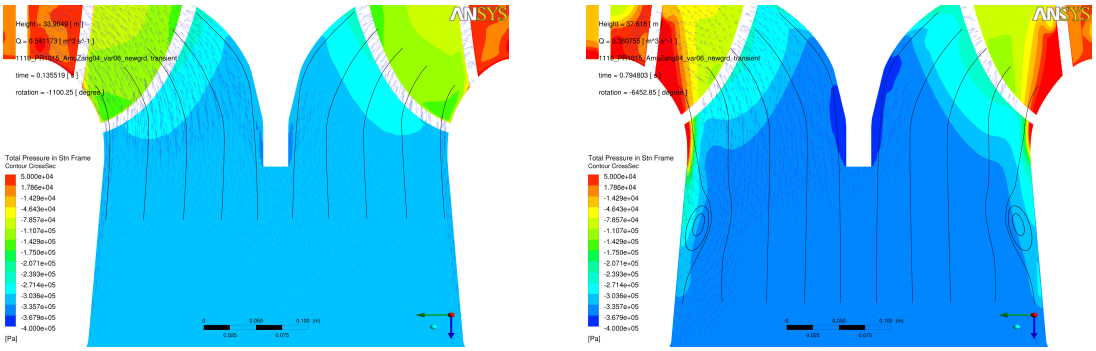

Figure 7.14.: Recirculation at impeller inlet; *left:* BEP, *right:* PL.

7.3.4. NPSH curve

If the pressure in a liquid drops below the vapour pressure, a portion of the fluid will evaporate, called cavitation. Around the blade leading edges areas with high flow velocities cause a local pressure drop, which may lead to partial evaporation. Extensive cavitation zones can impair the performance or even interrupt the flow. A relevant parameter for this effect is the *net positive suction head*, which is defined as the absolute suction head minus the vapour pressure p_v expressed as head.[6] Based on the NPSH behavior in partload operation, the effect of recirculation zones can be explained more accurately.

In general, the calculation of cavitation needs high computational costs. Therefore an estimation of the magnitude of the cavitation has been developed. This evaluation procedure is called a histogram analysis, which has proven itself as practicable. The NPSH value is calculated according to Equ.(7.25). The minimal pressure which is resulting on a specified area (here 1cm^2) of the impeller blade surfaces, is determined and is used to evaluate the $NPSH_{hist}$ value. An algorithm checks each cell for the occurring static pressure. Thus it is

evident that a hydraulic model - as the one observed with 100,000 elements on the blades - has a very high amount of data. For this reason this analysis was limited to the quasi-steady calculations. Fig.7.15 shows a drop of the NPSH value upon onset of flow separation in the stay vanes ($Q/Q_{opt} = 0.81$). The observations performed on the test rig are illustrated by the black curve.

$$NPSH = \frac{p_{tot,DT} - p_{hist}}{\rho g} \tag{7.25}$$

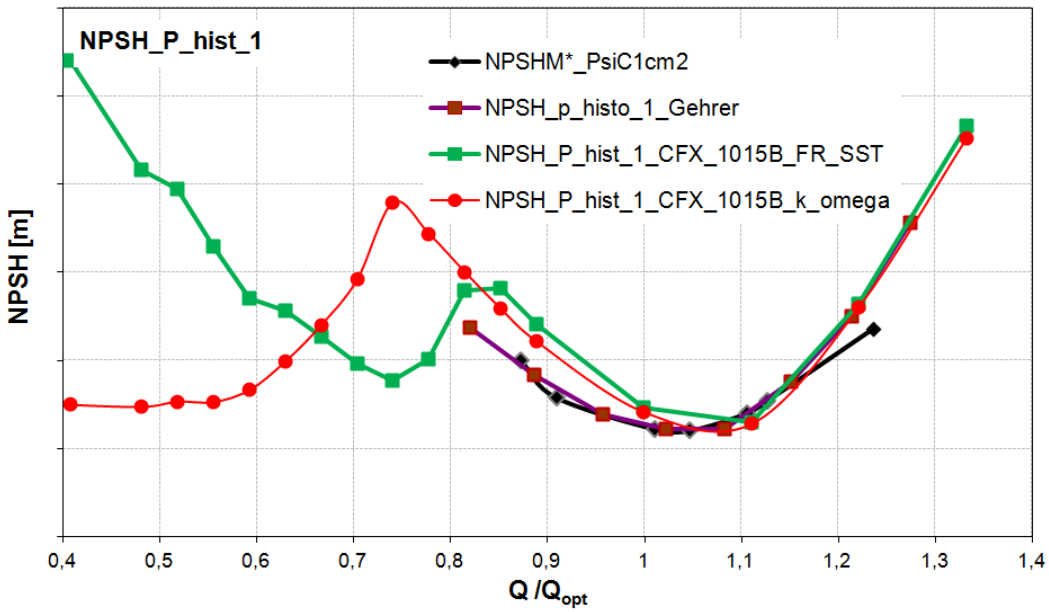

Figure 7.15.: NPSH histogram analysis.

The trend of the $NPSH_{hist,1cm^2}$ curve obtained by the Eulerkette shows a notable accordance with the measurements, however, no data was available in considerable partload. The two FR results do not match the trend and lie above the measured curve, but allow conclusions on the flow situation in partload.

7.3.5. Interface errors

According to the equations in section 7.2.3, an examination of the numeric error at the interfaces of the pump was carried out. This was initiated by the fact, that in the past inconsistencies in the results at the R&D department appeared. An analysis of the incoming and outgoing flow rate at the inlet and outlet of the entire pump shows a total deviation of less than 10^{-6}. This is an indication that the commercial code enforces the conservation of mass. A closer view on the fluxes at the interfaces shows, that this conservation is not found in the same accuracy, as the global examination suggests. For the following comparisons the OpenFOAM (OF) results have remained in the documentation (blue curve). The upper

graphs in Fig.7.16 show the interface errors encountered between the draft tube and runner, and the lower graphs indicate the errors at the impeller outlet between the runner and the spiral casing. The total pressure and swirl conservation of the methodology of OF is better in comparison to the ANSYS CFX results. Benefits arising from the latter code appear in the conservation of mass, particularly in the transient calculation.

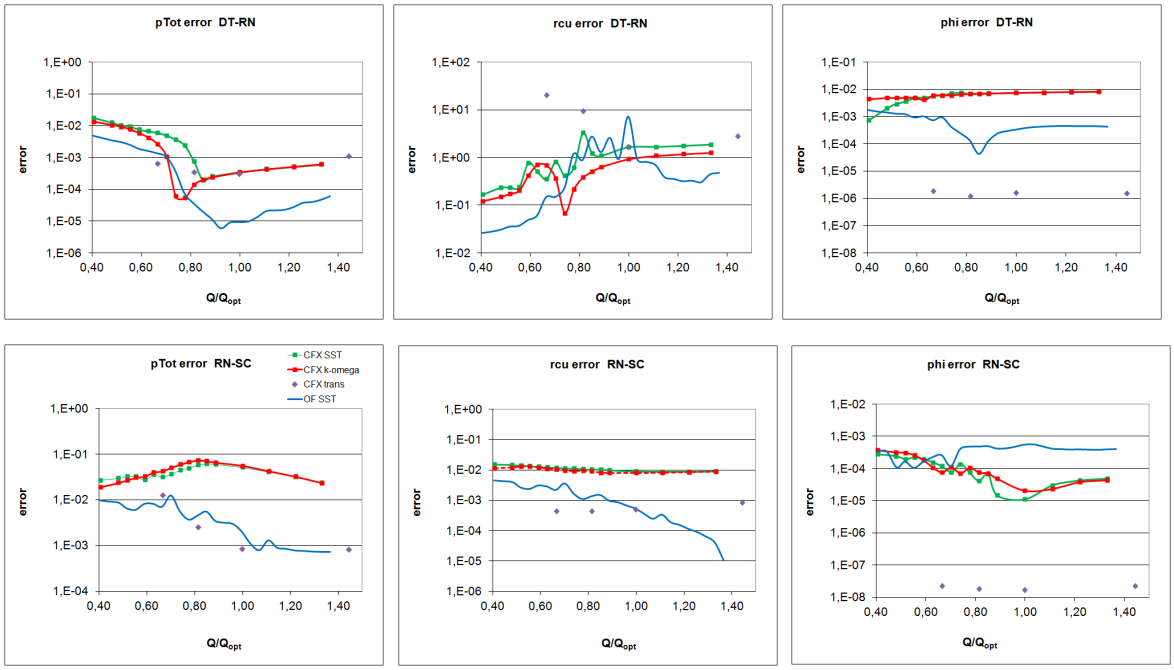

Figure 7.16.: Interface errors determined according to section 7.2.3.

In agreement with the R&D department in Graz it was decided to maintain the analysis of the executed calculations on a general comparison regarding each method. Because of the vast amount of data that have come forth from these calculations, it would be possible to perform further analysis in the unstable areas, e.g. by means of a FFT analysis. This could provide further information on the flow properties and more detailed information on the generation and onset of separation zones, which could cause phenomena as rotating stall.

7.4. Conclusion of the numerical results

The presented numerical results were acquired during the first part of this work. These results should serve as reference data for future comparison with the results from the ASPHODEL calculations.

From the results it can be concluded, that the quasi-stationary method generally has an advantage compared to the transient calculation. This is largely due to the fact that the applied model includes numerous model simplifications (neglection of disc friction, volumetric and mechanical losses). Despite correct reproduction of the rotor-stator-interaction, the results of the measurements are largely exceeded by the time-dependent method. Nevertheless, the obtained transient results allow conclusions on the transient flow behaviour within the pump at different rotor positions. For this purpose an analysis of the individual blade channels as well as a rotating stall analysis similar to [1] could implicate a clearer insight.

Comparing the two turbulence models applied here with the FR calculation, the SST method has proven itself as a viable approach. The close agreement of the calculated results with the characteristic curve at the BEP indicates its usefulness for the practical design of this prototype. It appeared, however, that these models are still of minor use for operating points apart from the design point. These OPs, affected by separation and recirculation zones, can hardly be described. In addition, the non-uniform three-dimensional flow formation within the pump increases the transient behaviour significantly. The k-ω model provides good results in the overload region of the Q-H curve, with the disadvantage of overestimation of the losses.

For a more detailed analysis of the numerical results within the hysteresis, a more detailed investigation of this area should be carried out. This could be reached by more operating points in this area.

The subsequent investigation of interface errors, which are a result of the mesh-based FV method, leads to the conclusion, that the interpolation errors between static and rotating mesh geometries are still a weakness of this method.

The post-processing and the obtained images had to fit at the first attempt, due to the limited time for the first part of this thesis. The obtained results were sufficient for the scope of this thesis, to enable a future evaluation of ASPHODEL regarding the BEP. Nonetheless, based on the experience gained, it would make sense in a future analysis to examine the area between rotor and stator in a more detailed manner.

Conclusion and future work

The present work is a contribution to the application of numerical methods concerning centrifugal pumps. In the course of this work, in a cooperation between the ANDRITZ GROUP sites in Graz and Vevey, the calculation of a centrifugal pump by means of various software packages available within the company was carried out. They are on one hand, the finite-volume-based commercial software ANSYS CFX and the in-house Euler code of the department ASTRÖ. The results of these two methods were assessed and will serve in future as a benchmark for the further development of a new in-house code developed in Vevey. This software, called ASPHODEL, is based on the Smoothed Particle Hydrodynamics method.

Using ANSYS CFX, a comparison between the Frozen Rotor and the transient method has been carried out, to get an overview on the applicability of these approaches by making a qualitative and quantitative evaluation regarding different turbulence models. It was found in agreement with the literature, that the SST model is more favourable than the k-ω model. In particular, the first TM captured the design point of the actual prototype quite well. Due to the model simplifications, the transient calculation allowed limited conclusions with regard to the measurement data. Based on the results, information on the flow effects within the pump could be identified. However, they could not be analyzed in detail for time reasons. It was necessary to make a comparison with two further simulation codes. These are the Eulerkette, which approximates well the characteristic curve of the pump near the design point, and the SPH-ALE method. The latter needed a lot of time and work including the implementation of a pump geometry originating from a grid-based geometry. The procedure will be used in future to compare the different numerical methods, and thus contribute to the further development of the code. The SPH method is under development and requires further research with regard to the correct implementation of boundary conditions. They are especially challenging in the Lagrangian formulation and need further quantitative investigations concerning the Eulerian formulation, which is currently in progress at the site in Vevey.

The further steps in terms of ASPHODEL are the implementation of a finite volume method within ASPHODEL, in order to take advantage of each method. Therefore a coupling is envisaged, which should resolve the near wall region with the finite-volume-method, allowing to apply existing turbulence models. The aim would be to reproduce the flow in the core by means of the Lagrangian formulation. Here it is essential to overcome obstacles such as the generation and destruction of particles at the boundaries and the numerical diffusion within this method. These developments could lead in future to an applicable numerical method regarding centrifugal pumps.

Appendix

The appendix includes the solver script for the frozen rotor (p.95-108) and transient settings (p.109-123) on the example of the BEP. The appendix also contains a hard drive handed out to the ASTROE department including the results, Excel files, post files, videos and presentations, which were generated during this work.

```
 This run of the CFX-12.0 Solver started at 21:05:27 on 03 May 2011
by
 user trainee01 on grzdlx054.graz.andritz.com
 (intel_xeon64.sse2_linux2.5) using the command:

  /graz/apps/ansys_inc/v120/CFX/bin/cfx5solve -batch -definition
My.def -ccl
    solve_AmuZang_newgrid.ccl

 Setting up CFX Solver run ...



+--------------------------------------------------------------------
+
 |
|
 |                     CFX Command Language Upgrade
|
 |
|

+--------------------------------------------------------------------
+

 Added /SIMULATION CONTROL/EXECUTION CONTROL/EXECUTABLE
SELECTION/Double
 Precision = Off.



+--------------------------------------------------------------------
+
 |
|
 |                     CFX Command Language for Run
|
 |
|

+--------------------------------------------------------------------
+

 LIBRARY:
   CEL:
     EXPRESSIONS:
       MPetagesIEC = (abs(massFlow()@RN_HP Side 1)/(997 [kg m^-3])) *
\
          (massFlowAve(Pressure)@RN_HP Side 1 + (massFlow()@RN_HP Side
\
          1/area()@RN_HP Side 1)^2/(2*997[kg m^-3]) - \
          massFlowAve(Pressure)@RN_LP Side 2 - (massFlow()@RN_LP Side
\
          2/area()@RN_LP Side 2)^2/(2*997 [kg m^-3]) ) / ( (torque_z()
@RN_BL + \
          torque_z()@RN_HUB + torque_z()@RN_SHR) * 141.7 [s^-1] )
     END
   END
   MATERIAL: Water
     Material Description = Water (liquid)
     Material Group = Water Data, Constant Property Liquids
     Option = Pure Substance
     Thermodynamic State = Liquid
     PROPERTIES:
       Option = General Material
       EQUATION OF STATE:
```

```
        Density = 997.0 [kg m^-3]
        Molar Mass = 18.02 [kg kmol^-1]
        Option = Value
      END
      SPECIFIC HEAT CAPACITY:
        Option = Value
        Specific Heat Capacity = 4181.7 [J kg^-1 K^-1]
        Specific Heat Type = Constant Pressure
      END
      REFERENCE STATE:
        Option = Specified Point
        Reference Pressure = 1 [atm]
        Reference Specific Enthalpy = 0.0 [J/kg]
        Reference Specific Entropy = 0.0 [J/kg/K]
        Reference Temperature = 25 [C]
      END
      DYNAMIC VISCOSITY:
        Dynamic Viscosity = 8.899E-4 [kg m^-1 s^-1]
        Option = Value
      END
      THERMAL CONDUCTIVITY:
        Option = Value
        Thermal Conductivity = 0.6069 [W m^-1 K^-1]
      END
      ABSORPTION COEFFICIENT:
        Absorption Coefficient = 1.0 [m^-1]
        Option = Value
      END
      SCATTERING COEFFICIENT:
        Option = Value
        Scattering Coefficient = 0.0 [m^-1]
      END
      REFRACTIVE INDEX:
        Option = Value
        Refractive Index = 1.0 [m m^-1]
      END
      THERMAL EXPANSIVITY:
        Option = Value
        Thermal Expansivity = 2.57E-04 [K^-1]
      END
    END
  END
END
FLOW: Flow Analysis 1
  SOLUTION UNITS:
    Angle Units = [rad]
    Length Units = [m]
    Mass Units = [kg]
    Solid Angle Units = [sr]
    Temperature Units = [K]
    Time Units = [s]
  END
  ANALYSIS TYPE:
    Option = Steady State
    EXTERNAL SOLVER COUPLING:
      Option = None
    END
  END
  DOMAIN: DT
    Coord Frame = Coord 0
    Domain Type = Fluid
    Location = Primitive 3D 4,Primitive 3D 5,Primitive 3D
6,Primitive 3D \
      7,Primitive 3D 8,Primitive 3D 9
    BOUNDARY: DT hub
      Boundary Type = WALL
```

```
      Location = INFLOW_BLOCK2,INFLOW_BLOCK3
      BOUNDARY CONDITIONS:
        MASS AND MOMENTUM:
          Option = No Slip Wall
          WALL VELOCITY:
            Angular Velocity = -141.7 [radian s^-1]
            Option = Rotating Wall
            AXIS DEFINITION:
              Option = Coordinate Axis
              Rotation Axis = Coord 0.3
            END
          END
        END
        WALL ROUGHNESS:
          Option = Smooth Wall
        END
      END
    END
    BOUNDARY: DT_HP
      Boundary Type = INTERFACE
      Location = INFLOW_BLOCK1
      BOUNDARY CONDITIONS:
        MASS AND MOMENTUM:
          Option = Conservative Interface Flux
        END
        TURBULENCE:
          Option = Conservative Interface Flux
        END
      END
    END
    BOUNDARY: DT_LP
      Boundary Type = INLET
      Location = OUTFLOW_BLOCK1 2,OUTFLOW_BLOCK2 2,OUTFLOW_BLOCK3 2
      BOUNDARY CONDITIONS:
        FLOW REGIME:
          Option = Subsonic
        END
        MASS AND MOMENTUM:
          Option = Cartesian Velocity Components
          U = -0.9847 [m s^-1]
          V = 0 [m s^-1]
          W = 0 [m s^-1]
        END
        TURBULENCE:
          Omega = 0.044 [s^-1]
          Option = k and Omega
          k = 0.000582 [m^2 s^-2]
        END
      END
    END
    BOUNDARY: DT_WALL
      Boundary Type = WALL
      Location = SHROUD_BLOCK1,SHROUD_BLOCK1 2,SHROUD_BLOCK1
3,SHROUD_BLOCK1 \
        4,SHROUD_BLOCK1 5,SHROUD_BLOCK1 6
      BOUNDARY CONDITIONS:
        MASS AND MOMENTUM:
          Option = No Slip Wall
        END
        WALL ROUGHNESS:
          Option = Smooth Wall
        END
      END
    END
    DOMAIN MODELS:
      BUOYANCY MODEL:
```

```
      Option = Non Buoyant
    END
    DOMAIN MOTION:
      Option = Stationary
    END
    MESH DEFORMATION:
      Option = None
    END
    REFERENCE PRESSURE:
      Reference Pressure = 1 [atm]
    END
  END
  FLUID DEFINITION: Fluid 1
    Material = Water
    Option = Material Library
    MORPHOLOGY:
      Option = Continuous Fluid
    END
  END
  FLUID MODELS:
    COMBUSTION MODEL:
      Option = None
    END
    HEAT TRANSFER MODEL:
      Fluid Temperature = 25 [C]
      Option = Isothermal
    END
    THERMAL RADIATION MODEL:
      Option = None
    END
    TURBULENCE MODEL:
      Option = SST
    END
    TURBULENT WALL FUNCTIONS:
      Option = Automatic
    END
  END
  INITIALISATION:
    Option = Automatic
    INITIAL CONDITIONS:
      Velocity Type = Cylindrical
      CYLINDRICAL VELOCITY COMPONENTS:
        Option = Automatic with Value
        Velocity Axial Component = -3 [m s^-1]
        Velocity Theta Component = 0 [m s^-1]
        Velocity r Component = 1 [m s^-1]
        AXIS DEFINITION:
          Option = Coordinate Axis
          Rotation Axis = Coord 0.3
        END
      END
      STATIC PRESSURE:
        Option = Automatic with Value
        Relative Pressure = -20e4 [Pa]
      END
      TURBULENCE INITIAL CONDITIONS:
        Option = Medium Intensity and Eddy Viscosity Ratio
      END
    END
  END
END
DOMAIN: RN
  Coord Frame = Coord 0
  Domain Type = Fluid
  Location = Assembly 10
  BOUNDARY: RN_BL
```

```
      Boundary Type = WALL
      Frame Type = Rotating
      Location = BLADE,BLADE 2,BLADE 3,BLADE 4,BLADE 5,BLADE 6
      BOUNDARY CONDITIONS:
        MASS AND MOMENTUM:
          Option = No Slip Wall
        END
        WALL ROUGHNESS:
          Option = Smooth Wall
        END
      END
    END
    BOUNDARY: RN_HP Side 1
      Boundary Type = INTERFACE
      Location = WEST,WEST 2,WEST 3,WEST 4,WEST 5,WEST 6
      BOUNDARY CONDITIONS:
        MASS AND MOMENTUM:
          Option = Conservative Interface Flux
        END
        TURBULENCE:
          Option = Conservative Interface Flux
        END
      END
    END
    BOUNDARY: RN_HUB
      Boundary Type = WALL
      Frame Type = Rotating
      Location = HUB,HUB 2,HUB 3,HUB 4,HUB 5,HUB 6,HUB_EAST,HUB_EAST
\
        2,HUB_EAST 3,HUB_EAST 4,HUB_EAST 5,HUB_EAST 6
      BOUNDARY CONDITIONS:
        MASS AND MOMENTUM:
          Option = No Slip Wall
        END
        WALL ROUGHNESS:
          Option = Smooth Wall
        END
      END
    END
    BOUNDARY: RN_LP Side 2
      Boundary Type = INTERFACE
      Location = EAST,EAST 2,EAST 3,EAST 4,EAST 5,EAST 6
      BOUNDARY CONDITIONS:
        MASS AND MOMENTUM:
          Option = Conservative Interface Flux
        END
        TURBULENCE:
          Option = Conservative Interface Flux
        END
      END
    END
    BOUNDARY: RN_SHR
      Boundary Type = WALL
      Frame Type = Rotating
      Location = SHROUD,SHROUD 2,SHROUD 3,SHROUD 4,SHROUD 5,SHROUD \
        6,SHROUD_EAST,SHROUD_EAST 2,SHROUD_EAST 3,SHROUD_EAST
4,SHROUD_EAST \
        5,SHROUD_EAST 6
      BOUNDARY CONDITIONS:
        MASS AND MOMENTUM:
          Option = No Slip Wall
        END
        WALL ROUGHNESS:
          Option = Smooth Wall
        END
      END
```

```
END
DOMAIN MODELS:
  BUOYANCY MODEL:
    Option = Non Buoyant
  END
  DOMAIN MOTION:
    Alternate Rotation Model = On
    Angular Velocity = -141.7 [radian s^-1]
    Option = Rotating
    AXIS DEFINITION:
      Option = Coordinate Axis
      Rotation Axis = Coord 0.3
    END
  END
  MESH DEFORMATION:
    Option = None
  END
  REFERENCE PRESSURE:
    Reference Pressure = 1 [atm]
  END
END
FLUID DEFINITION: Fluid 1
  Material = Water
  Option = Material Library
  MORPHOLOGY:
    Option = Continuous Fluid
  END
END
FLUID MODELS:
  COMBUSTION MODEL:
    Option = None
  END
  HEAT TRANSFER MODEL:
    Fluid Temperature = 25 [C]
    Option = Isothermal
  END
  THERMAL RADIATION MODEL:
    Option = None
  END
  TURBULENCE MODEL:
    Option = SST
  END
  TURBULENT WALL FUNCTIONS:
    Option = Automatic
  END
END
INITIALISATION:
  Frame Type = Rotating
  Option = Automatic
  INITIAL CONDITIONS:
    Velocity Type = Cylindrical
    CYLINDRICAL VELOCITY COMPONENTS:
      Option = Automatic with Value
      Velocity Axial Component = -3 [m s^-1]
      Velocity Theta Component = 0 [m s^-1]
      Velocity r Component = 1 [m s^-1]
    END
    STATIC PRESSURE:
      Option = Automatic with Value
      Relative Pressure = -20e4 [Pa]
    END
    TURBULENCE INITIAL CONDITIONS:
      Option = Medium Intensity and Eddy Viscosity Ratio
    END
  END
END
```

```
   END
   DOMAIN: SC
     Coord Frame = Coord 0
     Domain Type = Fluid
     Location = Primitive 3D
     BOUNDARY: SC_BL
       Boundary Type = WALL
       Location = Primitive 2D B,Primitive 2D C,Primitive 2D
D,Primitive 2D \
         E,Primitive 2D F,Primitive 2D G,Primitive 2D H,Primitive 2D
\
         I,Primitive 2D J,Primitive 2D K,Primitive 2D L,Primitive 2D
\
         M,Primitive 2D N,Primitive 2D O,Primitive 2D P,Primitive 2D
Q
       BOUNDARY CONDITIONS:
         MASS AND MOMENTUM:
           Option = No Slip Wall
         END
         WALL ROUGHNESS:
           Option = Smooth Wall
         END
       END
     END
     BOUNDARY: SC_GGI_DE Side 1
       Boundary Type = INTERFACE
       Location = SC_GGI_DE_A
       BOUNDARY CONDITIONS:
         MASS AND MOMENTUM:
           Option = Conservative Interface Flux
         END
         TURBULENCE:
           Option = Conservative Interface Flux
         END
       END
     END
     BOUNDARY: SC_GGI_DE Side 2
       Boundary Type = INTERFACE
       Location = SC_GGI_DE_B
       BOUNDARY CONDITIONS:
         MASS AND MOMENTUM:
           Option = Conservative Interface Flux
         END
         TURBULENCE:
           Option = Conservative Interface Flux
         END
       END
     END
     BOUNDARY: SC_GGI_SEP_B
       Boundary Type = INTERFACE
       Location = SC_GGI_SEP_B
       BOUNDARY CONDITIONS:
         MASS AND MOMENTUM:
           Option = Conservative Interface Flux
         END
         TURBULENCE:
           Option = Conservative Interface Flux
         END
       END
     END
     BOUNDARY: SC_LP
       Boundary Type = INTERFACE
       Location = SC_LP
       BOUNDARY CONDITIONS:
         MASS AND MOMENTUM:
           Option = Conservative Interface Flux
```

```
    END
    TURBULENCE:
      Option = Conservative Interface Flux
    END
  END
END
BOUNDARY: SC_WALL
  Boundary Type = WALL
  Location = Primitive 2D
  BOUNDARY CONDITIONS:
    MASS AND MOMENTUM:
      Option = No Slip Wall
    END
    WALL ROUGHNESS:
      Option = Smooth Wall
    END
  END
END
DOMAIN MODELS:
  BUOYANCY MODEL:
    Option = Non Buoyant
  END
  DOMAIN MOTION:
    Option = Stationary
  END
  MESH DEFORMATION:
    Option = None
  END
  REFERENCE PRESSURE:
    Reference Pressure = 1 [atm]
  END
END
FLUID DEFINITION: Fluid 1
  Material = Water
  Option = Material Library
  MORPHOLOGY:
    Option = Continuous Fluid
  END
END
FLUID MODELS:
  COMBUSTION MODEL:
    Option = None
  END
  HEAT TRANSFER MODEL:
    Fluid Temperature = 25 [C]
    Option = Isothermal
  END
  THERMAL RADIATION MODEL:
    Option = None
  END
  TURBULENCE MODEL:
    Option = SST
  END
  TURBULENT WALL FUNCTIONS:
    Option = Automatic
  END
END
INITIALISATION:
  Option = Automatic
  INITIAL CONDITIONS:
    Velocity Type = Cylindrical
    CYLINDRICAL VELOCITY COMPONENTS:
      Option = Automatic with Value
      Velocity Axial Component = 0 [m s^-1]
      Velocity Theta Component = -1 [m s^-1]
      Velocity r Component = 1 [m s^-1]
```

```
        AXIS DEFINITION:
          Option = Coordinate Axis
          Rotation Axis = Coord 0.3
        END
      END
      STATIC PRESSURE:
        Option = Automatic with Value
        Relative Pressure = 0 [Pa]
      END
      TURBULENCE INITIAL CONDITIONS:
        Option = Medium Intensity and Eddy Viscosity Ratio
      END
    END
  END
END
DOMAIN: SC SEP
  Coord Frame = Coord 0
  Domain Type = Fluid
  Location = Assembly 9
  BOUNDARY: SC_GGI_SEP_A
    Boundary Type = INTERFACE
    Location = SC_GGI_SEP_A
    BOUNDARY CONDITIONS:
      MASS AND MOMENTUM:
        Option = Conservative Interface Flux
      END
      TURBULENCE:
        Option = Conservative Interface Flux
      END
    END
  END
  BOUNDARY: SC_HP
    Boundary Type = OUTLET
    Location = SC_HP
    BOUNDARY CONDITIONS:
      FLOW REGIME:
        Option = Subsonic
      END
      MASS AND MOMENTUM:
        Option = Static Pressure
        Relative Pressure = 0 [Pa]
      END
    END
  END
  BOUNDARY: SC_SEP_WALL
    Boundary Type = WALL
    Location = Primitive 2D A
    BOUNDARY CONDITIONS:
      MASS AND MOMENTUM:
        Option = No Slip Wall
      END
      WALL ROUGHNESS:
        Option = Smooth Wall
      END
    END
  END
  DOMAIN MODELS:
    BUOYANCY MODEL:
      Option = Non Buoyant
    END
    DOMAIN MOTION:
      Option = Stationary
    END
    MESH DEFORMATION:
      Option = None
    END
```

```
    REFERENCE PRESSURE:
      Reference Pressure = 1 [atm]
    END
  END
  FLUID DEFINITION: Fluid 1
    Material = Water
    Option = Material Library
    MORPHOLOGY:
      Option = Continuous Fluid
    END
  END
  FLUID MODELS:
    COMBUSTION MODEL:
      Option = None
    END
    HEAT TRANSFER MODEL:
      Fluid Temperature = 25 [C]
      Option = Isothermal
    END
    THERMAL RADIATION MODEL:
      Option = None
    END
    TURBULENCE MODEL:
      Option = SST
    END
    TURBULENT WALL FUNCTIONS:
      Option = Automatic
    END
  END
  INITIALISATION:
    Option = Automatic
    INITIAL CONDITIONS:
      Velocity Type = Cartesian
      CARTESIAN VELOCITY COMPONENTS:
        Option = Automatic with Value
        U = 0 [m s^-1]
        V = 1 [m s^-1]
        W = 0 [m s^-1]
      END
      STATIC PRESSURE:
        Option = Automatic
      END
      TURBULENCE INITIAL CONDITIONS:
        Option = Medium Intensity and Eddy Viscosity Ratio
      END
    END
  END
END
DOMAIN INTERFACE: RN_HP
  Boundary List1 = RN_HP Side 1
  Boundary List2 = SC_LP
  Interface Type = Fluid Fluid
  INTERFACE MODELS:
    Option = General Connection
    FRAME CHANGE:
      Option = Frozen Rotor
    END
    MASS AND MOMENTUM:
      Option = Conservative Interface Flux
      MOMENTUM INTERFACE MODEL:
        Option = None
      END
    END
    PITCH CHANGE:
      Option = Specified Pitch Angles
      Pitch Angle Side1 = 360 [degree]
```

```
      Pitch Angle Side2 = 360 [degree]
    END
  END
  MESH CONNECTION:
    Option = GGI
    INTERSECTION CONTROL:
      Option = Direct
    END
  END
END
DOMAIN INTERFACE: RN_LP
  Boundary List1 = DT_HP
  Boundary List2 = RN_LP Side 2
  Interface Type = Fluid Fluid
  INTERFACE MODELS:
    Option = General Connection
    FRAME CHANGE:
      Option = Frozen Rotor
    END
    MASS AND MOMENTUM:
      Option = Conservative Interface Flux
      MOMENTUM INTERFACE MODEL:
        Option = None
      END
    END
    PITCH CHANGE:
      Option = Specified Pitch Angles
      Pitch Angle Side1 = 360 [degree]
      Pitch Angle Side2 = 360 [degree]
    END
  END
  MESH CONNECTION:
    Option = GGI
    INTERSECTION CONTROL:
      Option = Direct
    END
  END
END
DOMAIN INTERFACE: SC_GGI_DE
  Boundary List1 = SC_GGI_DE Side 1
  Boundary List2 = SC_GGI_DE Side 2
  Interface Type = Fluid Fluid
  INTERFACE MODELS:
    Option = General Connection
    FRAME CHANGE:
      Option = None
    END
    MASS AND MOMENTUM:
      Option = Conservative Interface Flux
      MOMENTUM INTERFACE MODEL:
        Option = None
      END
    END
    PITCH CHANGE:
      Option = None
    END
  END
  MESH CONNECTION:
    Option = GGI
    INTERSECTION CONTROL:
      Option = Direct
    END
  END
END
DOMAIN INTERFACE: SC_GGI_SEP
  Boundary List1 = SC_GGI_SEP_B
```

```
    Boundary List2 = SC_GGI_SEP_A
    Interface Type = Fluid Fluid
    INTERFACE MODELS:
      Option = General Connection
      FRAME CHANGE:
        Option = None
      END
      MASS AND MOMENTUM:
        Option = Conservative Interface Flux
        MOMENTUM INTERFACE MODEL:
          Option = None
        END
      END
      PITCH CHANGE:
        Option = None
      END
    END
    MESH CONNECTION:
      Option = GGI
      INTERSECTION CONTROL:
        Option = Direct
      END
    END
  END
  OUTPUT CONTROL:
    MONITOR OBJECTS:
      MONITOR BALANCES:
        Option = Full
      END
      MONITOR FORCES:
        Option = Full
      END
      MONITOR PARTICLES:
        Option = Full
      END
      MONITOR POINT: MPetagesIEC
        Expression Value = (abs(massFlow()@RN_HP Side 1)/(997 [kg
m^-3])) * \
          ( massFlowAve(Pressure)@RN_HP Side 1 + (massFlow()@RN_HP
Side \
          1/area()@RN_HP Side 1)^2/(2*997[kg m^-3]) \
          -massFlowAve(Pressure)@RN_LP Side 2 - (massFlow()@RN_LP
Side \
          2/area()@RN_LP Side 2)^2/(2*997 [kg m^-3]) ) / ( (torque_z
()@RN_BL \
          + torque_z()@RN_HUB + torque_z()@RN_SHR) * 141.7 [s^-1] )
        Option = Expression
      END
      MONITOR RESIDUALS:
        Option = Full
      END
      MONITOR TOTALS:
        Option = Full
      END
    END
    RESULTS:
      File Compression Level = Default
      Option = Standard
    END
  END
  SOLVER CONTROL:
    Turbulence Numerics = High Resolution
    ADVECTION SCHEME:
      Option = High Resolution
    END
    CONVERGENCE CONTROL:
```

```
      Local Timescale Factor = 5
      Maximum Number of Iterations = 500
      Minimum Number of Iterations = 5
      Timescale Control = Local Timescale Factor
    END
    CONVERGENCE CRITERIA:
      Conservation Target = 0.005
      Residual Target = 0.00001
      Residual Type = MAX
    END
    DYNAMIC MODEL CONTROL:
      Global Dynamic Model Control = On
    END
  END
  EXPERT PARAMETERS:
    force intersection = t
    ggi stage groups max = 500
  END
END
COMMAND FILE:
  Version = 12.0.1
  Results Version = 12.0
END
SIMULATION CONTROL:
  EXECUTION CONTROL:
    EXECUTABLE SELECTION:
      Double Precision = Off
    END
    INTERPOLATOR STEP CONTROL:
      Runtime Priority = Standard
      EXECUTABLE SELECTION:
        Double Precision = Off
      END
      MEMORY CONTROL:
        Memory Allocation Factor = 1.0
      END
    END
    PARALLEL HOST LIBRARY:
      HOST DEFINITION: grzdlx054.graz.andritz.com
        Host Architecture String = linux-amd64
        Installation Root = /graz/apps/ansys_inc/v%v/CFX
      END
    END
    PARTITIONER STEP CONTROL:
      Multidomain Option = Coupled Partitioning
      Runtime Priority = Standard
      EXECUTABLE SELECTION:
        Use Large Problem Partitioner = Off
      END
      MEMORY CONTROL:
        Memory Allocation Factor = 1.8
      END
      PARTITIONING TYPE:
        MeTiS Type = k-way
        Option = MeTiS
        Partition Size Rule = Automatic
        Partition Weight Factors = 0.083, 0.083, 0.083, 0.083,
0.083, 0.083, \
          0.083, 0.083, 0.083, 0.083, 0.083, 0.083
      END
    END
    RUN DEFINITION:
      Solver Input File = /local1/1304434741/My.def
      Run Mode = Full
    END
    SOLVER STEP CONTROL:
```

```
      Runtime Priority = Low
      EXECUTABLE SELECTION:
        Double Precision = Off
      END
      MEMORY CONTROL:
        Memory Allocation Factor = 1.8
      END
      PARALLEL ENVIRONMENT:
        Number of Processes = 12
        Parallel Host List = grzdlx054.graz.andritz.com*12
        Start Method = MPICH Local Parallel
      END
    END
  END
END
```

```
 This run of the CFX-12.0 Solver started at 13:03:13 on 24 May 2011
by
 user trainee01 on grzdlx064.graz.andritz.com
 (intel_xeon64.sse2_linux2.5) using the command:

  /graz/apps/ansys_inc/v120/CFX/bin/cfx5solve -batch -definition
My.def -ccl
    /graz/pumpe/AmuZang/transient_cfx/macros/solve_AZ_transient.ccl

 Setting up CFX Solver run ...



+--------------------------------------------------------------------
+
 |
|
 |                    CFX Command Language for Run
|
 |
|

+--------------------------------------------------------------------
+

 LIBRARY:
   CEL:
     EXPRESSIONS:
       MPetagesIEC = (abs(massFlow()@RN_HP Side 1)/(997 [kg m^-3])) *
\
         (massFlowAve(Pressure)@RN_HP Side 1 + (massFlow()@RN_HP Side
\
         1/area()@RN_HP Side 1)^2/(2*997[kg m^-3]) - \
         massFlowAve(Pressure)@RN_LP Side 2 - (massFlow()@RN_LP Side
\
         2/area()@RN_LP Side 2)^2/(2*997 [kg m^-3]) ) / ( (torque_z()
@RN_BL + \
         torque_z()@RN_HUB + torque_z()@RN_SHR) * 141.7 [s^-1] )
       Hmech = (torque_z()@RN_BL + torque_z()@RN_HUB + torque_z()
@RN_SHR)* \
         141.7 [s^-1]/997 [kg m^-3]/9.81 [m s^-2]/Q DT
       Q DT = massFlow()@DT_LP/997 [kg m^-3]
       p tot IEC DT = massFlowAve(Pressure)@DT_LP + 997 [kg m^-3]* \
         ((massFlow()@DT_LP/997 [kg m^-3]/area()@DT_LP)^2)/2
       p tot IEC SC = massFlowAve(Pressure)@SC_HP + 997 [kg m^-3]* \
         ((massFlow()@SC_HP/997 [kg m^-3]/area()@SC_HP)^2)/2
       dH DT = (massFlowAve(Total Pressure in Stn Frame)@DT_HP - p
tot IEC \
         DT) /997 [kg m^-3] / 9.81 [m s^-2]
       dH RN = (massFlowAve(Total Pressure in Stn Frame)@RN_HP Side 1
- \
         massFlowAve(Total Pressure in Stn Frame)@RN_LP Side 2) /997
[kg \
         m^-3] / 9.81 [m s^-2]
       dH SC = (p tot IEC SC - massFlowAve(Total Pressure in Stn \
         Frame)@SC_LP) /997 [kg m^-3] / 9.81 [m s^-2]
       dH ges IEC = (p tot IEC SC - massFlowAve(Total Pressure in Stn
\
         Frame)@SC_LP + massFlowAve(Total Pressure in Stn Frame)
@RN_HP Side 1 \
         - massFlowAve(Total Pressure in Stn Frame)@RN_LP Side 2 + \
         massFlowAve(Total Pressure in Stn Frame)@DT_HP - p tot IEC
DT) /997 \
         [kg m^-3] / 9.81 [m s^-2]
       eta RN = dH RN/Hmech
       eta ges IEC = (dH RN+dH DT+dH SC) /Hmech
```

```
      eta DT = 1+dH DT/Hmech
      eta SC = 1+dH SC/Hmech
    END
  END
  MATERIAL: Water
    Material Description = Water (liquid)
    Material Group = Water Data, Constant Property Liquids
    Option = Pure Substance
    Thermodynamic State = Liquid
    PROPERTIES:
      Option = General Material
      EQUATION OF STATE:
        Density = 997.0 [kg m^-3]
        Molar Mass = 18.02 [kg kmol^-1]
        Option = Value
      END
      SPECIFIC HEAT CAPACITY:
        Option = Value
        Specific Heat Capacity = 4181.7 [J kg^-1 K^-1]
        Specific Heat Type = Constant Pressure
      END
      REFERENCE STATE:
        Option = Specified Point
        Reference Pressure = 1 [atm]
        Reference Specific Enthalpy = 0.0 [J/kg]
        Reference Specific Entropy = 0.0 [J/kg/K]
        Reference Temperature = 25 [C]
      END
      DYNAMIC VISCOSITY:
        Dynamic Viscosity = 8.899E-4 [kg m^-1 s^-1]
        Option = Value
      END
      THERMAL CONDUCTIVITY:
        Option = Value
        Thermal Conductivity = 0.6069 [W m^-1 K^-1]
      END
      ABSORPTION COEFFICIENT:
        Absorption Coefficient = 1.0 [m^-1]
        Option = Value
      END
      SCATTERING COEFFICIENT:
        Option = Value
        Scattering Coefficient = 0.0 [m^-1]
      END
      REFRACTIVE INDEX:
        Option = Value
        Refractive Index = 1.0 [m m^-1]
      END
      THERMAL EXPANSIVITY:
        Option = Value
        Thermal Expansivity = 2.57E-04 [K^-1]
      END
    END
  END
END
FLOW: Flow Analysis 1
  SOLUTION UNITS:
    Angle Units = [rad]
    Length Units = [m]
    Mass Units = [kg]
    Solid Angle Units = [sr]
    Temperature Units = [K]
    Time Units = [s]
  END
  ANALYSIS TYPE:
    Option = Transient
```

```
      EXTERNAL SOLVER COUPLING:
        Option = None
      END
      INITIAL TIME:
        Option = Automatic with Value
        Time = 0 [s]
      END
      TIME DURATION:
        Option = Total Time
        Total Time = 0.44341463 [s]
      END
      TIME STEPS:
        First Update Time = 0.042 [s]
        Initial Timestep = 2.46341461e-4 [s]
        Option = Adaptive
        Timestep Update Frequency = 1
        TIMESTEP ADAPTION:
          Maximum Timestep = 2.46341461e-4 [s]
          Minimum Timestep = 0.000023 [s]
          Option = Number of Coefficient Loops
          Target Maximum Coefficient Loops = 4
          Target Minimum Coefficient Loops = 2
          Timestep Decrease Factor = 0.95
          Timestep Increase Factor = 1.06
        END
      END
    END
    DOMAIN: DT
      Coord Frame = Coord 0
      Domain Type = Fluid
      Location = Primitive 3D 4,Primitive 3D 5,Primitive 3D
6,Primitive 3D \
        7,Primitive 3D 8,Primitive 3D 9
      BOUNDARY: DT hub
        Boundary Type = WALL
        Location = INFLOW_BLOCK2,INFLOW_BLOCK3
        BOUNDARY CONDITIONS:
          MASS AND MOMENTUM:
            Option = No Slip Wall
            WALL VELOCITY:
              Angular Velocity = -141.7 [radian s^-1]
              Option = Rotating Wall
              AXIS DEFINITION:
                Option = Coordinate Axis
                Rotation Axis = Coord 0.3
              END
            END
          END
          WALL ROUGHNESS:
            Option = Smooth Wall
          END
        END
      END
      BOUNDARY: DT_HP
        Boundary Type = INTERFACE
        Location = INFLOW_BLOCK1
        BOUNDARY CONDITIONS:
          MASS AND MOMENTUM:
            Option = Conservative Interface Flux
          END
          TURBULENCE:
            Option = Conservative Interface Flux
          END
        END
      END
      BOUNDARY: DT_LP
```

```
    Boundary Type = INLET
    Location = OUTFLOW_BLOCK1 2,OUTFLOW_BLOCK2 2,OUTFLOW_BLOCK3 2
    BOUNDARY CONDITIONS:
      FLOW REGIME:
        Option = Subsonic
      END
      MASS AND MOMENTUM:
        Option = Cartesian Velocity Components
        U = -0.98467 [m s^-1]
        V = 0 [m s^-1]
        W = 0 [m s^-1]
      END
      TURBULENCE:
        Omega = 0.04404 [s^-1]
        Option = k and Omega
        k = 0.00058176 [m^2 s^-2]
      END
    END
  END
  BOUNDARY: DT_WALL
    Boundary Type = WALL
    Location = SHROUD_BLOCK1,SHROUD_BLOCK1 2,SHROUD_BLOCK1
3,SHROUD_BLOCK1 \
      4,SHROUD_BLOCK1 5,SHROUD_BLOCK1 6
    BOUNDARY CONDITIONS:
      MASS AND MOMENTUM:
        Option = No Slip Wall
      END
      WALL ROUGHNESS:
        Option = Smooth Wall
      END
    END
  END
  DOMAIN MODELS:
    BUOYANCY MODEL:
      Option = Non Buoyant
    END
    DOMAIN MOTION:
      Option = Stationary
    END
    MESH DEFORMATION:
      Option = None
    END
    REFERENCE PRESSURE:
      Reference Pressure = 1 [atm]
    END
  END
  FLUID DEFINITION: Fluid 1
    Material = Water
    Option = Material Library
    MORPHOLOGY:
      Option = Continuous Fluid
    END
  END
  FLUID MODELS:
    COMBUSTION MODEL:
      Option = None
    END
    HEAT TRANSFER MODEL:
      Fluid Temperature = 25 [C]
      Option = Isothermal
    END
    THERMAL RADIATION MODEL:
      Option = None
    END
    TURBULENCE MODEL:
```

```
        Option = SST
      END
      TURBULENT WALL FUNCTIONS:
        Option = Automatic
      END
    END
    INITIALISATION:
      Option = Automatic
      INITIAL CONDITIONS:
        Velocity Type = Cylindrical
        CYLINDRICAL VELOCITY COMPONENTS:
          Option = Automatic with Value
          Velocity Axial Component = -3 [m s^-1]
          Velocity Theta Component = 0 [m s^-1]
          Velocity r Component = 1 [m s^-1]
          AXIS DEFINITION:
            Option = Coordinate Axis
            Rotation Axis = Coord 0.3
          END
        END
        STATIC PRESSURE:
          Option = Automatic with Value
          Relative Pressure = -20e4 [Pa]
        END
        TURBULENCE INITIAL CONDITIONS:
          Option = Medium Intensity and Eddy Viscosity Ratio
        END
      END
    END
  END
  DOMAIN: RN
    Coord Frame = Coord 0
    Domain Type = Fluid
    Location = Assembly 10
    BOUNDARY: RN_BL
      Boundary Type = WALL
      Frame Type = Rotating
      Location = BLADE,BLADE 2,BLADE 3,BLADE 4,BLADE 5,BLADE 6
      BOUNDARY CONDITIONS:
        MASS AND MOMENTUM:
          Option = No Slip Wall
        END
        WALL ROUGHNESS:
          Option = Smooth Wall
        END
      END
    END
    BOUNDARY: RN_HP Side 1
      Boundary Type = INTERFACE
      Location = WEST,WEST 2,WEST 3,WEST 4,WEST 5,WEST 6
      BOUNDARY CONDITIONS:
        MASS AND MOMENTUM:
          Option = Conservative Interface Flux
        END
        TURBULENCE:
          Option = Conservative Interface Flux
        END
      END
    END
    BOUNDARY: RN_HUB
      Boundary Type = WALL
      Frame Type = Rotating
      Location = HUB,HUB 2,HUB 3,HUB 4,HUB 5,HUB 6,HUB_EAST,HUB_EAST
\
        2,HUB_EAST 3,HUB_EAST 4,HUB_EAST 5,HUB_EAST 6
      BOUNDARY CONDITIONS:
```

```
        MASS AND MOMENTUM:
          Option = No Slip Wall
        END
        WALL ROUGHNESS:
          Option = Smooth Wall
        END
      END
    END
    BOUNDARY: RN_LP Side 2
      Boundary Type = INTERFACE
      Location = EAST,EAST 2,EAST 3,EAST 4,EAST 5,EAST 6
      BOUNDARY CONDITIONS:
        MASS AND MOMENTUM:
          Option = Conservative Interface Flux
        END
        TURBULENCE:
          Option = Conservative Interface Flux
        END
      END
    END
    BOUNDARY: RN_SHR
      Boundary Type = WALL
      Frame Type = Rotating
      Location = SHROUD,SHROUD 2,SHROUD 3,SHROUD 4,SHROUD 5,SHROUD \
        6,SHROUD_EAST,SHROUD_EAST 2,SHROUD_EAST 3,SHROUD_EAST
4,SHROUD_EAST \
        5,SHROUD_EAST 6
      BOUNDARY CONDITIONS:
        MASS AND MOMENTUM:
          Option = No Slip Wall
        END
        WALL ROUGHNESS:
          Option = Smooth Wall
        END
      END
    END
    DOMAIN MODELS:
      BUOYANCY MODEL:
        Option = Non Buoyant
      END
      DOMAIN MOTION:
        Alternate Rotation Model = On
        Angular Velocity = -141.7 [radian s^-1]
        Option = Rotating
        AXIS DEFINITION:
          Option = Coordinate Axis
          Rotation Axis = Coord 0.3
        END
      END
      MESH DEFORMATION:
        Option = None
      END
      REFERENCE PRESSURE:
        Reference Pressure = 1 [atm]
      END
    END
    FLUID DEFINITION: Fluid 1
      Material = Water
      Option = Material Library
      MORPHOLOGY:
        Option = Continuous Fluid
      END
    END
    FLUID MODELS:
      COMBUSTION MODEL:
        Option = None
```

```
        END
        HEAT TRANSFER MODEL:
          Fluid Temperature = 25 [C]
          Option = Isothermal
        END
        THERMAL RADIATION MODEL:
          Option = None
        END
        TURBULENCE MODEL:
          Option = SST
        END
        TURBULENT WALL FUNCTIONS:
          Option = Automatic
        END
      END
      INITIALISATION:
        Frame Type = Rotating
        Option = Automatic
        INITIAL CONDITIONS:
          Velocity Type = Cylindrical
          CYLINDRICAL VELOCITY COMPONENTS:
            Option = Automatic with Value
            Velocity Axial Component = -3 [m s^-1]
            Velocity Theta Component = 0 [m s^-1]
            Velocity r Component = 1 [m s^-1]
          END
          STATIC PRESSURE:
            Option = Automatic with Value
            Relative Pressure = -20e4 [Pa]
          END
          TURBULENCE INITIAL CONDITIONS:
            Option = Medium Intensity and Eddy Viscosity Ratio
          END
        END
      END
    END
    DOMAIN: SC
      Coord Frame = Coord 0
      Domain Type = Fluid
      Location = Primitive 3D
      BOUNDARY: SC_BL
        Boundary Type = WALL
        Location = Primitive 2D B,Primitive 2D C,Primitive 2D
D,Primitive 2D \
          E,Primitive 2D F,Primitive 2D G,Primitive 2D H,Primitive 2D
\
          I,Primitive 2D J,Primitive 2D K,Primitive 2D L,Primitive 2D
\
          M,Primitive 2D N,Primitive 2D O,Primitive 2D P,Primitive 2D
Q
        BOUNDARY CONDITIONS:
          MASS AND MOMENTUM:
            Option = No Slip Wall
          END
          WALL ROUGHNESS:
            Option = Smooth Wall
          END
        END
      END
      BOUNDARY: SC_GGI_DE Side 1
        Boundary Type = INTERFACE
        Location = SC_GGI_DE_A
        BOUNDARY CONDITIONS:
          MASS AND MOMENTUM:
            Option = Conservative Interface Flux
          END
```

```
    TURBULENCE:
      Option = Conservative Interface Flux
    END
  END
END
BOUNDARY: SC_GGI_DE Side 2
  Boundary Type = INTERFACE
  Location = SC_GGI_DE_B
  BOUNDARY CONDITIONS:
    MASS AND MOMENTUM:
      Option = Conservative Interface Flux
    END
    TURBULENCE:
      Option = Conservative Interface Flux
    END
  END
END
BOUNDARY: SC_GGI_SEP_B
  Boundary Type = INTERFACE
  Location = SC_GGI_SEP_B
  BOUNDARY CONDITIONS:
    MASS AND MOMENTUM:
      Option = Conservative Interface Flux
    END
    TURBULENCE:
      Option = Conservative Interface Flux
    END
  END
END
BOUNDARY: SC_LP
  Boundary Type = INTERFACE
  Location = SC_LP
  BOUNDARY CONDITIONS:
    MASS AND MOMENTUM:
      Option = Conservative Interface Flux
    END
    TURBULENCE:
      Option = Conservative Interface Flux
    END
  END
END
BOUNDARY: SC_WALL
  Boundary Type = WALL
  Location = Primitive 2D
  BOUNDARY CONDITIONS:
    MASS AND MOMENTUM:
      Option = No Slip Wall
    END
    WALL ROUGHNESS:
      Option = Smooth Wall
    END
  END
END
DOMAIN MODELS:
  BUOYANCY MODEL:
    Option = Non Buoyant
  END
  DOMAIN MOTION:
    Option = Stationary
  END
  MESH DEFORMATION:
    Option = None
  END
  REFERENCE PRESSURE:
    Reference Pressure = 1 [atm]
  END
```

```
  END
  FLUID DEFINITION: Fluid 1
    Material = Water
    Option = Material Library
    MORPHOLOGY:
      Option = Continuous Fluid
    END
  END
  FLUID MODELS:
    COMBUSTION MODEL:
      Option = None
    END
    HEAT TRANSFER MODEL:
      Fluid Temperature = 25 [C]
      Option = Isothermal
    END
    THERMAL RADIATION MODEL:
      Option = None
    END
    TURBULENCE MODEL:
      Option = SST
    END
    TURBULENT WALL FUNCTIONS:
      Option = Automatic
    END
  END
  INITIALISATION:
    Option = Automatic
    INITIAL CONDITIONS:
      Velocity Type = Cylindrical
      CYLINDRICAL VELOCITY COMPONENTS:
        Option = Automatic with Value
        Velocity Axial Component = 0 [m s^-1]
        Velocity Theta Component = -1 [m s^-1]
        Velocity r Component = 1 [m s^-1]
        AXIS DEFINITION:
          Option = Coordinate Axis
          Rotation Axis = Coord 0.3
        END
      END
      STATIC PRESSURE:
        Option = Automatic with Value
        Relative Pressure = 0 [Pa]
      END
      TURBULENCE INITIAL CONDITIONS:
        Option = Medium Intensity and Eddy Viscosity Ratio
      END
    END
  END
END
DOMAIN: SC SEP
  Coord Frame = Coord 0
  Domain Type = Fluid
  Location = Assembly 9
  BOUNDARY: SC_GGI_SEP_A
    Boundary Type = INTERFACE
    Location = SC_GGI_SEP_A
    BOUNDARY CONDITIONS:
      MASS AND MOMENTUM:
        Option = Conservative Interface Flux
      END
      TURBULENCE:
        Option = Conservative Interface Flux
      END
    END
  END
```

```
BOUNDARY: SC_HP
  Boundary Type = OUTLET
  Location = SC_HP
  BOUNDARY CONDITIONS:
    FLOW REGIME:
      Option = Subsonic
    END
    MASS AND MOMENTUM:
      Option = Static Pressure
      Relative Pressure = 0 [Pa]
    END
  END
END
BOUNDARY: SC_SEP_WALL
  Boundary Type = WALL
  Location = Primitive 2D A
  BOUNDARY CONDITIONS:
    MASS AND MOMENTUM:
      Option = No Slip Wall
    END
    WALL ROUGHNESS:
      Option = Smooth Wall
    END
  END
END
DOMAIN MODELS:
  BUOYANCY MODEL:
    Option = Non Buoyant
  END
  DOMAIN MOTION:
    Option = Stationary
  END
  MESH DEFORMATION:
    Option = None
  END
  REFERENCE PRESSURE:
    Reference Pressure = 1 [atm]
  END
END
FLUID DEFINITION: Fluid 1
  Material = Water
  Option = Material Library
  MORPHOLOGY:
    Option = Continuous Fluid
  END
END
FLUID MODELS:
  COMBUSTION MODEL:
    Option = None
  END
  HEAT TRANSFER MODEL:
    Fluid Temperature = 25 [C]
    Option = Isothermal
  END
  THERMAL RADIATION MODEL:
    Option = None
  END
  TURBULENCE MODEL:
    Option = SST
  END
  TURBULENT WALL FUNCTIONS:
    Option = Automatic
  END
END
INITIALISATION:
  Option = Automatic
```

```
    INITIAL CONDITIONS:
      Velocity Type = Cartesian
      CARTESIAN VELOCITY COMPONENTS:
        Option = Automatic with Value
        U = 0 [m s^-1]
        V = 1 [m s^-1]
        W = 0 [m s^-1]
      END
      STATIC PRESSURE:
        Option = Automatic
      END
      TURBULENCE INITIAL CONDITIONS:
        Option = Medium Intensity and Eddy Viscosity Ratio
      END
    END
  END
END
DOMAIN INTERFACE: RN_HP
  Boundary List1 = RN_HP Side 1
  Boundary List2 = SC_LP
  Interface Type = Fluid Fluid
  INTERFACE MODELS:
    Option = General Connection
    FRAME CHANGE:
      Option = Transient Rotor Stator
    END
    MASS AND MOMENTUM:
      Option = Conservative Interface Flux
      MOMENTUM INTERFACE MODEL:
        Option = None
      END
    END
    PITCH CHANGE:
      Option = Specified Pitch Angles
      Pitch Angle Side1 = 360 [degree]
      Pitch Angle Side2 = 360 [degree]
    END
  END
  MESH CONNECTION:
    Option = GGI
    INTERSECTION CONTROL:
      Option = Direct
    END
  END
END
DOMAIN INTERFACE: RN_LP
  Boundary List1 = DT_HP
  Boundary List2 = RN_LP Side 2
  Interface Type = Fluid Fluid
  INTERFACE MODELS:
    Option = General Connection
    FRAME CHANGE:
      Option = Transient Rotor Stator
    END
    MASS AND MOMENTUM:
      Option = Conservative Interface Flux
      MOMENTUM INTERFACE MODEL:
        Option = None
      END
    END
    PITCH CHANGE:
      Option = Specified Pitch Angles
      Pitch Angle Side1 = 360 [degree]
      Pitch Angle Side2 = 360 [degree]
    END
  END
```

```
  MESH CONNECTION:
    Option = GGI
    INTERSECTION CONTROL:
      Option = Direct
    END
  END
END
DOMAIN INTERFACE: SC_GGI_DE
  Boundary List1 = SC_GGI_DE Side 1
  Boundary List2 = SC_GGI_DE Side 2
  Interface Type = Fluid Fluid
  INTERFACE MODELS:
    Option = General Connection
    FRAME CHANGE:
      Option = None
    END
    MASS AND MOMENTUM:
      Option = Conservative Interface Flux
      MOMENTUM INTERFACE MODEL:
        Option = None
      END
    END
    PITCH CHANGE:
      Option = None
    END
  END
  MESH CONNECTION:
    Option = GGI
    INTERSECTION CONTROL:
      Option = Direct
    END
  END
END
DOMAIN INTERFACE: SC_GGI_SEP
  Boundary List1 = SC_GGI_SEP_B
  Boundary List2 = SC_GGI_SEP_A
  Interface Type = Fluid Fluid
  INTERFACE MODELS:
    Option = General Connection
    FRAME CHANGE:
      Option = None
    END
    MASS AND MOMENTUM:
      Option = Conservative Interface Flux
      MOMENTUM INTERFACE MODEL:
        Option = None
      END
    END
    PITCH CHANGE:
      Option = None
    END
  END
  MESH CONNECTION:
    Option = GGI
    INTERSECTION CONTROL:
      Option = Direct
    END
  END
END
OUTPUT CONTROL:
  MONITOR OBJECTS:
    MONITOR BALANCES:
      Option = Full
    END
    MONITOR FORCES:
      Option = Full
```

```
    END
    MONITOR PARTICLES:
      Option = Full
    END
    MONITOR POINT: Hmech
      Expression Value = Hmech
      Option = Expression
    END
    MONITOR POINT: dH DT
      Expression Value = dH DT
      Option = Expression
    END
    MONITOR POINT: dH RN
      Expression Value = dH RN
      Option = Expression
    END
    MONITOR POINT: dH SC
      Expression Value = dH SC
      Option = Expression
    END
    MONITOR POINT: dH ges IEC
      Expression Value = dH ges IEC
      Option = Expression
    END
    MONITOR POINT: eta DT
      Expression Value = eta RN
      Option = Expression
    END
    MONITOR POINT: eta RN
      Expression Value = eta RN
      Option = Expression
    END
    MONITOR POINT: eta SC
      Expression Value = eta RN
      Option = Expression
    END
    MONITOR POINT: eta ges IEC
      Expression Value = eta ges IEC
      Option = Expression
    END
    MONITOR RESIDUALS:
      Option = Full
    END
    MONITOR TOTALS:
      Option = Full
    END
  END
  RESULTS:
    File Compression Level = Default
    Option = Standard
  END
  TRANSIENT RESULTS: Transient Results 1
    File Compression Level = Default
    Option = Standard
    OUTPUT FREQUENCY:
      Option = Every Timestep
    END
  END
END
SOLVER CONTROL:
  Turbulence Numerics = First Order
  ADVECTION SCHEME:
    Option = High Resolution
  END
  CONVERGENCE CONTROL:
    Maximum Number of Coefficient Loops = 50
```

```
      Minimum Number of Coefficient Loops = 1
      Timescale Control = Coefficient Loops
    END
    CONVERGENCE CRITERIA:
      Residual Target = 0.00001
      Residual Type = RMS
    END
    TRANSIENT SCHEME:
      Option = Second Order Backward Euler
      TIMESTEP INITIALISATION:
        Option = Automatic
      END
    END
  END
  EXPERT PARAMETERS:
    force intersection = t
    transient initialisation override = t
  END
END
COMMAND FILE:
  Version = 12.0.1
  Results Version = 12.0
END
SIMULATION CONTROL:
  EXECUTION CONTROL:
    EXECUTABLE SELECTION:
      Double Precision = No
    END
    INTERPOLATOR STEP CONTROL:
      Runtime Priority = Standard
      EXECUTABLE SELECTION:
        Double Precision = Off
      END
      MEMORY CONTROL:
        Memory Allocation Factor = 1.5
      END
    END
    PARALLEL HOST LIBRARY:
      HOST DEFINITION: grzdlx064.graz.andritz.com
        Host Architecture String = linux-amd64
        Installation Root = /graz/apps/ansys_inc/v%v/CFX
      END
    END
    PARTITIONER STEP CONTROL:
      Multidomain Option = Coupled Partitioning
      Runtime Priority = Standard
      EXECUTABLE SELECTION:
        Use Large Problem Partitioner = Off
      END
      MEMORY CONTROL:
        Memory Allocation Factor = 2.0
      END
      PARTITIONING TYPE:
        MeTiS Type = k-way
        Multipass Partitioning Option = None
        Option = MeTiS
        Partition Size Rule = Automatic
        Partition Weight Factors = 0.200, 0.200, 0.200, 0.200, 0.200
      END
    END
    RUN DEFINITION:
      Solver Input File = /local/cfx_solve_0_98467/My.def
      Run Mode = Full
    END
    SOLVER STEP CONTROL:
      Runtime Priority = Low
```

```
      EXECUTABLE SELECTION:
        Double Precision = Off
      END
      MEMORY CONTROL:
        Memory Allocation Factor = 1.8
      END
      PARALLEL ENVIRONMENT:
        Number of Processes = 5
        Parallel Host List = grzdlx064.graz.andritz.com*5
        Start Method = MPICH Local Parallel
      END
    END
  END
END
```

Bibliography

[1] O. BRAUN. *Part Load Flow in Radial Centrifugal Pumps.* PhD Thesis, École Polytechnique Fédérale de Lausanne, Thèse No 4422, 2009.

[2] G. BRENN. Vorlesungsskriptum: Strömungslehre und wärmeÃ¼bertragung i. *Institut für Strömungslehre, TU Graz*, 2007.

[3] A. COLAGROSSI, M. LANDRINI. Numerical simulation of interfacial flows by Smoothed Particle Hydrodynamics. *J. Comp. Phys., 191 :448-475*, 2003.

[4] J.H. FERZIGER, M. PERIĆ. *Computational Methods for Fluid Dynamics.* 3rd rev. ed., Springer Verlag Berlin Heidelberg NewYork, ISBN 3-540-42074-6, 2002.

[5] A. GEHRER. *Entwicklung eines 3D-Navier-Stokes Codes zur numerischen Berechnung der Turbomaschinenströmung.* PhD Thesis, Technischen Universität Graz, 1998.

[6] J.F. GÜLICH. Centrifugal Pumps. *Springer-Verlag Berlin Heidelberg*, 2008.

[7] J.F. GÜLICH, R. EGGER. *Part load flow and hydraulic stability of centrifugal pumps.* EPRI Report TR-100219, 1992.

[8] M. GUGAU. *Ein Beitrag zur Validierung der numerischen Berechnung von Kreiselpumpen.* PhD Thesis, Technische UniversitÃ¤t Darmstadt, 2004.

[9] IEC 60193 *International Standard - Hydraulic turbines, storage pumps and pump turbines - Model acceptance tests.* International Electrotechnical Commission, 1999.

[10] H. JABERG *Hydraulische Strömungsmaschinen (317.024).* Vorlesungsskriptum, TU Graz, 2011.

[11] J. LEDUC. *Étude physique et numérique de l'écoulement dans un système d'injection de turbine Pelton.* PhD thesis, Ecole Centrale de Lyon, 2010.

[12] E.S. LEE. Testcase 3: Lid-driven cavity flow. *1st international SPHERIC workshop, Roma, Italy*, 2006.

[13] LIU G.R.; LIU M.B. *Smoothed Particle Hydrodynamics - A Meshfree Particle Method.* World Scientific Publishing Co. Pte. Ltd., 2003.

[14] J.C. MARONGIU. *Methode numerique lagrangienne pour la simulation d'ecoulements a surface libre Application aux turbines Pelton.* PhD thesis, Ecole Centrale de Lyon, 2007.

[15] J.C. MARONGIU, F. LEBOEUF, E. PARKINSON. *Riemann solvers and efficient boundary treatments: an hybrid SPH-finite volume numerical method.* 3rd ERCOFTAC SPHERIC workshop on SPH applications, Lausanne, Switzerland, 2008.

[16] W.L. OBERKAMPF, T.G. TRUCANO. *Verification and Validation in Computational Fluid Dynamics.* Report, SAND2002-0529, Sandia National Laboratories, 2002.

[17] G. OGER. Aspects théoriques de la méthode SPH et applications à l'hydrodynamique à surface libre. *École Centrale de Nantes*, 2006.

[18] P. PIERINGER. Incompressible 3D Euler Flow-Solver: First step of documentation. *ÁSTROE, Project Eulerkette*, July 2007.

[19] J.F. PRICE. Lagrangian and eulerian representations of fluid flow: Kinematics and the equations of motion. *Woods Hole Oceanographic Institution Woods Hole (MA)*, 2006.

[20] P.W. RANDLES, L.D. LIBERSKY Smoothed particle hydrodynamics : some recent improvements and applications. *Computational Methods Applied Mechanical Engineering, 139:375-408*, 1996.

[21] P.J. ROACHE *Verification and Validation in Computational Science and Engineering.* hermosa publishers, Albuquerque, 1998.

[22] M. SALLABERGER et.al. *Experimental and Numerical Studies of Flow Instabilities in Pump-Turbine Stages.* International Association for Hydro-Environment Engineering and Research, Sulzer Hydro, Zürich, 1998.

[23] W. SANZ. *Computational Fluid Dynamics (319.082).* Vorlesungsskriptum, TU Graz, 2011.

[24] M.S. SHADLOO et al. *Improved Incompressible Smoothed Hydrodynamics method for simulating flow around bluff bodies.* Computational Methods in Applied Mechanics and Engineering, 200, p. 1008-1020, Elsevier B.V., 2010.

[25] E.F. TORO. *Riemann Solvers and Numerical Methods for Fluid Dynamics: A practical Introduction.* Third Edition, Springer Verlag, 2009.

[26] G. TREUTZ. *Numerische Simulation der instationären Strömung in einer Kreiselpumpe.* PhD Thesis, Technischen Universität Darmstadt, 2002.

[27] H.K. VERSTEEG, W. MALALASEKERA. *An Introduction to Computational Fluid Dynamics The Finite Volume Method.* 2nd Edition, Pearson Education Limited, 2007.

[28] J.P. VILA. On particle weighted methods and Smoothed Particle Hydrodynamics. *Mathematical models and Methods in Applied Sciences, 9 :161-209*, 1999.

[29] J.P. VILA. Méthodes particulaires régularisées. Dévelopements récents et nouvelles applications. *ESAIM Proceedings, Actes du 29ème congrè d'analyse numérique: CA NUM'97, volume 3, pages 131-146*, 1998.

[30] ANSYS CFX Manual *Release 12.0.* 2011.

[31] ANSYS FLUENT *Determining Turbulence Parameters.* URL: https://www.sharcnet.ca/Software/Fluent6/html/ug/node217.htm, access 23.01.2012.